

# SPRAY FORMING OF Al-Si-Pb ALLOYS AND THEIR CHARACTERIZATION

## A THESIS

*Submitted in partial fulfilment of the requirements for the award of the degree of*

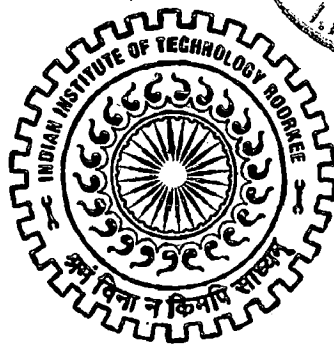
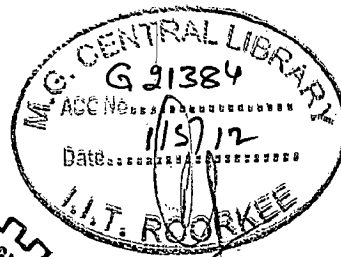
DOCTOR OF PHILOSOPHY

*in*

METALLURGICAL AND MATERIALS ENGINEERING

*by*

**ARUNA TOMAR**



DEPARTMENT OF METALLURGICAL AND MATERIALS ENGINEERING  
INDIAN INSTITUTE OF TECHNOLOGY ROORKEE  
ROORKEE-247 667 (INDIA)

FEBRUARY, 2010

**©INDIAN INSTITUTE OF TECHNOLOGY ROORKEE, ROORKEE, 2010  
ALL RIGHTS RESERVED**



# INDIAN INSTITUTE OF TECHNOLOGY ROORKEE ROORKEE

## CANDIDATE'S DECLARATION

I hereby certify that the work which is being presented in the thesis entitled "**Spray forming of Al-Si-Pb alloys and their characterization**" in partial fulfilment of the requirement for the award of the Degree of Doctor of Philosophy and submitted in the Department of Metallurgical & Materials Engineering of the Indian Institute of Technology Roorkee, Roorkee is an authentic record of my own work carried out during a period from Jan. 2006 to Feb 2010 under the supervision of **Dr. Devendra Singh**, Assistant Professor, Department of Metallurgical and Materials Engineering, Indian Institute of Technology Roorkee, Roorkee.

The matter presented in this thesis has not been submitted by me for the award of any other degree of this or any other Institute.

*Aruna Tomar*  
(ARUNA TOMAR)

This is to certify that the above statement made by the candidate is correct to the best of my knowledge.

*D. Singh*  
(Devendra Singh)  
Supervisor

Date: 23/2/10

The Ph.D. Viva-Voce Examination of '**Aruna Tomar**', Research Scholar, has been held on.....

Signature of Supervisor

Signature of External Examiner

## ABSTRACT

Processing of Al–Pb–Si alloys by the conventional casting techniques is difficult due to liquid immiscibility and segregation of lead during melt solidification. To overcome these problems, spray forming can be used which also possesses several advantages like microstructural control together with producing a near net shape preform in a less number of processing steps. In present study a convergent-divergent nozzle to atomize the melt was designed and fabricated. Before spray forming, a detailed gas field study of this nozzle was carried out using a pitot tube. Then, Al–Si–Pb alloys were spray formed in the form of a disc shape by using this nozzle and then their characteristics such as thickness uniformity of the disc, microstructure, porosity, hardness, strength, wear etc. were studied.

The spray droplets were deposited over a rotating copper substrate to achieve a disc shape preform. The thickness uniformity of the preform was found to depend on the preform distance from the nozzle, preform offset distance from the axis of the atomizer and inclination of the preform from the horizontal plane. Mathematical equations were developed to represent the thickness variation of the preform with aforementioned parameters.

The porosity, hardness, strength, wear and microstructural studies of the Al–Si–Pb spray deposited alloys were conducted for different lead content, top to bottom distance of the deposit and the distance from centre to periphery of the deposit. Overspray and worn debris particles were also analyzed. Particles/droplets of two different types were observed to deposit on the substrate. First type particles were aluminum rich and second type were lead rich. Optical micrographs were taken at four different locations of the deposit viz. (a) top (b) middle (c) bottom and (d) peripheral regions. The size of the aluminum grains was almost same at the bottom and top regions of the deposit whereas it was lower at the peripheral region. In middle region the grain size was a little bit coarser than at the top or bottom region. In scanning electron micrograph the grain boundaries were not clear with the increase in lead content and maximum amount of lead was distributed along the grain boundaries. The lead was uniformly dispersed in the deposit as revealed by color dot map.

The porosity was found to decrease with the decrease in lead content and the

distance from centre to periphery of the deposit. It remains constant with thickness of the deposit. The areas having large and small amount of porosity were observed in the microstructure of Al-Si-Pb alloys. The large and small amount porosity areas belong to the lead and aluminum rich areas, respectively.

The hardness of the deposit was observed to decrease with the increase in lead content and its effect on hardness increased with the increase in lead content. Its value was high for high silicon content. Preform hardness increased from centre to periphery of the deposit whereas it remained constant with the increase in distance from bottom to top of the deposit. Hardness was not affected by the grain size although it decreased with the increase in porosity of the deposit.

Ultimate tensile strength, proof stress and elongation to fracture were found to decrease linearly with the increase in lead content of the deposit. Both the strengths and elongation increased linearly with the increase in distance from centre to periphery of the deposit. Both the strengths were also higher for higher silicon content. Ultimate tensile strength, proof stress and elongation to fracture decreased exponentially with the increase in porosity of the deposit. Both, Ultimate tensile strength and proof stress were found to have a linear relationship with the hardness of the deposit.

Friction and wear testing of spray formed alloys were investigated using a pin on disc type wear testing machine. Wear rate behavior with applied load was observed to depict three stages, in the second stage rate of increase in wear rate was the lowest and in the third stage it was the highest. The wear rate decreased with the increase in distance from centre to periphery of the deposit. It decreased linearly with the increase in lead content and it was lower for 12 % Si as compared to that of 6 % Si in Al-Si-Pb alloys. The coefficient of friction decreased rapidly up to the load of 40 N and beyond this load the friction coefficient was almost constant. The coefficient of friction was lower for higher lead content.

## **ACKNOWLEDGEMENTS**

I would like to extend my sincere gratitude to Dr. Devendra Singh, Asst. Prof. for suggesting an interesting study, for his able guidance, for the informative discussions and for his assistance which made this work possible and successful.

I would also like to thank all faculty and staff members for their kind cooperation given to me for my work.

I would like to express my gratitude for my parents, brother and sisters for their encouragement, continuous and unconditional support throughout of my work. Also, I could not forget Rishu and Taru whose sweet talk takes all the tension away.

My gratitude also goes to my friends Manali and priti who were always with me to support and encouragement.

I also would like to extend my special thanks to Sir and Binita mam for their kind support and encouragement throughout of my work.

I would also like to thank all those who directly and indirectly attached to me for their kind support given to me during my Ph.D.

Above all I want to dedicate my thesis to God without whom this Ph.D. thesis could not be completed.

**(ARUNA TOMAR)**

# CONTENTS

Certificate	I
Abstract	III
Acknowledgement	V
List of figures	XI
List of tables	XVI
List of symbols	XVII
<b>1. INTRODUCTION</b>	<b>1</b>
<b>2. LITERATURE REVIEW</b>	<b>5</b>
<b>2.1 Atomizer Design</b>	<b>5</b>
<b>2.2 Gas Field of Atomizer</b>	<b>5</b>
<b>2.3 Droplets Solidification</b>	<b>7</b>
<b>2.4 Preform Shape</b>	<b>8</b>
<b>2.5 Al-Si-Pb Preform Characteristics</b>	<b>8</b>
<b>3. PROBLEM FORMULATION</b>	<b>15</b>
<b>4. EXPERIMENTAL SET-UP and PROCEDURE</b>	<b>17</b>
<b>4.1 Atomizer Characterization</b>	<b>17</b>
4.1.1 Atomizer design	17
4.1.2 Gas velocities from the atomizer	19
4.1.3 Gas flow rate through atomizer	20
<b>4.2 Spray Deposition of Al-Si-Pb alloys</b>	<b>21</b>
<b>4.3 Spray Deposit Characterization</b>	<b>24</b>
4.3.1 Shape	24
4.3.2 Porosity	24
4.3.3 Microstructure	25
4.3.4 EDAX analysis	26
4.3.5 XRD analysis	26
4.3.6 Hardness	26
4.3.7 Tensile testing	27
4.3.8 Wear testing	28

<b>5. RESULTS</b>	29
<b>5.1 Gas Dynamics of Atomizer</b>	29
5.1.1 Gas velocities	29
(a) Axial velocity	29
(b) Radial velocity	32
5.1.2 Gas flow rate	36
<b>5.2 Shape of Spray Deposit</b>	37
<b>5.3 Porosity in Spray Deposit</b>	39
<b>5.4 Microstructural Features</b>	45
5.4.1 Spray particle	45
5.4.2 Spray deposit	50
<b>5.5 Mechanical Properties</b>	60
5.5.1 Hardness	60
5.5.2 Strength and Elongation	63
<b>5.6 Tribological Properties</b>	68
5.6.1 Wear Rate	68
5.6.2 Coefficient of friction	71
5.6.3 Worn-out surface analysis	73
5.6.4 Worn-out debris analysis	74
<b>6. DISCUSSION</b>	75
<b>6.1 Atomizer Characteristics</b>	75
6.1.1 Gas Velocity Field Formation	75
6.1.2 Discharge Coefficient	78
<b>6.2 Thickness Uniformity of the Deposit</b>	81
6.2.1 Effect of inclination angle	81
6.2.2 Effect of offset distance	85
6.2.3 Effect of substrate distance	87
<b>6.3 Solidification &amp; Microstructure Evolution</b>	89
6.3.1 In powder particles	89
6.3.2 In spray deposit	91



<b>6.4</b>	<b>Porosity Formation</b>	93
<b>6.5</b>	<b>Hardness Characteristics</b>	97
<b>6.6</b>	<b>Preform Strength and Elongation</b>	98
<b>6.7</b>	<b>Wear Characteristics</b>	102
6.7.1	Wear rate	102
6.7.2	Coefficient of friction	105
<b>7.</b>	<b>CONCLUSIONS</b>	107
<b>8.</b>	<b>SCOPE FOR FUTURE WORK</b>	111
<b>REFERENCES</b>		113
<b>APPENDIX-A</b>	<b>Derivation for <math>r_1</math> and <math>r_2</math> of figure 6.4</b>	121
<b>APPENDIX-B</b>	<b>Some publications from this work</b>	123

## List of figures

2.1	A conventional confined type atomizer.	6
4.1	Design of the atomizer.	18
4.2	Photograph of atomizer used in gas dynamics study and spray forming.	19
4.3	Schematic of the gas dynamics.	20
4.4	Schematic of spray forming.	22
4.5	Locations of samples cut from spray deposit for porosity measurements.	25
4.6	Sample locations for microstructural study of the preform.	25
4.7	Cutting of sample in strip form from preform for hardness study.	26
4.8	(a) front and (b) side view of sample cut from the preform for hardness study.	27
4.9	Dimensions of the specimens used for tensile testing.	27
5.1	Variation of gas velocity with axial distance for zero radial distance at different plenum pressures.	30
5.2	Gas velocity variation with axial distance for radial distance of 10 mm at different plenum pressures.	30
5.3	Gas velocity variation with axial distance for 20 mm radial distance at different plenum pressures.	31
5.4	Gas velocity variation with axial distance for 30 mm radial distance at different plenum pressures.	32
5.5	Variation in gas velocity with radial distance for 25 mm axial distance at different plenum pressures.	33
5.6	Variation in gas velocity with radial distance for 50 mm axial distance at different plenum pressures.	33
5.7	Variation in gas velocity with radial distance for 100 mm axial distance at different plenum pressures.	34

<b>5.8</b>	Variation in gas velocity with radial distance for 300 mm axial distance at different plenum pressures.	35
<b>5.9</b>	Experimental and calculated gas mass flow rate as a function of plenum pressure.	36
<b>5.10</b>	Shape of spray deposit produced at different substrate distances (h), offset distances (s) and inclination angles ( $\theta$ ): (a) $h=400, \theta=0, s=0$ ; (b) $h=450, \theta=0, s=0$ ; (c) $h=500, \theta=0, s=0$ ; (d) $h=450, \theta=0, s=40$ ; (e) $h=450, \theta=15, s=40$ and (f) $h=450\text{ mm}, \theta=30\text{ deg}, s=40\text{ mm}$ .	38
<b>5.11</b>	Measured densities (gm/cc) with their locations in the spray deposit for different percentage of Pb: (a) 0; (b) 10; (c) 15; (d) 20 and (e) 25%.	41
<b>5.12</b>	Variation in porosity with distance from centre to periphery of spray deposited preform at different Pb content.	42
<b>5.13</b>	Porosity variation with Pb content at different distances from centre of deposit.	42
<b>5.14</b>	Microstructure at 4000x to show porosity variation from centre to periphery of the deposit at distances: (a) 0; (b) 20; (c) 40 and (d) 70 mm.	43
<b>5.15</b>	Micrograph showing the porosity distribution with Pb content of (a) 10; (b) 15; (c) 20 and (d) 25% at center of the deposit.	44
<b>5.16</b>	EDAX spectrum with analyzed (a) whole region; (b) bright region, indicating Pb and Si phases in spray deposited Al-6Si-20Pb alloy.	46
<b>5.17</b>	SEM micrographs showing the size, shape and some other characteristics of Al-6Si-10Pb alloy spray particles at magnification of (a)200x and (b) 500x.	47
<b>5.18</b>	SEM micrograph showing the size, shape and some other characteristics of Al- 6Si-20Pb alloy spray particles at magnification of (a)200x and (b) 500x.	48
<b>5.19</b>	SEM micrograph showing the surface topography of Pb rich particle.	49
<b>5.20</b>	Microstructure of the cross-section of two different particles (a) and (b).	49
<b>5.21</b>	Microstructure of spray deposited Al-6Si alloy showing (a) top; (b) middle; (c) bottom and (d) peripheral regions.	51

<b>5.22</b>	Micrograph of spray deposited Al-6Si-10Pb alloy showing distribution of Pb and Si particles at (a) top; (b) middle; (c) bottom and (d) peripheral regions.	<b>52</b>
<b>5.23</b>	Micrograph of spray deposited Al-6Si-15Pb alloy showing distribution of Pb and Si particles at (a) top; (b) middle; (c) bottom and (d) peripheral regions.	<b>53</b>
<b>5.24</b>	Micrograph of spray deposited Al-6Si-20Pb alloy showing distribution of Pb and Si particles at (a) top; (b) middle; (c) bottom and (d) peripheral regions.	<b>54</b>
<b>5.25</b>	Micrograph of spray deposited Al-6Si-25Pb alloy showing distribution of Pb and Si particles at (a) top; (b) middle; (c) bottom and (d) peripheral regions.	<b>55</b>
<b>5.26</b>	SEM micrographs showing the Pb (white phase) distribution in Al-6Si matrix for (a) 10; (b) 15; (c) 20 and (d) 25 % Pb.	<b>57</b>
<b>5.27</b>	Color dot maps of all three elements: (a) Al; (b) Si and (c) Pb in the Al-6Si-15Pb spray deposit alloy.	<b>58</b>
<b>5.28</b>	XRD patterns at centre of spray deposit for different composition of Pb: (a) 10; (b) 15; (c) 20 and (d) 25% in Al-6Si alloy.	<b>59</b>
<b>5.29</b>	Variation in hardness with Pb content at different distances from centre to periphery of the deposit.	<b>60</b>
<b>5.30</b>	Variation in hardness with distance from centre to periphery at different Pb contents.	<b>61</b>
<b>5.31</b>	Variation in hardness with distance from bottom to top at centre of the deposit.	<b>62</b>
<b>5.32</b>	Variation in hardness with distance from bottom to top for 15% Pb in Al-Si-Pb alloy at centre of the deposit.	<b>63</b>
<b>5.33</b>	Stress- Strain plots for (a) Al-6Si, (b) Al-6Si-10Pb, (c) Al-6Si-15Pb, (d) Al-6Si-20Pb and (e) Al-6Si-25Pb.	<b>64</b>
<b>5.34</b>	Variation in stress of spray formed Al-6Si-Pb alloys with Pb content.	<b>65</b>
<b>5.35</b>	Variation in elongation of spray formed Al-Si-Pb alloys with Pb content.	<b>66</b>

5.36	Variation in stress of Al-Si-15Pb alloys with distance from centre to periphery of the deposit for 6 and 12% Si.	66
5.37	Variation in elongation of spray formed Al-Si-15Pb alloys with distance from centre to periphery of the deposit at 6 and 12% Si.	67
5.38	Variation in wear rate of Al-6Si-Pb alloys as a function of applied load for different Pb contents.	68
5.39	Variation of wear rate with Pb content in spray deposited Al-6Si-Pb alloy at different applied load.	69
5.40	Variation in wear rate of spray formed Al-6Si-15Pb alloy with distance from centre to periphery at different loads.	70
5.41	Variation in wear rate of spray formed Al-Si-15Pb alloy as a function of applied load for 6 and 12% Si.	71
5.42	Variation in coefficient of friction with applied load at different % of Pb in Al-6Si-Pb alloy.	72
5.43	Variation in coefficient of friction with Pb content in spray deposit at different applied load.	72
5.44	Scanning electron micrographs of worn out surfaces of wear test specimen at different applied loads: (a) 10 N; (b) 40 N;(c) 60 N and (d) 80 N for 15% Pb alloy.	73
5.45	XRD patterns for the wear debris of Al-6Si-15Pb alloy at the loads of (a) 30N and (b) 70N.	74
6.1	Schematic of gas flow from nozzle and aspiration at the exit of melt delivery tube.	77
6.2	Comparison of calculated and experimental gas velocities.	78
6.3	Variation of gas discharge coefficient with plenum pressure.	80
6.4	Schematic to show the radius/area on which particle/mass distribution of spray cone takes place after tilting substrate an angle 'θ'.	83
6.5	Ratio of mass flux at 30 deg inclination angle ( $m_{30}$ ) to mass flux rate at 0 deg angle ( $m_0$ ) with ratio of radius $r/r_{0.5}$ of the substrate.	84

<b>6.6</b>	<b>Schematic to represent the mass distribution about substrate axis with an offset distance 's' from spray cone axis.</b>	<b>86</b>
<b>6.7</b>	<b>Variation of mass distribution in spray cone on substrate with an offset distance of 40 mm.</b>	<b>87</b>
<b>6.8</b>	<b>Variation of spray cone mass with spray cone radius for different values of deposition distance.</b>	<b>88</b>
<b>6.9</b>	<b>Average lead particle size as a function of lead content in Al-Si-Pb alloy.</b>	<b>96</b>
<b>6.10</b>	<b>Variation in strength with porosity at the centre of spray deposit.</b>	<b>100</b>
<b>6.11</b>	<b>Variation in elongation to fracture with porosity at centre of the spray deposit.</b>	<b>100</b>
<b>6.12</b>	<b>Variation in strengths with hardness at centre of the spray deposit.</b>	<b>101</b>

## List of tables

2.1	Experimental data of spray and other casting processes of Al-Si-Pb alloys and their characterization parameters of various investigators.	10
4.1	Values of various variables used in present study (a) related to gas (air) dynamics (b) related to spray forming/deposition.	23
5.1	Values of different experimental parameters in fig.5.10.	37
5.2	Theoretical density of Al-6Si-xPb alloys.	39
6.1	Gas discharge coefficient $C_D$ of atomizer with given experimental parameters.	80
6.2	Physical properties of Pb and Al.	90
6.3	Design matrix for hardness study.	97
6.4	Values of various parameters according to design matrix.	97
6.5	Effects of various parameters on hardness.	98
6.6	Design matrix for wear study.	103
6.7	Values of various parameters as per design matrix.	104
6.8	Effects of various parameters on wear rate.	104

## List of symbols

a	radial distribution coefficient	81
$a_0$	radial distribution coefficient at distance $h_0$	88
A	throat area of nozzle, $\text{mm}^2$	79
$A_s$	substrate area	81
B	constant	91
b, c & d	exponents	76
$C_D$	discharge coefficient of gas	79
$C_p$	specific heat capacity, J/Kg-K	90
$dT / dt$	solidification rate, K/s	91
FS	proof stress	99
h	substrate distance from atomizer, mm	87
$\Delta H$	latent heat of metal	90
K	constant	82
$\dot{m}$	mass flux of droplets/particles in the spray cone	81
$\dot{m}_A$	gas mass flow rate, kg/s	79
$\dot{m}_a$	actual mass flow rate of gas passing through the atomizer	79
$\dot{m}_{\max}$	maximum mass flux of droplets/particles in the spray cone	81
M	molecular wt. of gas	79
n	constant	91
p	plenum pressure, Pa	75
$\dot{Q}$	heat transfer rate	92
$r_s$	radius of substrate	81
R	universal gas constant	79
$r_{0.5}$	half width of the spray cone	82
$R_s$	distance from centre to periphery of the preform	97
r	radial distance from the axis of atomizer, mm	81
s	offset distance of the preform from atomizer axis, mm	85



T	temperature of the gas	79
$T_m$	melting temperature of metal ( K )	89
$t_{sol}$	solidification time of droplets	89
$t_{sph}$	sphereodization time of droplets	90
UTS	ultimate tensile strength, MPa	99
v	gas velocity	75
$v_z$	gas velocity at any location in the gas field	76
$v_{z0}$	maximum gas velocity at zero radial distance	76
z	axial distance from nozzle, mm	76
$\theta$	inclination angle of the substrate, deg.	82
$\gamma$	specific heat ratio of the gas	79
$\rho$	density of the metal (Kg/m <sup>3</sup> )	90
$\rho_g$	density of the gas, kg/m <sup>3</sup>	80
$\alpha$	spray cone angle, deg	83
$\mu$	viscosity of metal ( Pas )	90
$\sigma$	surface tension of melt (N/m)	90
$\lambda$	dendritic arm spacing, $\mu\text{m}$	91

## **CHAPTER -1**

# **INTRODUCTION**

---

Aluminum based alloys have the advantage of high strength to weight ratio, and therefore they are widely used in the automotive and aerospace industries. The liquid immiscible alloys based on Al-Pb system are potential materials for bearing alloys [1–21] because they possess superior performance like superior friction properties, low cost of production, high thermal conductivity and high corrosion resistance than other aluminum bearing alloys [2,5,11,12,21-23]. Lead is soft and much cheaper and more freely available than tin. Although, it is toxic but even then a number of research efforts are being made to achieve uniform and fine distribution of Pb in immiscible systems. It is due to the fact that the applicability of Pb dispersion cannot be dispensed with in critical area. However, the low melting point of lead places an upper limit on its operational temperature range. In addition, adding elements, such as Si, Cu and Sn to strengthen the Al matrix, the wear properties of Al-Pb alloys can be further improved [8,10]. Tin addition also improves the corrosion resistance of these alloys. Silicon is thought to have several benefits, including improved wear resistance, seizure resistance, strength of matrix and surface condition of the contact face [7,8,13].

Processing of Al-Pb alloys by the conventional casting techniques is difficult due to liquid immiscibility in a wide range of temperature and composition; and also large density difference of the constituent phases compared to Al alloys [3,8,11]. Early attempts to synthesize these alloys by the conventional casting routes had limited success. A slow cooling rate associated with conventional casting processes results in rapid separation of Al and Pb-rich phases [1,13,21]. In the past, several techniques, different from conventional casting, have been employed to prevent segregation of lead during melt solidification. Techniques based on powder metallurgy [2], stir casting [2,3,16], rheocasting [11], melt spinning [24], strip casting [14] and spray forming [13,21], results in a uniform distribution of lead particles in Al matrix. However, some

of these techniques are often associated with either a higher energy consumption or generation of coarse grain microstructures. Among these techniques, spray forming possesses several advantages in effective microstructural control together with producing a near net shape [25-32] preform in a less number of processing steps. Rapid cooling associated with solidification of atomized droplets and a turbulent fluid flow condition on the deposition surface minimizes the separation of the Al- and Pb-rich phases [13, 33].

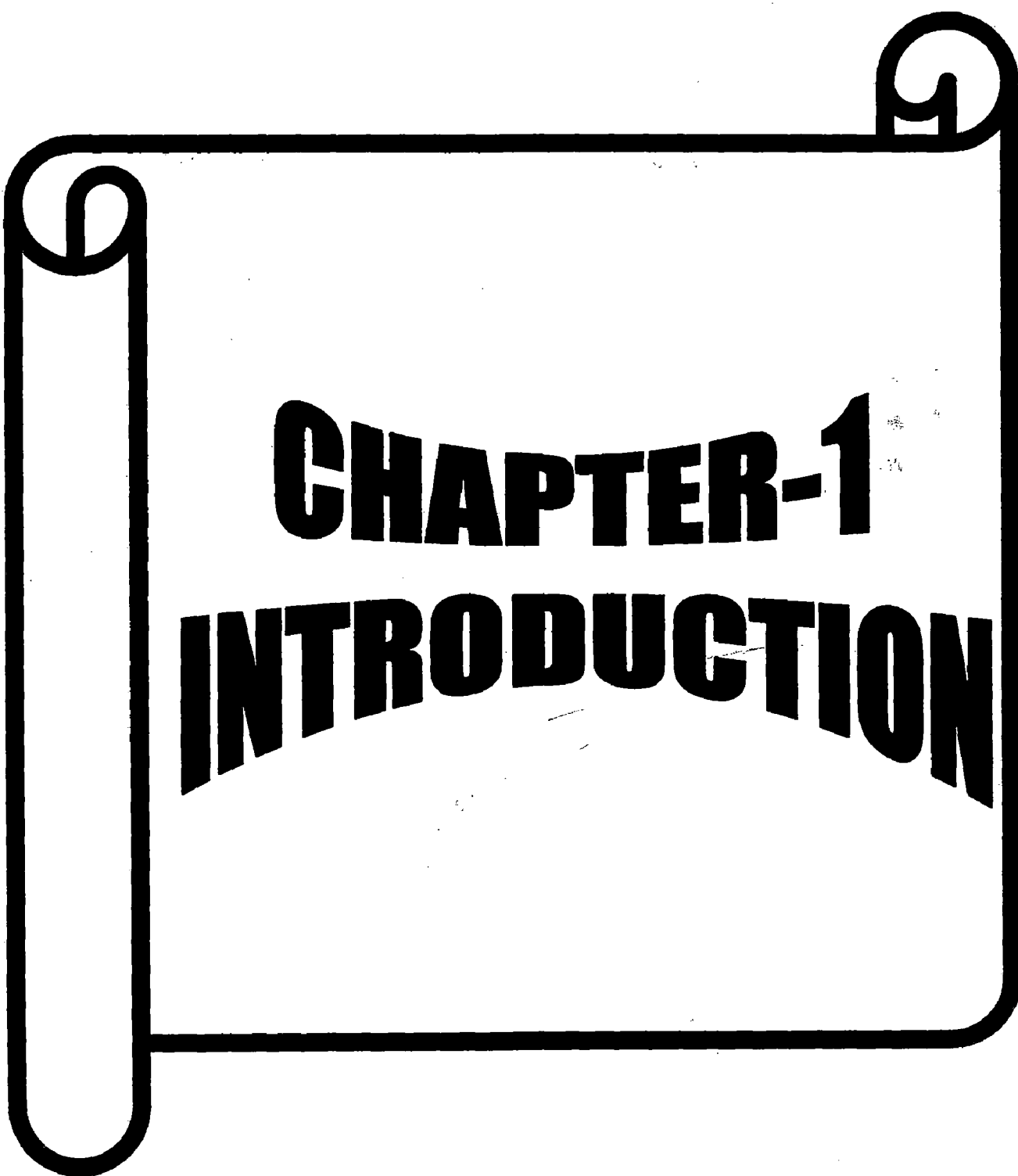
Spray forming is essentially a two-step process route that involves [34-36]:

- (a) Disintegration (atomization) of the molten metal by inert gas into micron-sized droplets.
- (b) The subsequent deposition of the mixture of solid, liquid and partially solidified droplets on a substrate surface. These droplets eventually collect as a coherent mass and the microstructure of this mass is largely dictated by the solidification conditions of the droplets during impact. Almost similar steps are used in thermal spraying [37,38] process.

Above mentioned steps make spray forming a potentially attractive manufacturing route for the following reasons [36]:

1. The fast heat extraction during atomization limits large scale segregation and associated coarsening phenomena.
2. The inert conditions required for atomization and deposition minimize surface oxidation and other harmful surface reactions.
3. This process can potentially be used to produce near net-shape products and thereby reducing the cost of production.

During spray atomization and subsequent deposition a detailed study of the solidification mechanisms that govern the evolution of microstructure is very complex due to the extreme differences in thermal environment both before and after impact of the droplets with the deposition surface. During spray atomization, the violent and/or rapid extraction of thermal energy by the atomization gas promotes the formation of highly refined grain structures [21]. In contrast, during subsequent deposition the solidification conditions are governed by relatively slow cooling rates [13,39]. The microstructure of spray-atomized and deposited materials is generally reported to exhibit spheroidal or "equiaxed" grains, a feature that is consistently observed

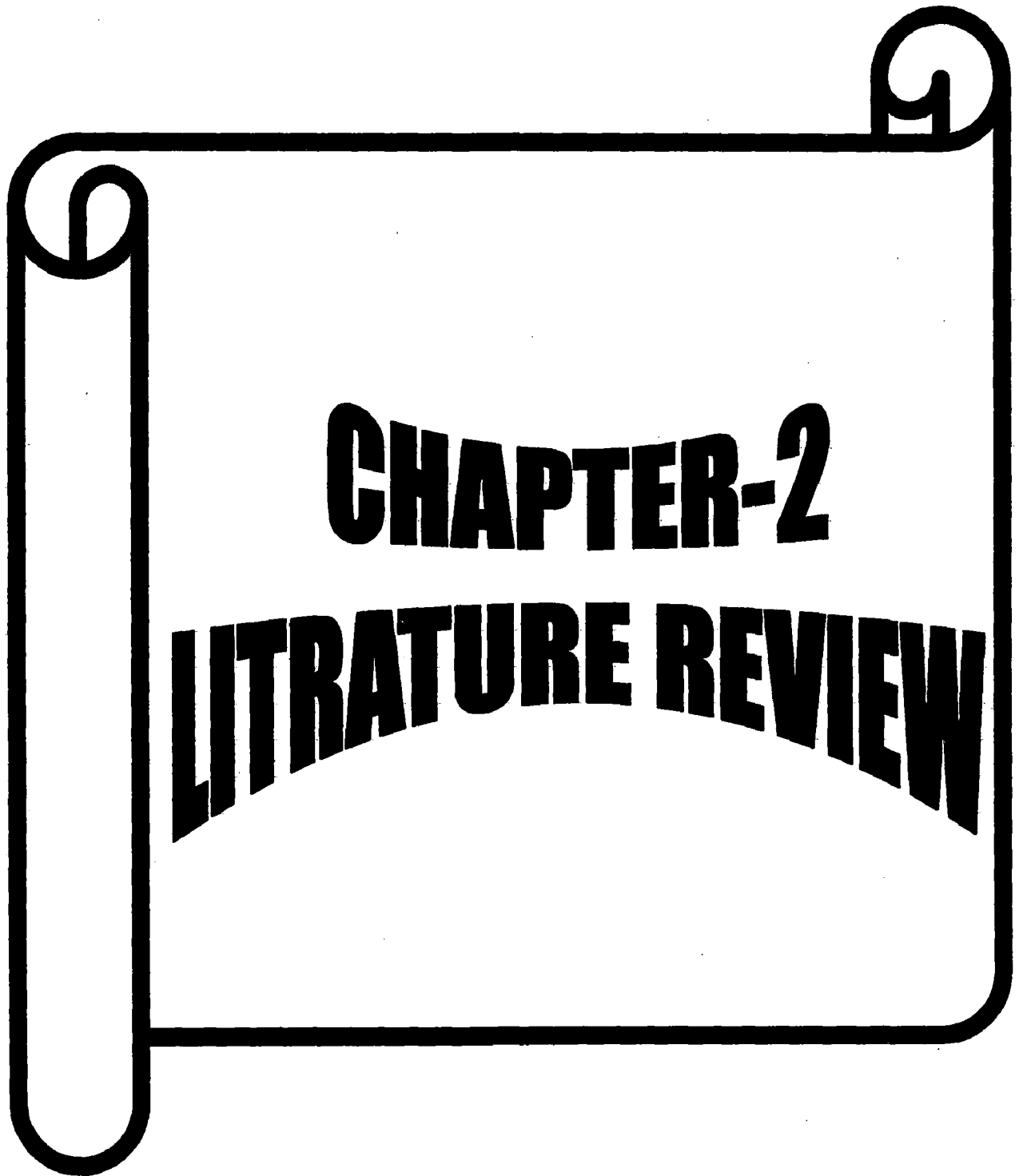


**CHAPTER-1**  
**INTRODUCTION**

regardless of alloy composition [34,40]. In fact, spray atomization and deposition processing exhibits the beneficial characteristics of powder metallurgy processing without the numerous processing concerns, that is, powder production, storage and handling, sintering and hot consolidation.

Various shapes like disc [27,41], billet [25,42-45], tube [25] and ring [28] can be produced by this process. The disintegrated or atomized droplets during the process follow a particular distribution [25-29] and therefore some special arrangements are required to produce aforementioned shapes of desired dimensions. The produced part also has some porosity [46-49] which can be shrinkage porosity, gas porosity etc.

In the present work Al-Si-Pb alloys were spray formed in the form of a disc and then their characteristics such as shape, microstructure, porosity, hardness, strength, wear etc. were studied. The whole work is divided into several chapters from 1 to 8. Next chapter (Chapter-2) deals with the literature survey related to this work. Chapter-3 comprises of the problem formulation. Chapter-4 is related to experimental set-up and procedure carried out to achieve objectives of the present study. Chapter-5 consists of the results obtained and chapter-6 is on the discussion of the work. The conclusions and scope for future work are reported in chapter-7 and 8, respectively.



# **CHAPTER-2**

# **LITRATURE REVIEW**

## **CHAPTER -2**

# **LITERATURE REVIEW**

---

Spray forming involves a number of design and operating process parameters which can affect the characteristics of spray deposit or preform. The design parameters are related to the design of atomizer or nozzle, which are throat diameter of nozzle, slit width of nozzle and apex angle [50,51] etc. Operating parameters are gas pressure, type of gas, alloy or melt composition, melt temperature, nozzle to substrate distance, tilt angle of substrate etc. Taking these parameters into consideration, this chapter is divided into the following sections to review the spray forming process and Al-Si-Pb preform characteristics: atomizer design, gas field of atomizer, droplet solidification, preform shape, Al-Si-Pb preform characteristics like microstructure, hardness, strength, wear rate etc.

### **2.1 ATOMIZER DESIGN**

In case of gas atomizer two types of atomizers viz free fall [52-55] or confined [50,51] type are used to disintegrate the liquid metal into droplets. Out of these two, confined type atomizers are primarily used in spray forming due to their advantages over free fall type atomizers. A conventional confined type atomizer is shown in **fig. 2.1**. It consists of a convergent or convergent- divergent nozzle concentric to melt delivery tube and therefore forming an annular slit for gas exit around the delivery tube. The opposite axes of slit intersect at a common point, called as focal point [56] or geometric point [57] or geometric focus [58,59] of the atomizer.

### **2.2 GAS FIELD OF ATOMIZER**

Gas jet issuing from annular slit of atomizer forms a gas field of widely varying velocities around the geometric point. These velocities were measured as a function of the parameters like plenum pressure, axial and radial distances etc. using pitot tube, hot

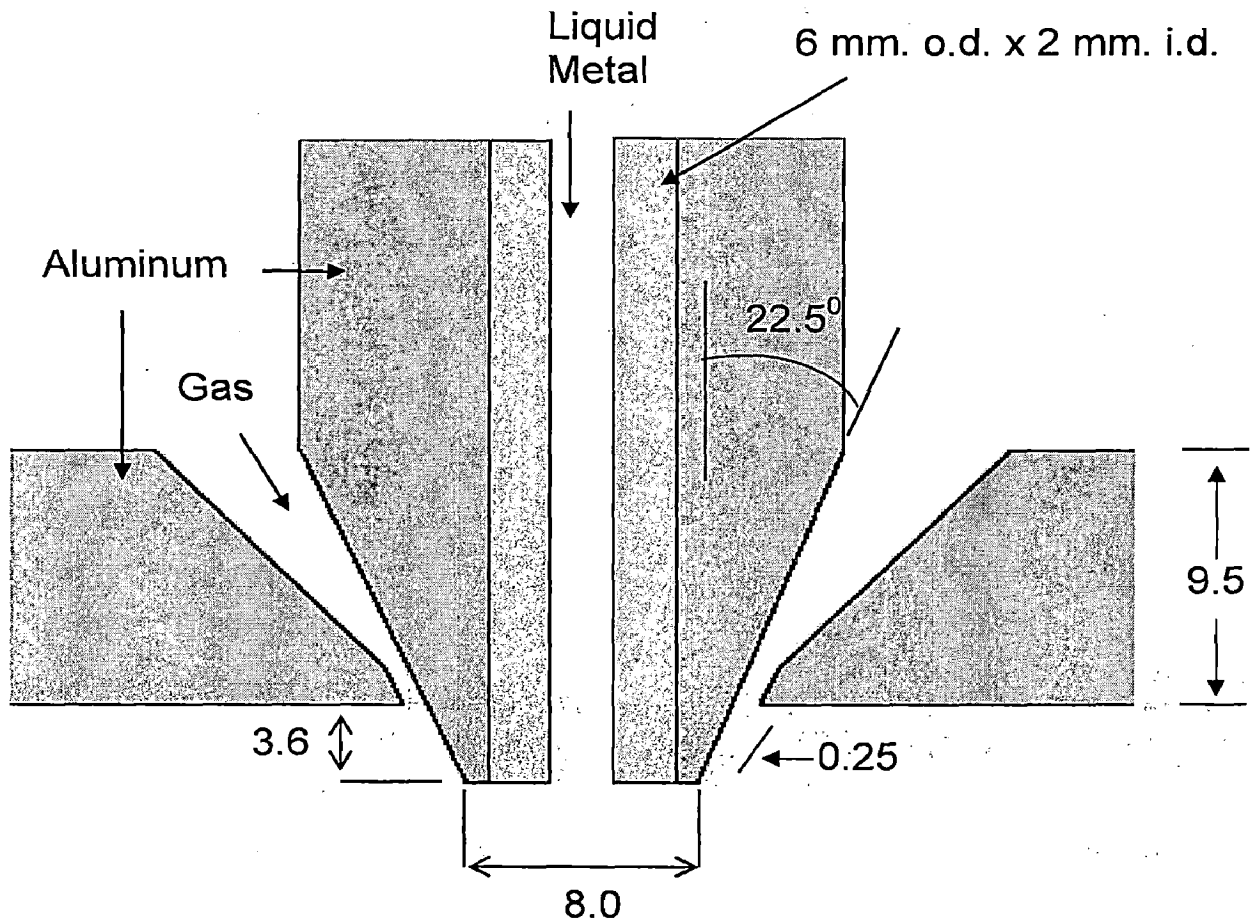


Fig. 2.1 A conventional confined type atomizer [60].

wire anemometry etc. by various workers [50,51,56-58]. Some empirical correlations are available to determine these velocities, for example:-

The velocity decay with axial distance is given by the following equations [61-63]

$$V_z = V_{z_0} \exp\left(-\frac{Z}{Z_{c1}}\right) \quad (2.1)$$

$$V_z = V_{z_0} \left(1 - \frac{Z}{Z_{c2}}\right)^2 \quad (2.2)$$

$$V_z = V_{z_0} \left(\frac{Z_{c3}}{Z + Z_{c3}}\right)^3 \quad (2.3)$$

$$\frac{v_z}{v_{z_0}} = 6.2 \left(\frac{D}{z}\right) \quad (\text{for } 7 < z/D < 1000) \quad (2.4)$$



and with radial distance the velocity decay is given by

$$\log\left(\frac{v_z}{v_r}\right) = v_{z0}\left(\frac{r}{z}\right)^2 \quad (\text{for } 7 < z/D < 100) \quad (2.5)$$

For a free fall type atomizer the velocity decay is given by the following equation [52].

$$V_z = \frac{5.58 \times 10^{-4} D^{0.48} P^{0.96}}{F^{0.75}} \quad (2.6)$$

Where,  $v_z$  is the jet centre line velocity at a distance  $z$  from the gas nozzle along its axis,  $v_{z0}$  is initial jet velocity,  $D$  is gas nozzle diameter and  $v_r$  is the jet velocity at a radius  $r$  from the jet axis. Constants  $Z_{C1}$ ,  $Z_{C2}$  and  $Z_{C3}$  are functions of the initial gas velocity.  $P$  is plenum pressure and  $F$  is the focal length.

So, there are at least two separate equations to determine gas velocity in both axial and radial directions of the gas field.

## 2.3 DROPLETS SOLIDIFICATION

Melt droplets of various size forms as gas jet from the atomizer impinge on the melt stream. These droplets collected as powder particles follow the log-normal size distribution and their shape is given by an empirical equation as reported by Nichiparenko and Naida [65].

$$t_{sph} = \frac{3\pi^2 \mu_m}{4V\rho_m} (R_p^4 - r_p^4) \quad (2.7)$$

Lubanska [66] studied the atomization behaviour of molten iron using a spray ring type atomizer and proposed the following correlation to predict mass median size of powder particles collective.

$$X_g = K \left[ \frac{\mu_m \rho_g \gamma_m d}{\mu_g \rho_m^2 V_g^2} \left( 1 + \frac{M}{m} \right) \right]^{1/2} \quad (2.8)$$

The powder yield in different size range of the collected powder is given by the following log-normal distribution function [67].

$$\frac{dW}{dX} = \frac{1}{\sqrt{2\pi} x \ln \sigma_g} \exp \left[ - \left( \frac{\ln x - \ln x_g}{\sqrt{2} \ln \sigma_g} \right)^2 \right] \quad (2.9)$$

The droplets of various sizes will solidify at different distances from the atomizer to form this powder. Mathematical models [30,39,61,68-71] were developed to determine the solidification distance and cooling rate etc, of these droplets. In spray forming the substrate should be kept at such a distance so that there is fully solidification of droplets but there is sufficient liquid 50-70 % [29] or 30-60% [32] or 20-60% [72] or 40% [73] reaching in the deposit to get a coherent preform. The cooling rate of the droplet decides its microstructure like grain size, secondary dendrite arm spacing etc [21,33,39,74-78] which in turn can affect the microstructure of the preform.

## 2.4 PREFORM SHAPE

Atomized droplets in spray cone follow the Gaussian mass distribution [25-29] about the cone axis. Therefore, the preform produced by these droplets will follow the same distribution in terms of its shape if substrate is kept normal to the spray cone axis at its centre. Other shape can be produced by different arrangements of either atomizer or substrate. Different types of shapes which can be produced by spray forming process are discs, billets, roads, pipes, sheets etc. These shapes should be produced to near-net-shape to avoid machining. Disc [27,41] and billet [25,43] shape parts were claimed to be that of near-net-shape by some workers. Tilting of either atomizer or substrate from vertical axis was used to produce the near-net-shape of these parts. Disc shape was generally non-uniform in thickness. Mathematical models were also given by some workers to produce billet shape [42-45].

## 2.5 Al-Si-Pb PREFORM CHARACTERISTICS

There is not much literature available on Al-Si-Pb spray formed alloys and their characteristics. Experimental data of spray and other casting processes of Al-Si-Pb alloys and their characterization parameters of various investigators are reported in

**table 2.1.** The processes parameters include the alloy composition, gas pressure used for spray forming, melt temperature of the alloy and deposition distance i.e. distance between atomizer and substrate. The alloy characterization parameters include the microstructure of the alloy, its porosity, applied wear load, sliding speed during wear, wear rate, coefficient of friction, spray formed or cast alloy, its hardness, stress and percent elongation to fracture.

An. et al. [2,3] have investigated the wear behavior of as-cast and hot extruded Al-Si-Pb alloys under dry conditions using a pin-on-disc type wear testing machine. The results shown almost constant wear rate at intermediate load levels. The wear rate in Al-Si-Pb alloys was found to decrease with increasing lead content. Better resistance to seizure for Al-Si-Pb alloys with more than 15 wt% lead were observed due to a film of lubricant covering almost the entire worn surface. This film was a mixture of different constituents containing Al, Fe, Si, O and Pb. Pathak et al. [6] studied the wear characteristics of a series of leaded aluminum bearing cast alloys under dry sliding conditions under a room atmosphere using a pin-on-disc-type wear testing machine. The wear volume was measured as a function of the alloy composition, sliding distance, normal load and sliding velocity. Optical and scanning electron microscopic examinations of the test specimen, wear track and wear debris were carried out to aid in the elucidation of the wear mechanisms. It was observed generally that the wear rate decreased with increasing lead content and hardness of aluminum-based alloys. They also have studied the antiseizure and antifriction characteristics of a number of Al-Si-Pb as cast alloys with silicon contents in the range 2-20 wt.% and lead contents in the range 0-10 wt.% under different lubrication conditions using a bearing test machine [7]. The addition of lead to aluminum-silicon alloys was generally found to reduce interfacial friction and improve their ability to resist seizure. A lower friction coefficient and a higher seizure load were obtained for Al-Si-Pb alloys bearing in semi-dry sliding conditions compared with those were observed for dry conditions.

Sharma and Rajan [8] investigated the coefficient of friction characteristics of cast aluminum-silicon alloy with varying lead content from 4 to 16 wt.% under lubricated, semi-dry and dry conditions. The average value of coefficient of friction in the oil-lubricated test was lower as compared with semi-dry and dry tests. In general

**Table 2.1** Experimental data of spray and other casting processes of Al-Si-Pb alloys and their characterization parameters of various investigators

Reference	Process parameters				Pre-form characterization parameters											
	Composition in Al (wt%)	Spray / Cast	Gas pressure (kPa)	Melt temperature (°C)	Deposition distance (cm)	Micro-structure (grain / particle size, μm)			porosity (%)	Load (N)	Sliding speed (m/s)	Wear Rate (m <sup>3</sup> /mx10 <sup>-13</sup> ) Fricion coeff.	Hardness	Stress (MN/m <sup>2</sup> ) proof UTS	Elongation (%)	
2.	4Si-1Cu 10-25Pb	Cast				Al	Si	Pb	4.3-25.2	180-300			45-34	160-79	4.3-0.5	
3.	4Si 1Cu 10-25Pb	Cast							4.3-25.2	20-240	0.79		45-34	160-79	4.3-0.5	
6	2-20Si 2-10Pb	Cast								5-150	0.25-3.0	5-60	32.4-81.0	39.1-82.5	111.6-186.2	2.5-16.4
7	2-20Si 2-10Pb	Cast								600	0.073		32.4-79.0	39.1-77.8	111.6-186.2	2.8-16.4
8	12Si 4-16Pb	Cast								100-600	0.57		54-38 (BHN)		165-132	7.2-10.0
9	12Si 4-16Pb	Cast		697						5-40	0.51	13-87			165-132	7.2-10.0

11	7Si 3.8-17.2 Pb	Cast		750													90-150	190-260	4.8-15
13	10Si 0, 20Pb 3.5Cu	Spray	1000	750-850	35-55	10-25	0.5-5	0.1-25	10-90	1.0	7-45	0.22-0.57							
21	11.5-18Si 10-15Pb	Spray	1600	730 -850	50	35											110.7-121.5	143.2-165.8	13.4 -8.3
23	2-20Si 2-10Pb	Cast							10-150	0.25-3.0	5-110						32.4-81.0	111.6-189.7	2.5-16.4
33	10Si 20 Pb 3.5Cu	Spray	1000	850	45		<5	0.5-25		0.5-2	7.5-38.7	0.25-0.57							

Copyright © 2015, Emerald Group Publishing Limited

Copyright © 2015, Emerald Group Publishing Limited

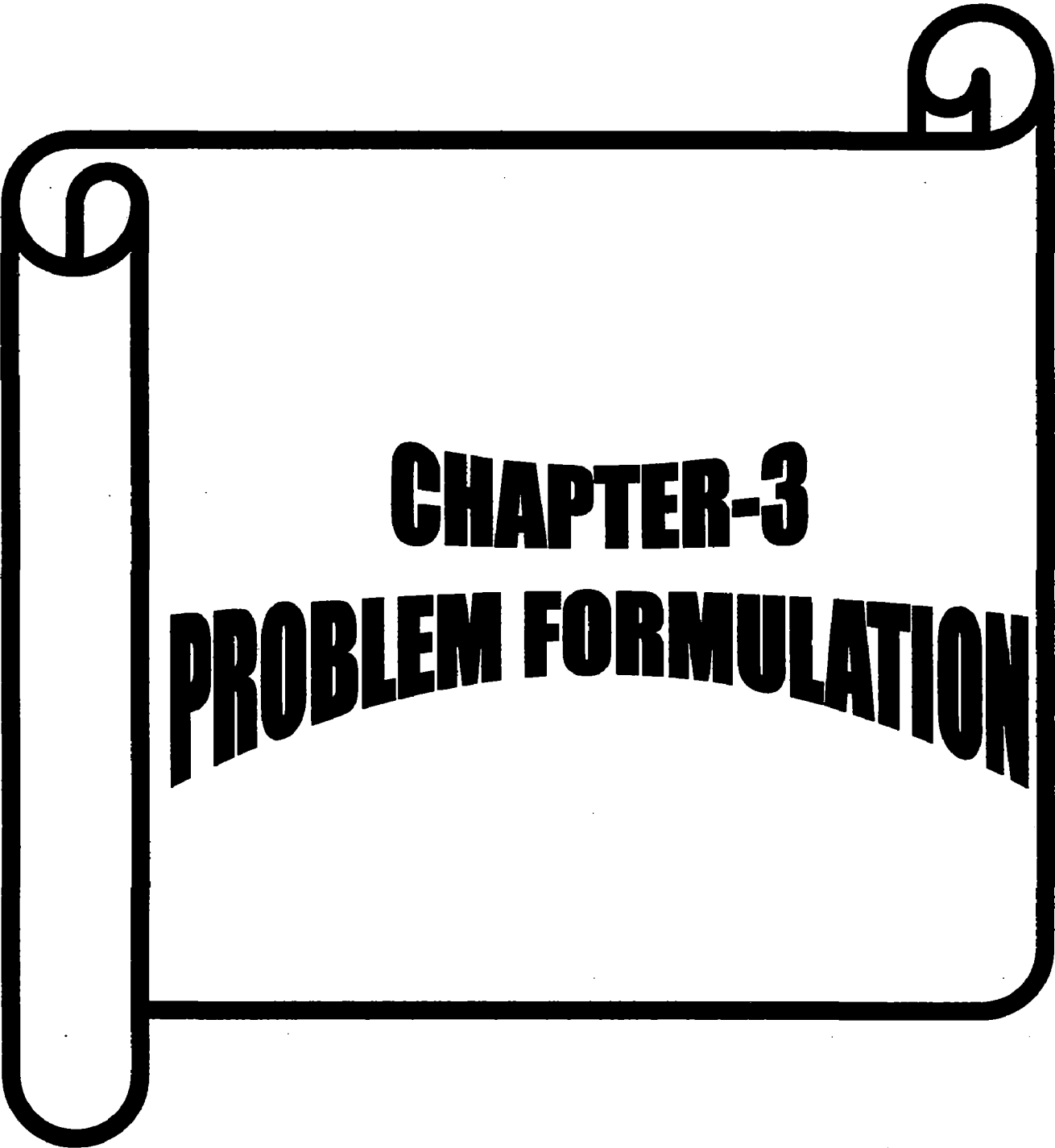
the influence of morphology of microstructure, lead distribution and addition of lead was found helpful in reducing interface friction. They also studied [9] wear of Al-12Si and Al-12Si-1Cu-1.5Mg alloys along with varying amounts of lead (from 4 to 16 wt.%). Wear experiments were conducted on a pin-on-disc machine. The worn-out test pin surface topography, sub-surface damage and debris were studied by scanning electron microscope (SEM). The worn-out test pin surfaces for all the alloys showed a multitude of distinct topographical features in the SEM images. It was found that a number of wear processes, such as delamination, adhesion and abrasion, take part in removal of metal as debris, and no single wear process is responsible for metal removal from sliding surfaces. The presence of lead in base alloys was found to reduce wear and friction.

Fang and Fan [11] successfully produced immiscible Al-Si-Pb alloys using the rheo-diecasting process (RDC). The microstructure of RDC Al-Si-Pb alloys was characterized by spherical and fine Pb particles dispersed uniformly in the Al-Si alloy matrix. The size of the  $\alpha$ -Al primary phase was approximately 50  $\mu\text{m}$  and the average size of the Pb particles increased with the increase in Pb concentration. The Pb particle size increased from 2.6  $\mu\text{m}$  in Al-7Si-3.8Pb to 14  $\mu\text{m}$  in Al-7Si-17.2Pb alloy. It was also found that both the ultimate tensile strength and elongation of Al-Si-Pb alloys decreased with increasing Pb content.

Rudrakshi et al. [13] spray formed Al-Si-Cu-Pb at a gas pressure of 1.0 MPa and the nozzle to substrate distance was varied from 0.35 to 0.55 m. The microstructure and wear characteristics of the spray-deposits were investigated. The results invariably exhibited an equiaxed grain morphology of the primary  $\alpha$ -phase with variation in grain size from 10 to 25  $\mu\text{m}$  in addition to a uniform dispersion of ultra-fine particles of lead and globular silicon particles in Al-matrix. The size of Si particles varied from 0.5 to 5  $\mu\text{m}$  and that of Pb particles from 0.1 to 25  $\mu\text{m}$  with variation in deposition distance. The microstructural variation was also observed in different regions of the deposit. The atomized powder particles revealed two different types of microstructures, the one showing a cellular-dendritic morphology of the primary  $\alpha$ -phase whereas the other exhibited fine spherical Al-particles dispersed in the matrix of Pb-rich phase. The wear rate and the coefficient of friction of Al-Si-Cu-Pb alloy were observed to be lower than that of Al-Si alloy at loads varying from 10 to 90 N at a sliding velocity of 1.0 m/s.

Rudrakshi et al. [33] also have studied the wear behaviour of same alloy in different environmental conditions. The wear tests were carried out in air atmosphere and vacuum, using a pin-on-disc type wear testing equipment. The wear behaviour in air atmosphere clearly indicated the influence of surface oxidation on the mating surfaces. This resulted in the formation of irregular shaped oxide particles having bright contrast in SEM investigation of worn surfaces and debris particles. The nature of variation in wear with sliding distance, both in air atmosphere and vacuum, remained similar showing two distinct wear regimes, viz., running in wear and steady state wear. A relatively lower running in period and a large reduction in the frictional force were observed in vacuum as compared to that obtained in air under same conditions of sliding speed and applied pressure. The wear rate varied from  $(0.25 \text{ to } 0.61) \times 10^{-12} \text{ m}^3/\text{m}$  for a range of applied pressure of 0.2–1.8 MPa and at a constant sliding speed of 1.0 m/s in vacuum, whereas, the wear rates observed in air atmosphere for the same sliding conditions range between  $(0.75 \text{ and } 3.87) \times 10^{-12} \text{ m}^3/\text{m}$ . The coefficient of friction in air atmosphere varied for low pressures and remained almost constant at 0.25 in high pressure regime, whereas in vacuum it decreased linearly and finally attained a constant value of 0.1. The wear rate increased with sliding speed in vacuum, on the other hand, in air atmosphere the wear rate decreased with increasing sliding speed, reaching a minimum at a critical sliding speed and then increasing with further increase in sliding speed. The coefficient of friction remained almost constant for different sliding speeds for both air and vacuum. However, under vacuum, the value of coefficient of friction was lower than that in air, through the range of sliding speed.

Yu. et al. [21] produced Al-11.5Si-15Pb and Al-18Si-10Pb alloys by liquid phase co-spray forming. Some deposit was extruded and then microstructure and tensile properties were studied. Torabian et al. [23] studied wear characteristics of Al-Si-Pb alloys with silicon content from 2 to 20 wt% and lead from 2 to 10 wt% using a pin-on-disc type wear testing machine at room temperature. The effects of applied load, sliding velocity and alloy composition on wear rate of Al-Si-Pb alloys were investigated. It was found that wear rate strongly depend on alloy composition, applied load and sliding speed. Wear rate decreased and load bearing capacity of the alloy increased with the increase in lead content. Wear rate of Al-Si-Pb alloys initially decreased and then increased with the increase in sliding speed.



**CHAPTER-3**  
**PROBLEM FORMULATION**

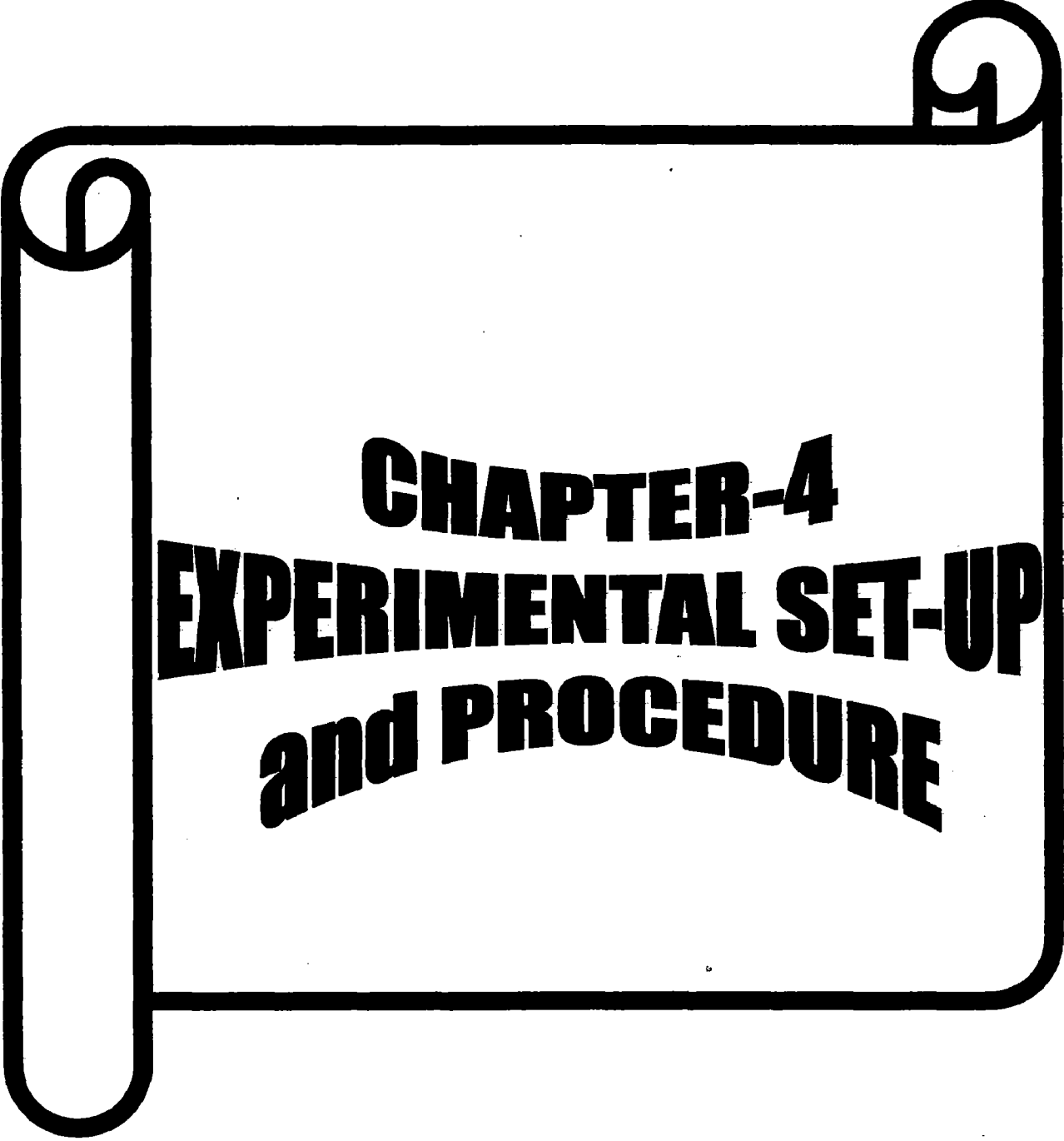


# Problem Formulation

After reviewing the literature critically and with the importance of Al-Si-Pb alloys, the scope of the problem and objectives of the present study have been formulated which are as follows:-

1. To design a confined convergent divergent nozzle to increase the thickness uniformity of disc shape preform (spray deposit). The idea is to shift more particles/droplets towards periphery, or gas should not push particles/droplets towards central axis of atomizer because more thickness of preform is observed at the centre.
2. To characterize qualitatively and quantitatively the atomizing gas field produced by the designed nozzle which is different from the conventional nozzle and to correlate by single equation the gas velocity in the gas field with maximum gas velocity, axial distance and radial distance from the atomizer axis.
3. To study the thickness uniformity of the disc shape preform.
4. To study the density and porosity variation in Al-Si-Pb preform of different compositions.
5. To study the microstructure of Al-Si-Pb preform of different compositions.
6. To study the mechanical properties like hardness, strength of the Al-Si-Pb preform of different compositions.
7. To study the tribological properties like wear rate, coefficient of friction of the Al-Si-Pb preform of different compositions.

It should be noted that in present study alloy composition and /or the process used is different from that of the literature.



**CHAPTER-4**  
**EXPERIMENTAL SET-UP**  
**and PROCEDURE**

## CHAPTER -4

# EXPERIMENTAL SET-UP and PROCEDURE

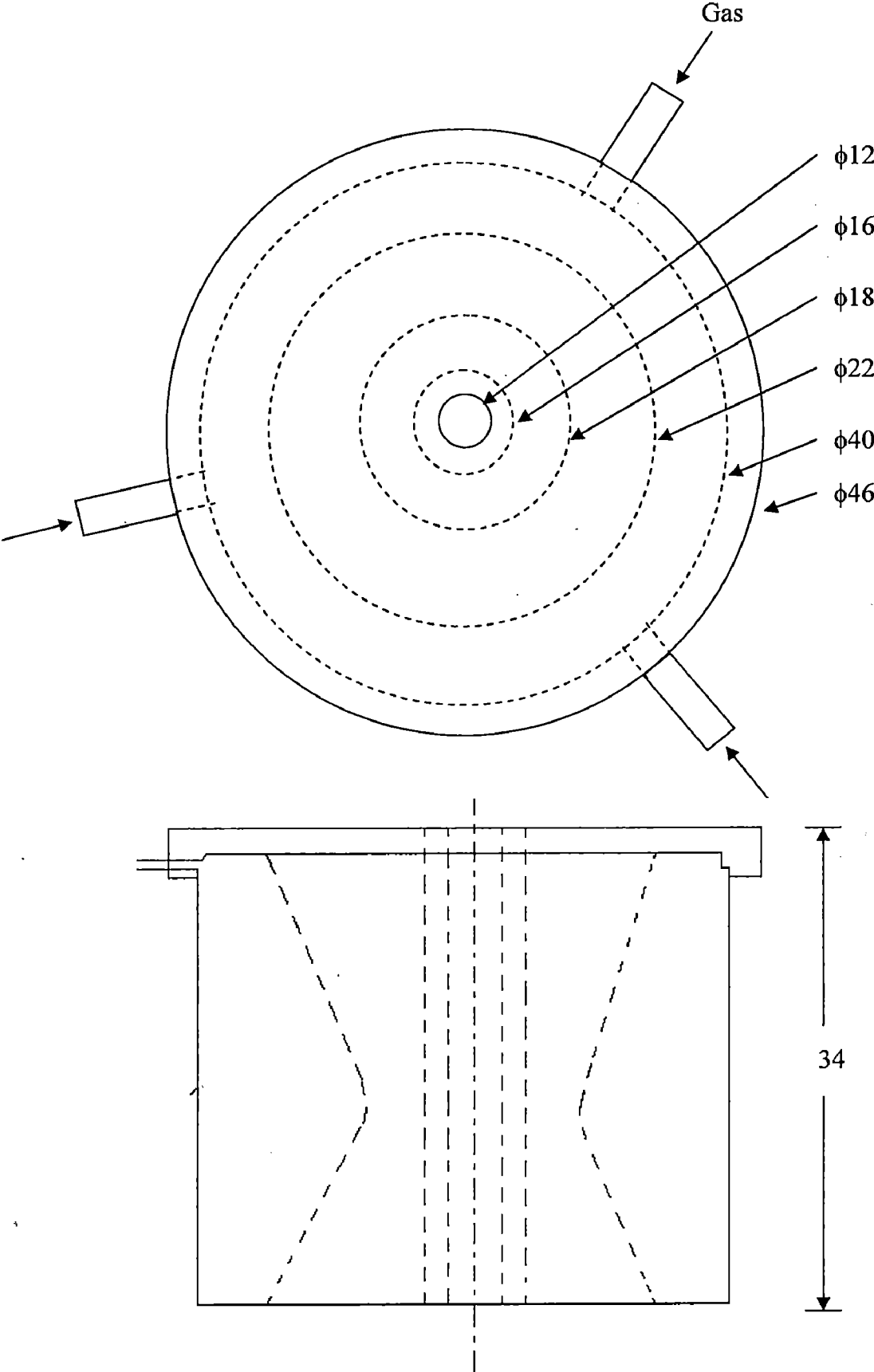
---

This chapter consists of three main parts viz. (1) atomizer characterization (2) spray deposition of Al-Si-Pb alloys and (3) characterization of the spray deposit (preform). Gas dynamic behavior of air and nitrogen are almost similar, therefore for atomizer characterization by gas dynamics, where a large amount of gas is required, air was used. Whereas for spray forming nitrogen gas was used because air can cause oxidation of Al-Si-Pb alloys.

## 4.1 ATOMIZER CHARACTERIZATION

### 4.1.1 Atomizer design

The design of an atomizer used in present study is shown in **fig.4.1** and its photograph is shown in **fig.4.2**. This atomizer falls in the category of confined type atomizer in which gas interact with the melt as it leaves the melt delivery tube. But, the design is slightly different from that of the conventional confined type atomizer (**fig.2.1**). In conventional atomizer opposite axes of annular slit or discrete nozzles intersect at a common point, whereas in the present nozzle axes are parallel i.e. they do not intersect. Therefore, in conventional design gas compress the melt stream towards its central line or axis of atomizer. Whereas, in present case the gas stream will be parallel to the melt stream or it will not compress the melt stream. The outer and inner diameters at the throat are 16 and 18 mm, respectively and hence the throat width is 1.0 mm which is required to calculate the maximum mass flow rate through the atomizer.



All dimensions are in mm

Fig. 4.1 Design of the atomizer.

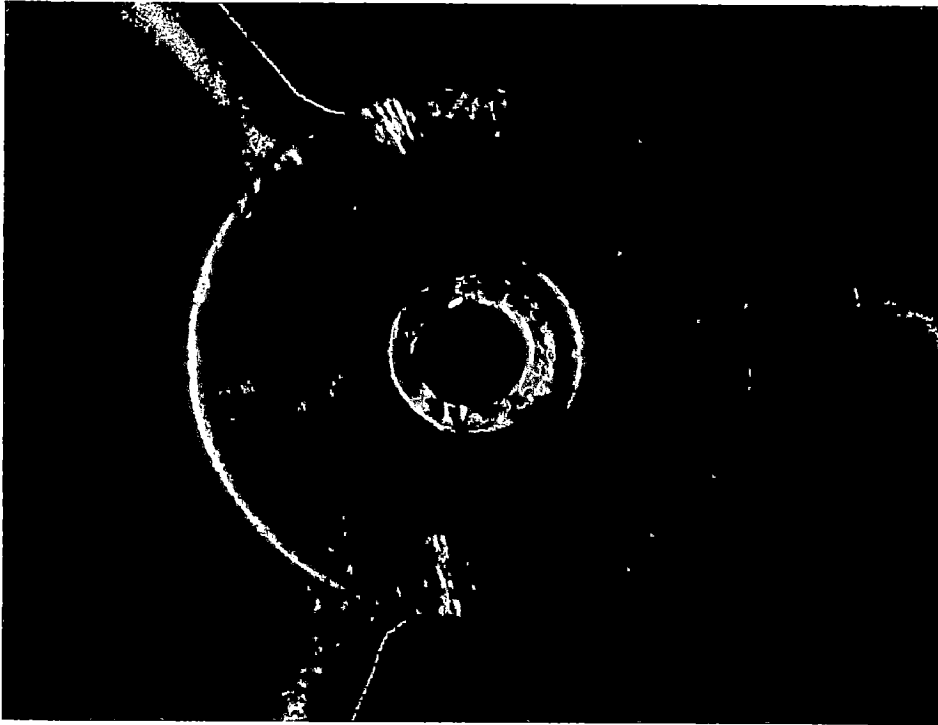


**Fig. 4.2** Photograph of atomizer used in gas dynamics study and spray forming.

### **4.1.2 Gas velocities from the atomizer**

The experimental set-up used to measure the gas velocities in the gas field created by the atomizer is shown in **fig.4.3**. This set-up primarily consists of an atomizer, a Pitot tube, a manometer, a rotameter, a pressure transducer and a three-way-traversing mechanism to hold and move the Pitot tube in three perpendicular directions.

Pressure at the inlet of the atomizer was measured by means of a calibrated pressure transducer (see **fig.4.3** for its location), and it is termed as 'Plenum pressure', while the pressures in the air field around the central axis of the atomizer were measured by a Pitot tube connected to a mercury manometer. The pressures measured by Pitot tube were converted to jet velocity using procedure reported elsewhere [52,58,80]. The Pitot tube was fixed on a traversing mechanism which was placed outside the air field to avoid any interference with measurement as shown in the figure.

By means of knobs on the traversing mechanism, it was possible to move the tube spatially within the air field. The accuracy of the movement of the tube was  $\pm 0.1$  mm.

### 4.1.3 Gas flow rate through atomizer

The flow rate of gas was measured by a calibrated rotameter (location of rotameter is shown in the fig 4.3). Depending on throat diameter of the nozzle an air compressor gave a sustained air supply at the maximum plenum pressure of 20 bar.

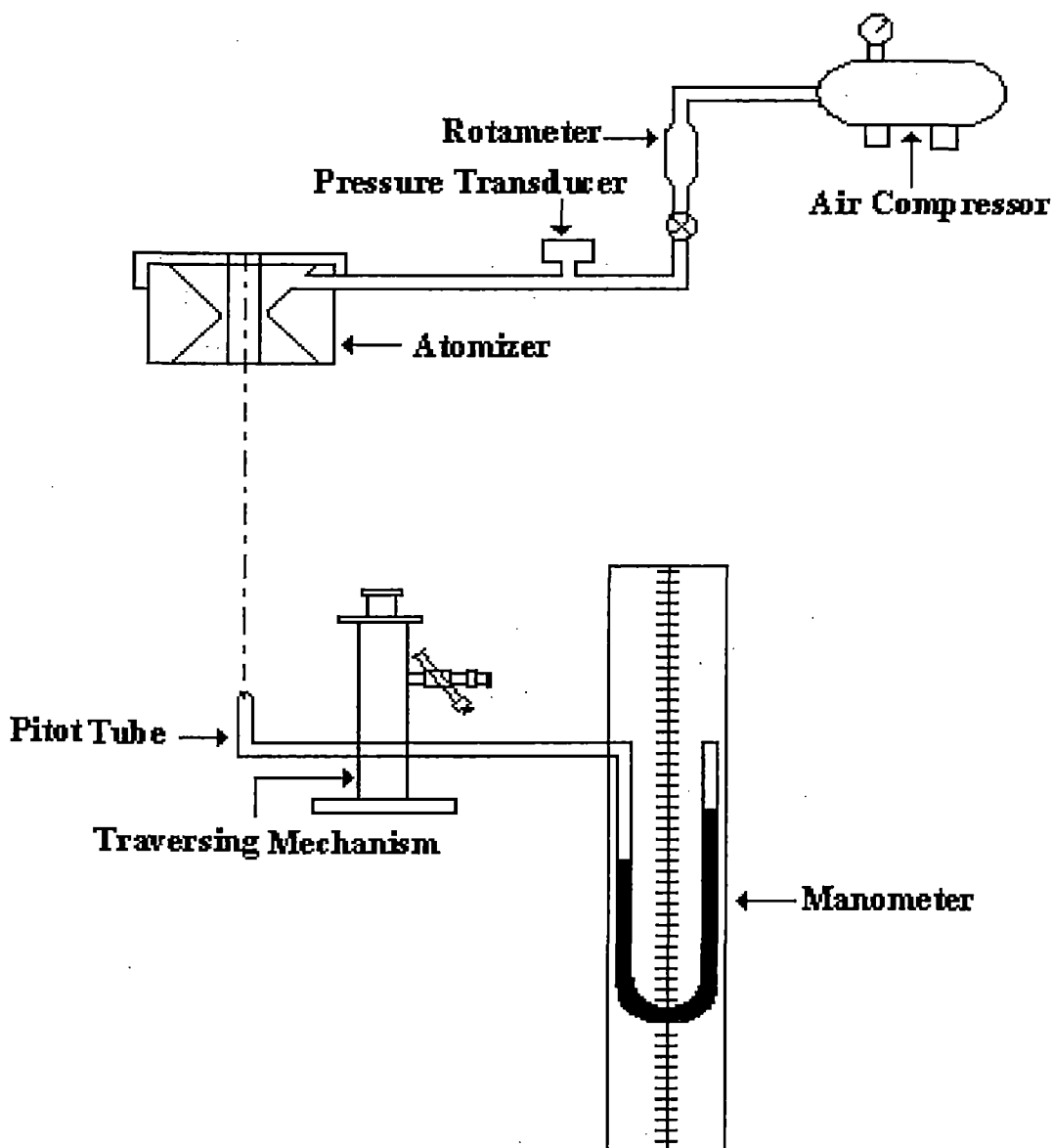


**Fig.4.3** Schematic of the gas dynamics.

## 4.2 SPRAY DEPOSITION OF Al-Si-Pb ALLOYS

A Schematic of spray forming set-up is shown in **fig.4.4**. The alloy was allowed to melt into a graphite crucible placed inside a furnace as shown in the figure. At centre of the bottom of crucible an exchangeable graphite melt delivery tube was fitted to produce melt flow stream. A stopper rod was used to either open or close the entrance of the delivery tube. Other end of delivery tube was fitted into the atomizer which was placed above the cooling chamber. Design of atomizer is described in section 4.1.1. Height of cooling chamber was 1500 mm. The stopper rod was raised up after starting the gas flow in atomizer to start the atomization of melt and thereby spray deposition. Vertically falling liquid metal stream interacts with high energy gas jet at the tip of melt delivery tube which promotes the atomization of melt into spray of small size droplets. This atomization takes place inside the cooling or spray chamber and atomized droplets were deposited over a copper substrate which can be placed at a different distances from the atomizer. Copper substrate can be inclined at desired angle from the horizontal axis and also can be rotated at varying rpm to get a uniform shape of preform. Overspray powder was collected over a tray placed at the bottom of cooling chamber.

The base alloy used in the present work consisted of Al-Si alloy having 12% and 24% Si. The alloy was super heated to  $200^{\circ}$  C above its melting temperature in graphite crucible using an induction furnace. Different amount of lead and Al were added in this Al-Si alloy to make Al-6Si-xPb and Al-12Si-xPb (where, x= 0, 10, 15, 20 and 25) alloys. In each run 800 gm of Al-Si-Pb alloy was taken in the crucible. Nitrogen gas was supplied for atomization prior to melt flow. The atomization was carried out at a  $N_2$  gas pressure of 10 bar. The details of the process variables are given in **table 4.1**. The spray droplets were deposited over a rotating (240 rpm) copper substrate which was either inclined to  $0^{\circ}$ ,  $15^{\circ}$  or  $30^{\circ}$  and offset either at a distance of 0 or 40 mm from central axis of the atomizer to achieve a disc shape preform. This preforms was taken out of the substrate after deposition.

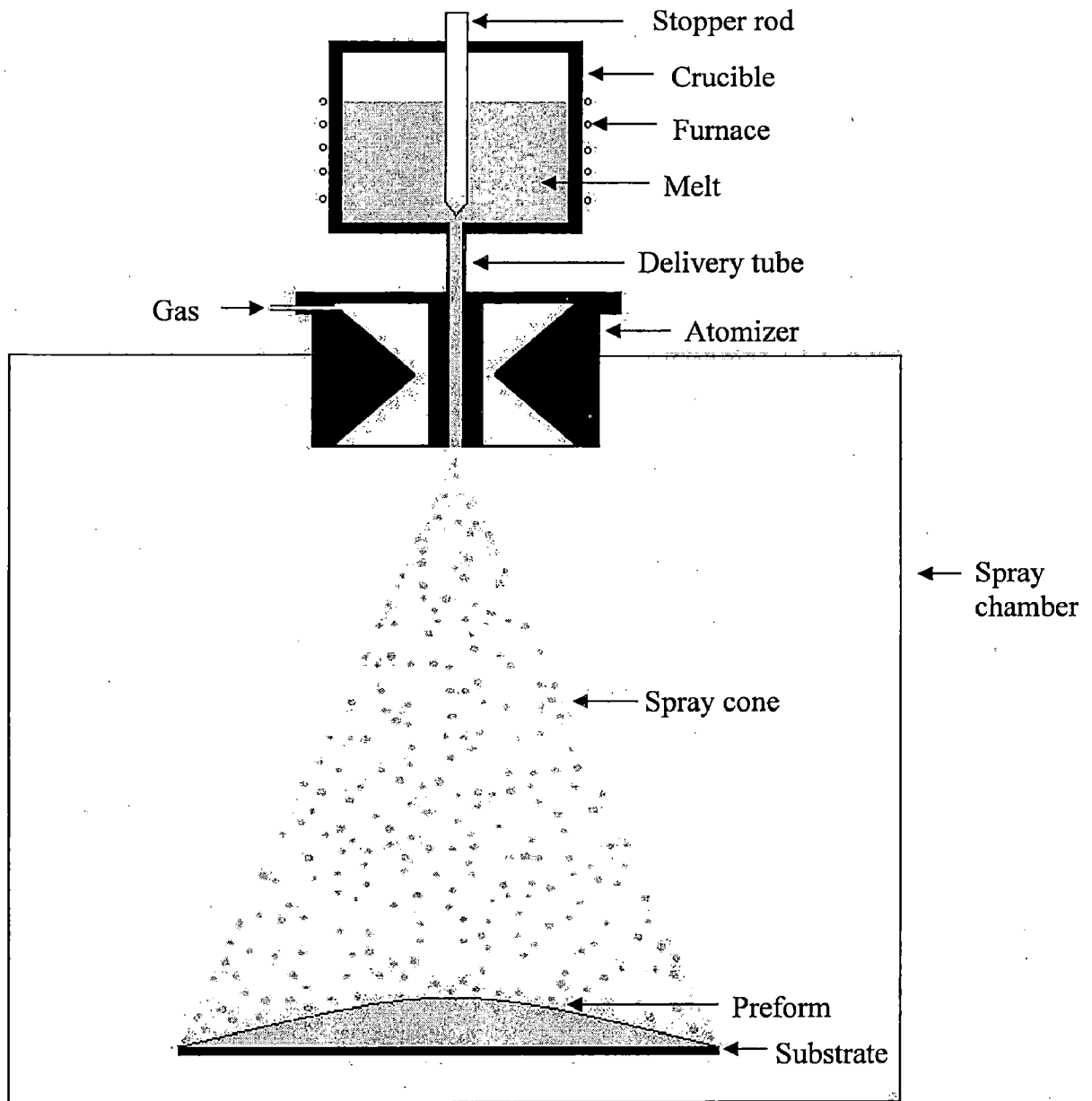


**Fig.4.4** Schematic of spray forming.



**Table 4.1** Values of various variables used in present study

(a) Related to gas (air) dynamics

Conducted study	Plenum pressure kPa	Axial distance mm	Radial distance mm
Gas velocity	500-1500	0-300	0-30
Gas flow rate	500-1500	Not applicable	Not applicable

(b) Related to spray forming/deposition

Conducted study	Alloy compositions (wt%)	Melt temp. (°C)	Substrate		
			Distance from atomizer (mm)	Angle (deg)	Offset distance (mm)
Atomized particles characteristics	Al-6Si-10Pb	820	Not applicable	Not applicable	Not applicable
	Al-6Si-20Pb	-do-			
<b>Spray deposit</b>					
shape	Al-6Si-15Pb	820	400,450,500	0,15,30	0,40
porosity	Al-6Si-(0-25)Pb	-do-	450	30	40
EDAX	Al-6Si-20Pb	-do-	-do-	-do-	-do-
XRD	Al-6Si-(10-25)Pb	-do-	-do-	-do-	-do-
microstructure	Al-6Si-(0-25)Pb	-do-	-do-	-do-	-do-
Hardness	Al-6Si-(0-25)Pb	-do-	-do-	-do-	-do-
	Al-12Si-15Pb	780	-do-	-do-	-do-
Strength	Al-6Si-(0-25)Pb	820	-do-	-do-	-do-
	Al-12Si-15Pb	780	-do-	-do-	-do-
wear rate	Al-6Si-(0-25)Pb	820	-do-	-do-	-do-
	Al-12Si-15Pb	780	-do-	-do-	-do-

- a. Weight of alloy taken for each run = 800 gm
- b. Melt delivery tube diameter = 5 mm
- c. Substrate thickness = 8 mm
- d. Substrate diameter = 200 mm
- e. Substrate rotational speed = 240 rpm
- f. Nitrogen gas plenum pressure = 1000 kPa

### 4.3 SPRAY DEPOSIT CHARACTERIZATION

Preform (spray deposit) was characterized by shape, porosity, microstructure, EDAX analysis, XRD analysis, hardness, tensile strength, ultimate tensile strength, percentage elongation and tribological properties like wear rate and coefficient of friction. Atomized overspray particles were also characterized by microstructure and surface topography.

#### 4.3.1 Shape

Thickness uniformity of the circular deposit (disc) on a substrate was considered as a measure of the shape of spray deposit. For this purpose spray deposited discs of diameter 200 mm on a copper substrate were produced under different process parameters (**table 4.1**) and then their thickness uniformity was observed.

#### 4.3.2 Porosity

Samples were cut from centre of spray deposit having 10, 15, 20 and 25% Pb and prepared by using standard metallographic technique. These samples were examined for surface porosity by image analysis using the optical microscope. 'Olympus model PM-3-311U' in conjunction with a computer having image analysis software from 'Dewinter material plus'.

Surface porosity variation with distance from centre to periphery of the spray deposit was examined by scanning electron microscope (SEM) JEOL JXA 840A.

To measure total porosity at different locations of the deposit, samples were cut from different locations as shown in **fig.4.5**. The total porosity was calculated [48,79] by Archimedes principle and followed the ASTM B 328-96 practice.

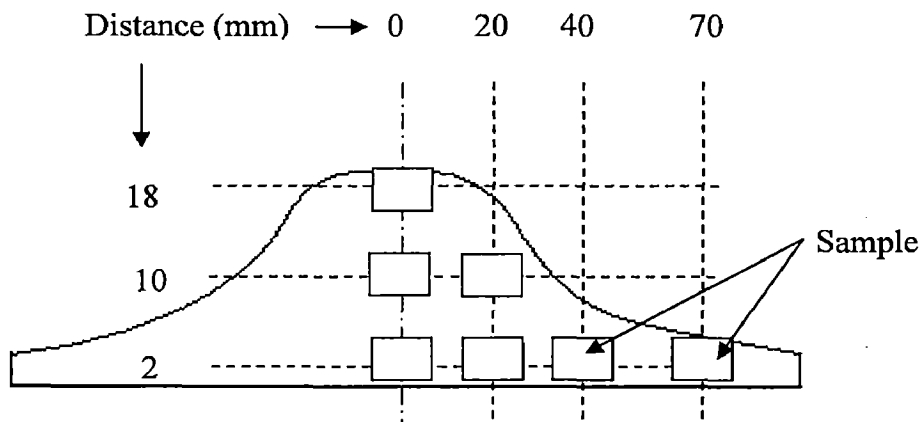


**Fig.4.5** Locations of samples cut from spray deposit for porosity measurements.

### 4.3.3 Microstructure

Samples from the central and peripheral regions of the preform (as shown in **fig.4.6**) were cut down for its microstructural study. These samples were polished using standard metallographic technique of polishing with an emery paper of 1/0, 2/0, 3/0 and 4/0 specification and then followed by wheel cloth polishing using an emulsion of alumina powder particles suspended in water. Afterwards these samples were polished by kerosene oil and brasso. Then samples were etched with Keller's reagent and examined with Letiz optical microscope (OM) and JEOL JXA840A scanning electron microscope (SEM). Scanning electron microscope was operated at an accelerating voltage of 20-25 KV.

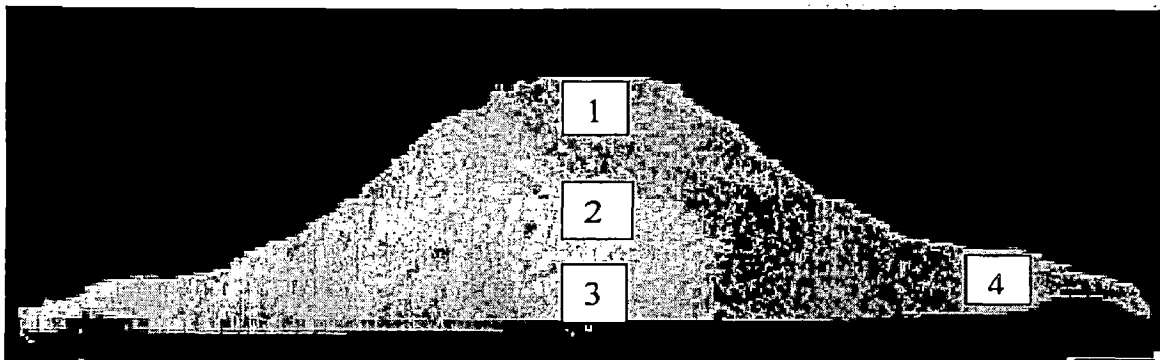


**Fig 4.6.** Sample locations for microstructural study of the preform.

### 4.3.4 EDAX analysis

Phases present in spray formed Al-6Si-20Pb alloy preform were examined by EDAX analysis technique.

### 4.3.5 XRD analysis

XRD analysis of spray deposit for different composition of Pb viz. 10, 15, 20 and 25% in Al-6Si alloy was carried out by Philips X-Ray diffractometer, using Cu target and Ni filter. Diffraction angle ( $2\theta$ ) was varied from 20 to  $120^\circ$  in step of 0.05 deg. The Goniometer speed was  $2^\circ/\text{min}$ .

### 4.3.6 Hardness

Samples for hardness investigation were cut from central and peripheral regions of preform of different lead contents i.e. 0, 10, 15, 20 and 25% as shown in **fig.4.7**. Before commencement of test, samples were ground and polished using standard metallographic technique. A Brinell-cum- Vicker's hardness tester of model HPO 250 was used to measure the Vicker hardness at 5 Kg load. Indentations were taken at different points of central and peripheral regions of each sample as shown in **fig.4.8**.

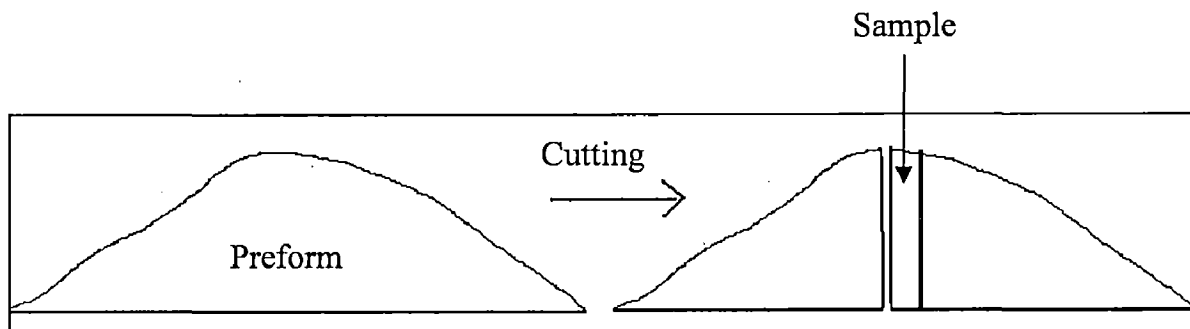


**Fig.4.7** Cutting of sample in strip form from preform for hardness study.

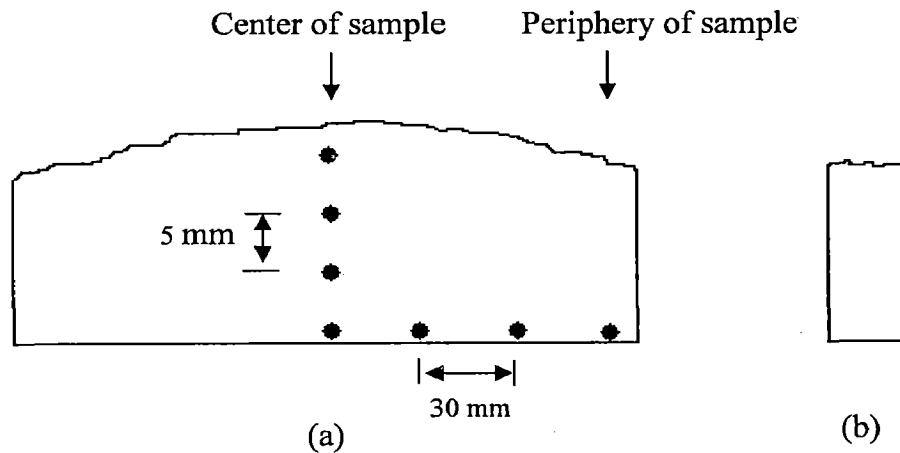
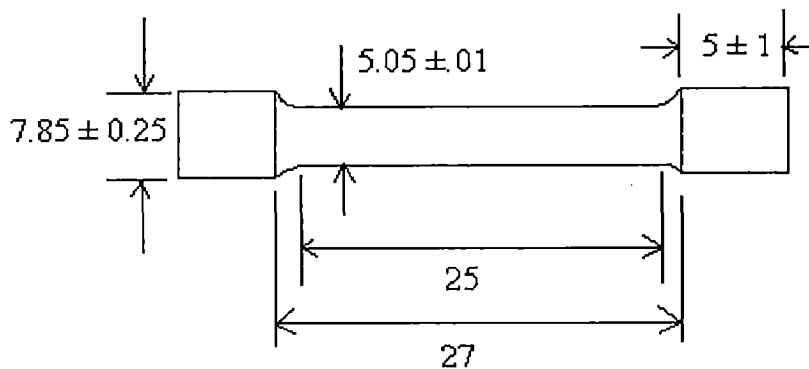


**Fig.4.8** (a) Front and (b) Side view of sample cut from the preform for hardness study.

### 4.3.7 Tensile testing

A 5 tons universal tensile testing machine, model TTC- MC at constant head speed of  $5 \times 10^{-4}$  m/min yielding a conventional strain rate of  $3 \times 10^{-4}$  /sec. was used for tensile testing. Samples of gauge length of 25 mm and diameter 5 mm as shown in **fig.4.9** were taken from the preform. These samples were taken from different distances from centre to periphery of the preform. Preforms of different lead compositions and, 6 and 12% Si were used.



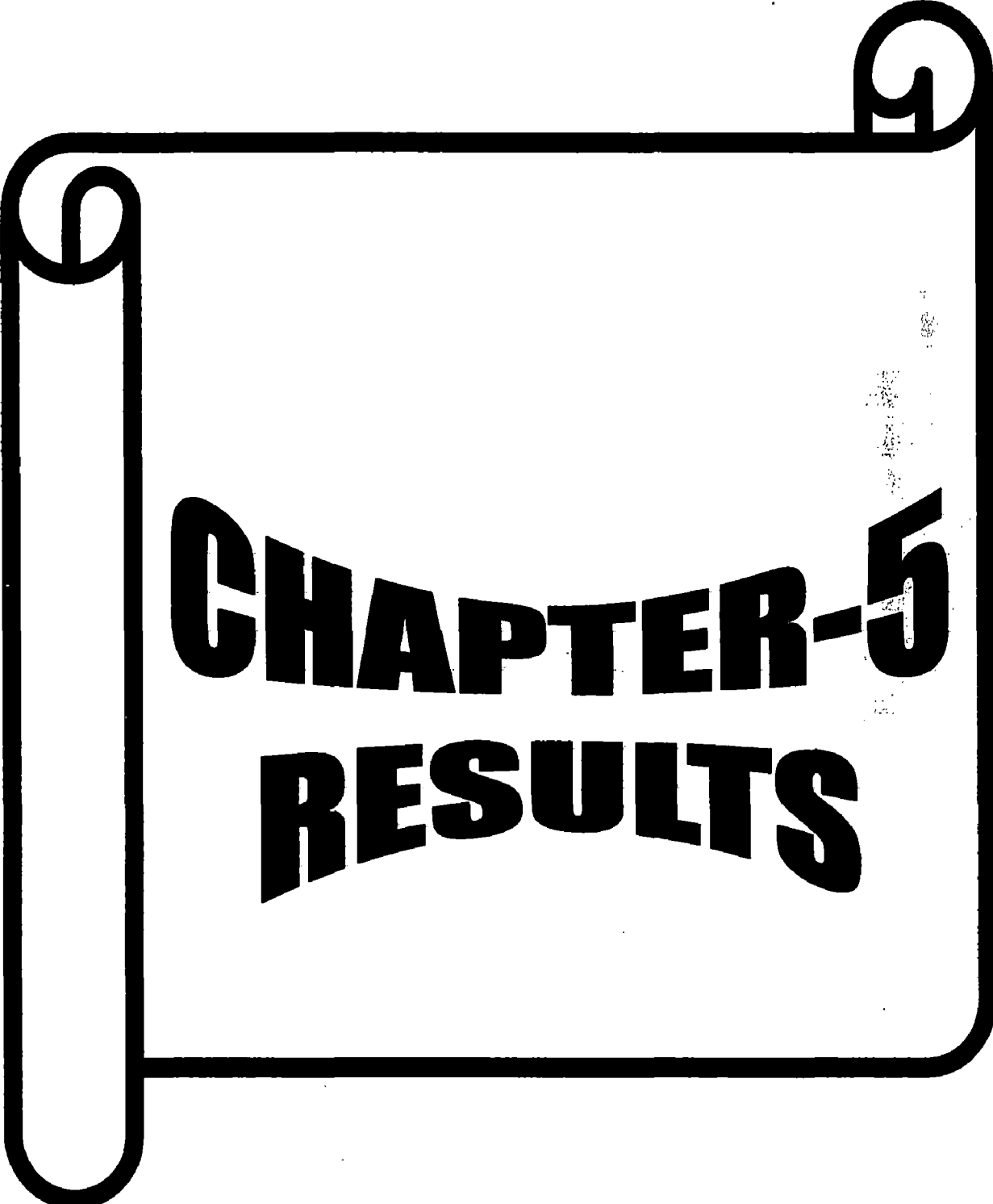
All dimensions are in mm

**Fig.4.9** Dimensions of the specimens used for tensile testing.

### 4.3.8 Wear testing

The spray formed preform with different lead contents were machined into cylindrical pins of dimensions 8 mm diameter x 30 mm length. Specimens were thoroughly degreased by acetone and dried before the commencement of each wear test.

Friction and wear testing of spray formed alloys were investigated using a pin on disc type wear testing machine. It consisted of a hardened EN-24 steel disc (surface roughness = 0.4-0.5  $\mu\text{m}$ ) of diameter 12 cm with Rockwell hardness of 57 HRC and a specimen holder. Rotation speed of the disk was kept constant at 2 m/s throughout the investigation. Wear test specimen was mounted in a specimen holder. The load on the specimen was applied by placing a load on the opposite side of a fulcrum of the lever attached to the specimen holder. The samples were run for a period of 25 minutes before calculating their weight loss which was used to find the resultant wear volume. The radius of rotation was fixed at 36.5 mm. Sliding distance for one run comes out to be around 3000 m for this radius. The standard wear test procedure was followed for evaluating the wear rate for different load ranging from 10 to 80 N. The disc surface was cleaned with acetone before each experimental run. All the tests were carried out in dry sliding conditions and at room temperature. Pin specimens were weighed both before and after testing on a single pan electrical balance that gave reading to 0.01 mg. The worn surfaces of the wear pins after the test were examined by using JEOL JXA840A scanning electron microscope (SEM). Also, the debris generated during wear experiments was examined by XRD.



**CHAPTER-5**  
**RESULTS**

### 5.1 GAS DYNAMICS OF ATOMIZER

Every gas nozzle or atomizer has its own gas dynamics characteristics and these are gas velocity distribution in the gas field generated by the atomizer and the gas flow rate. Both the characteristics will affect the spray forming process and hence these needs to be determined thoroughly before spray forming study. There is no universal empirical or theoretical formula available in open literature to determine these two parameters. Therefore, both parameters are determined experimentally for the atomizer used in the present study for the spray forming of Al-Si-Pb alloys.

#### 5.1.1 Gas velocities

Gas velocity in the gas field generated by the atomizer was measured in both the directions i.e. axial and radial. These velocities were not measured up to an axial distance of 12 mm from the atomizer/ nozzle exit because there was aspiration or suction.

##### (a) Axial velocity

Fig.5.1 shows the variation of gas velocity as a function of axial distance for zero radial distance (i.e.  $r = 0$ ) at different plenum pressures viz. 5, 7, 10 and 15 bar. It can be seen that the gas velocity shoots up to some maximum value within a distance of 25 mm at all plenum pressures. Beyond 25 mm axial distance the gas velocity decreases linearly but with a lower rate as compared to that of its increasing rate. For example, the gas velocity shoots up with distance at the rate of 16 m/s but decreases with an average rate of 0.6 m/s per mm of axial distance at a plenum pressure of 10 bar.

A similar trend of gas velocity variation was observed for a radial distance of 10 mm as shown in fig.5.2. Although, gas velocities are lower to some extent than that at the radial distance of 0 mm.



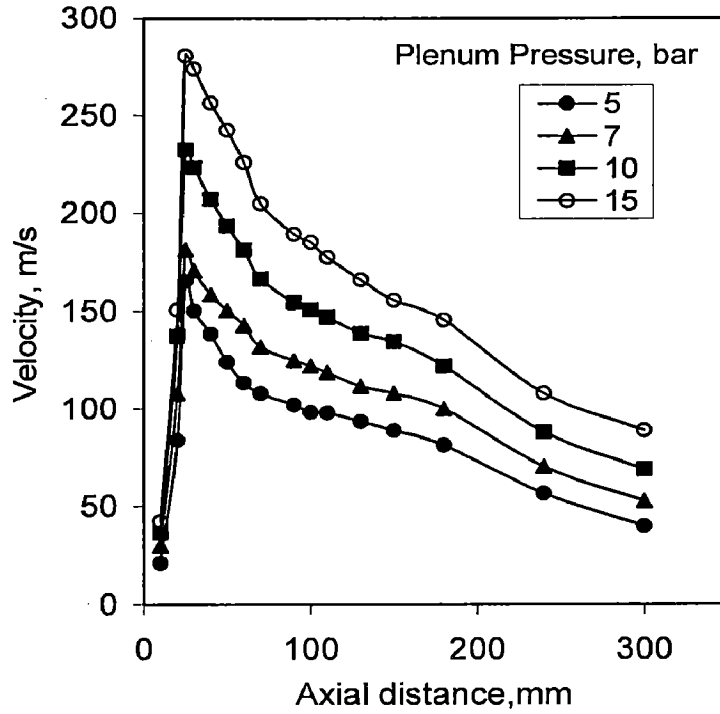


Fig. 5.1 Variation of gas velocity with axial distance, for zero radial distance at different plenum pressures.

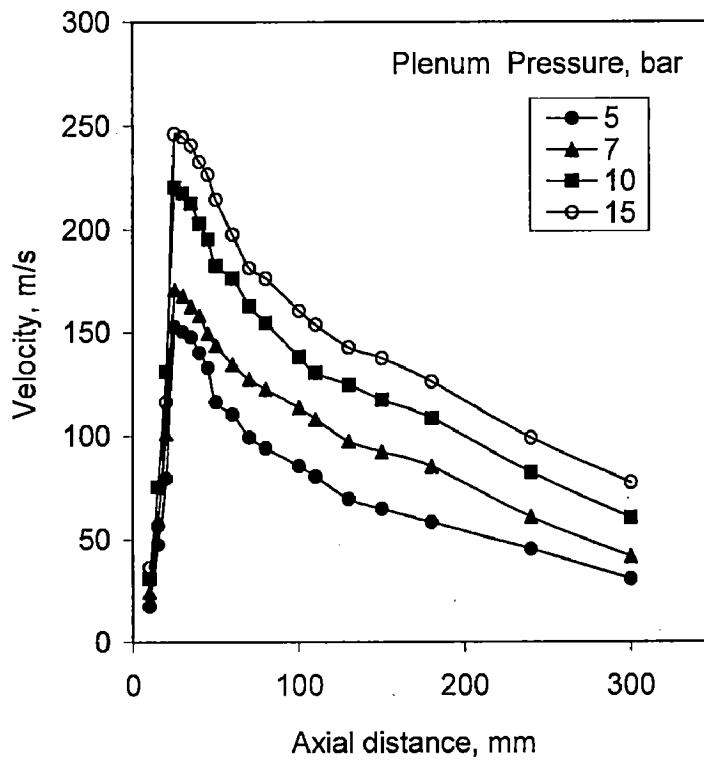
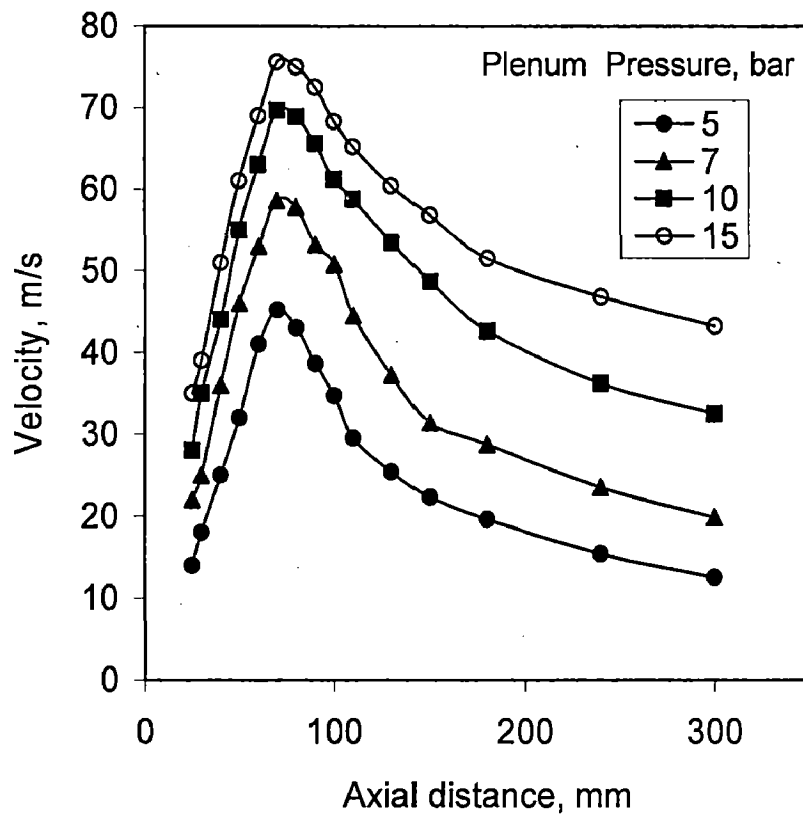


Fig. 5.2 Gas velocity variation with axial distance for radial distance of 10 mm at different plenum pressures.

At a radial distance of 20 mm, the pattern of gas velocity variation is different from that of 0 and 10 mm radial distances as shown in **fig. 5.3**. It can be seen that the maximum velocity occur at a higher axial distance as compared to that of previous two cases i.e. at  $r = 0$  and 10 mm. The maxima in velocity were observed at an axial distance of 70 mm as compared to that of 25 mm and the gas velocity also increases at a lower rate (up to 70 mm distance) with axial distance as compared to that of previous two cases.



**Fig. 5.3** Gas velocity variation with axial distance for 20 mm radial distance at different plenum pressures.

**Fig.5.4** shows the variation of gas velocity with axial distance for radial distance of 30 mm at different plenum pressures viz. 5, 7, 10 and 15 bar. In this case the maximum velocity was observed at an axial distance of 100 mm which is higher than that of at the radial distance of 20 mm. The gas velocity initially increases and then decreases at a lower rate as compared to that of at radial distances of 0, 10 and 20 mm.

For example, the velocity increases and then decreases with axial distance at an average rate of 0.4 and 0.1 m/s per mm distance, respectively.

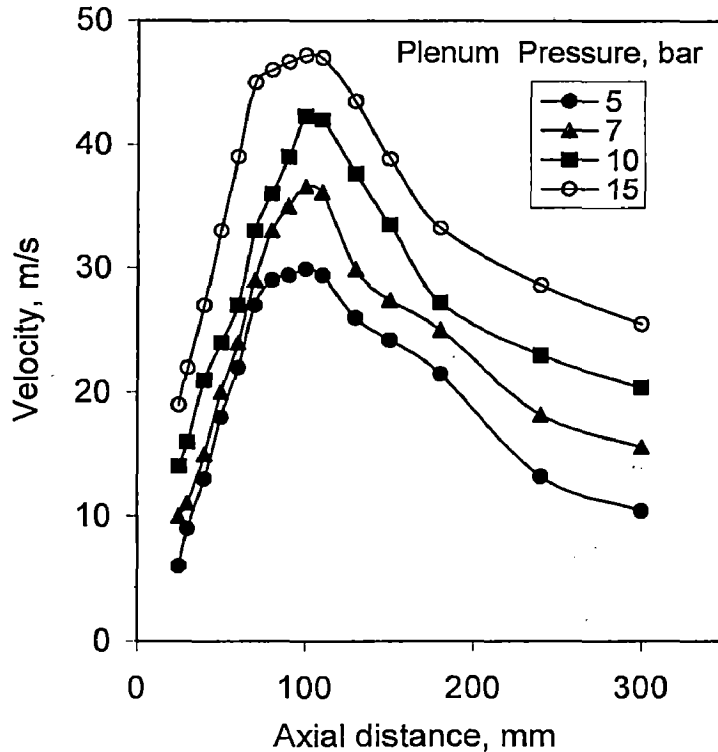


**Fig. 5.4** Gas velocity variation with axial distance for 30 mm radial distance at different plenum pressures.

### (b) Radial velocity

Gas velocity variation as a function of radial distance at different plenum pressures (5, 7, 10 and 15 bar) for axial distance of 25 mm is shown in **fig.5.5**. It can be seen that the velocity decay is negligible up to a radial distance of 10 mm and beyond this distance the velocity decreases very rapidly at all plenum pressures. For example, at a plenum pressure of 10 bar, the gas velocity is 230 m/s up to 10 mm radial distance and then it decreases to 25 m/s at 20 mm radial distance.

**Fig.5.6** shows the variation of gas velocity with radial distance at different plenum pressures for axial distance of 50 mm. The gas velocity decreases very slowly up to 10 mm radial distance and beyond this distance the velocity decreases at a faster rate. For example, the average decay rate of gas velocity up to 10 mm radial distance is

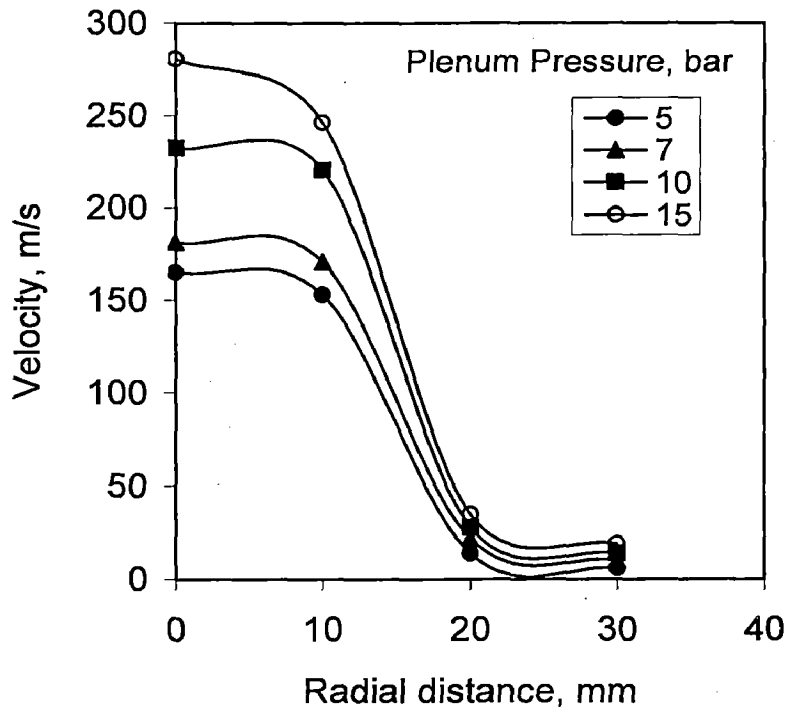


Fig. 5.5 Variation in gas velocity with radial distance for 25 mm axial distance at different plenum pressures.

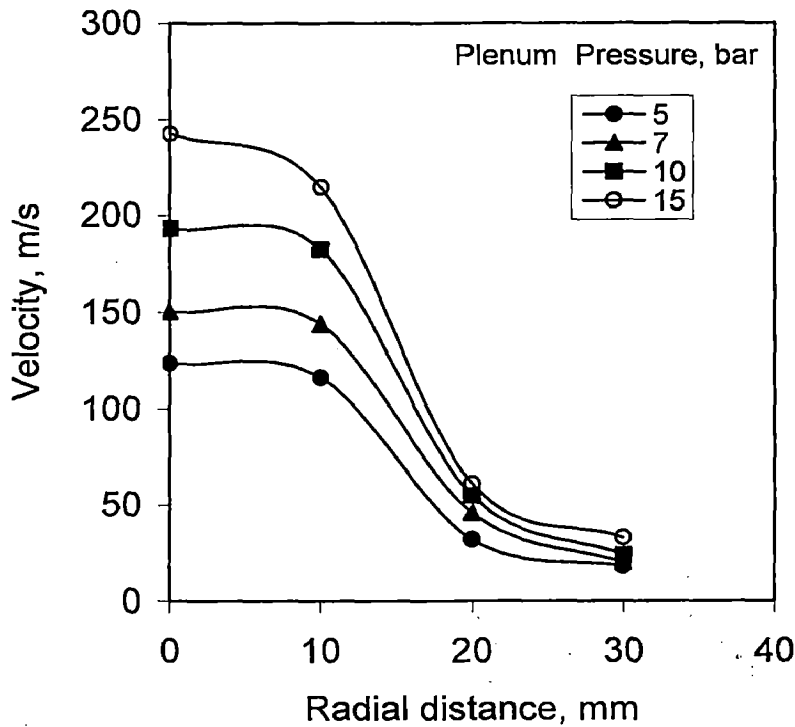
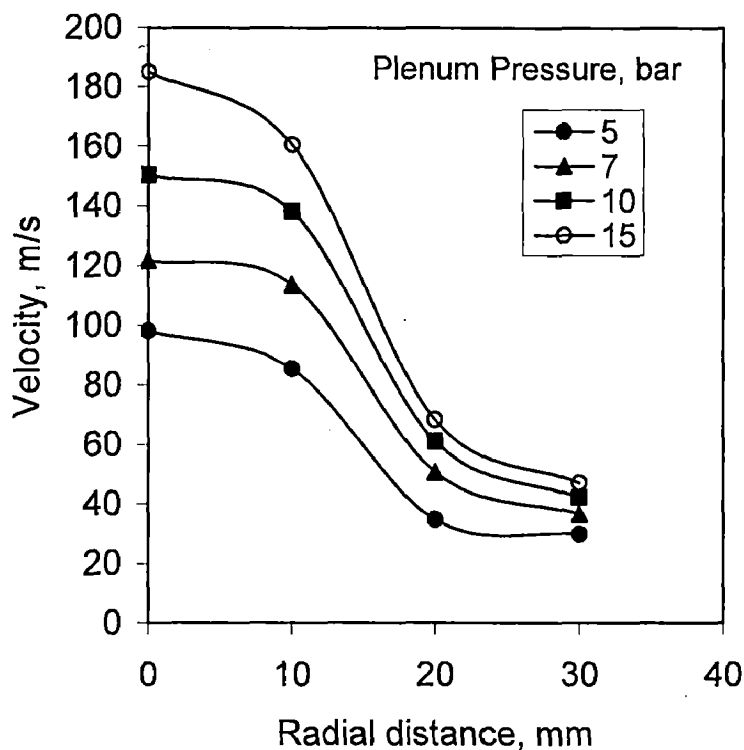


Fig. 5.6 Variation in gas velocity with radial distance for 50 mm axial distance at different plenum pressures.

0.5 m/s per unit increase in distance and beyond this radial distance the value of decay rate is 11.0 m/s. A similar type of gas velocity variation is observed at an axial distance of 100 mm as shown in **fig.5.7**. In this case, the gas velocity decreases at a higher rate up to 10 mm radial distance as compared to that of the previous case i.e. at the axial distance of 50 mm.



**Fig. 5.7** Variation in gas velocity with radial distance for 100 mm axial distance at different plenum pressures.

Variation of gas velocity with radial distance at different plenum pressures for axial distance of 300 mm is shown in **fig.5.8**. The gas velocity decreases at a higher rate up to 10 mm radial distance as compared to that of 25 and 50 mm axial distances. For example, the gas velocity decreases at an average rate of 1.0 m/s per unit increase in distance up to 10 mm radial distance and beyond this distance it decreases at the rate of 2.0 m/s per unit increase in the radial distance.

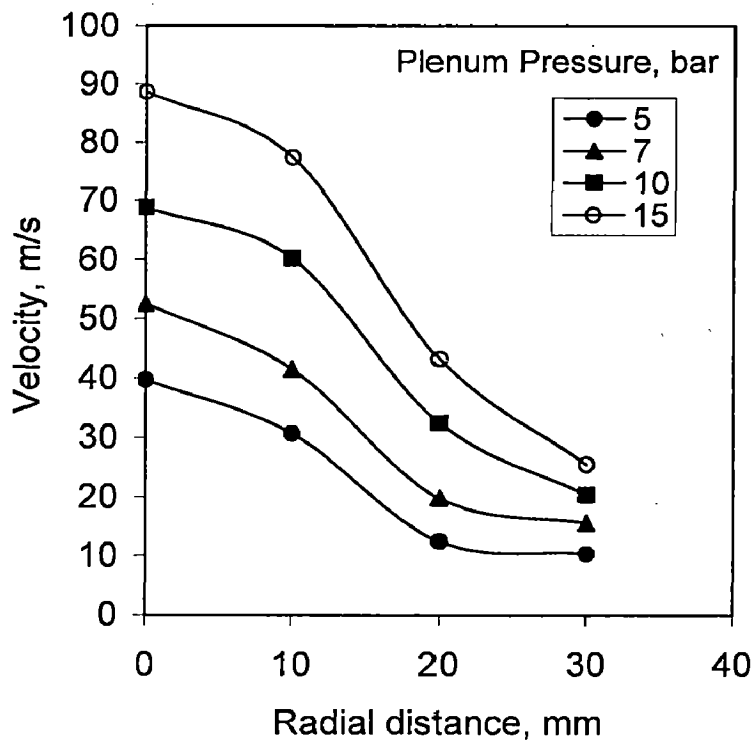
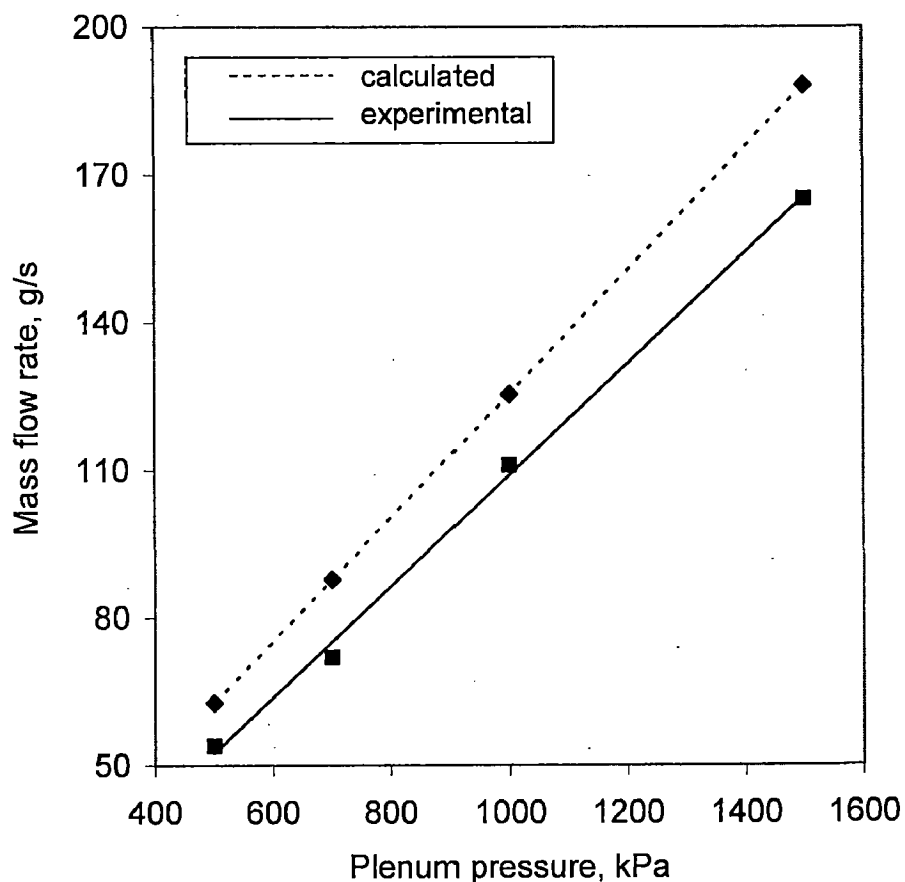


Fig. 5.8 Variation in gas velocity with radial distance for 300 mm axial distance at different plenum pressures.

### 5.1.2 Gas flow rate

Experimental and calculated [80] gas mass flow rates as a function of plenum pressure are shown in **fig.5.9**. Both the flow rates increase at a constant rate with the increase in plenum pressure. Although, the rate of increase is lower in case of experimental flow rate (11.1 g/s / KPa) as compared to that of calculated one (12.5 g/s / KPa). Also, the experimental flow rate is lower than that of calculated one.



**Fig. 5.9** Experimental and calculated gas mass flow rate as a function of plenum pressure.

## 5.2 SHAPE OF SPRAY DEPOSIT

The side view of the deposit produced at three different distances from the atomizer and three different inclination angles of the substrate are shown in **fig.5.10**. The substrate was also offset by 40 mm from the atomizer axis in case of 15 and 30° inclination angles. This figure shows the shape of deposit for the different combinations and values of parameters reported in **table 5.1**.

**Table 5.1** Values of different experimental parameters in **fig.5.10**

Figure number	Substrate distances(h) mm	Offset distance(s) mm	Inclination angle( $\theta$ ) deg.
(a)	400	0	0
(b)	450	0	0
(c)	500	0	0
(d)	450	40	0
(e)	450	40	15
(f)	450	40	30

It can be seen that the thickness uniformity of the deposit produced at an angle of 30° with an offset distance of 40 mm (**fig.5.10 (f)**) is higher than that of at 15° (**fig.5.10 (e)**) which is higher than that of at 0° (**fig.5.10 (d)**). In other words, the thickness uniformity of the deposit increases with the increase in inclination angle with offset distance of the substrate from atomizer axis. However, the loss of deposited droplets also increases with the increase in inclination angle for the same size of the substrate which is obvious from the geometry with consideration of the conical shape of the spray cone of droplets. The thickness uniformity also increases with the increase in deposition distance from atomizer as observed from **figs.5.10 (a), (b) and (c)**. However, again the loss of deposited particles also increases with the increase in deposition distance for the same size of preform which is also obvious from the geometry.



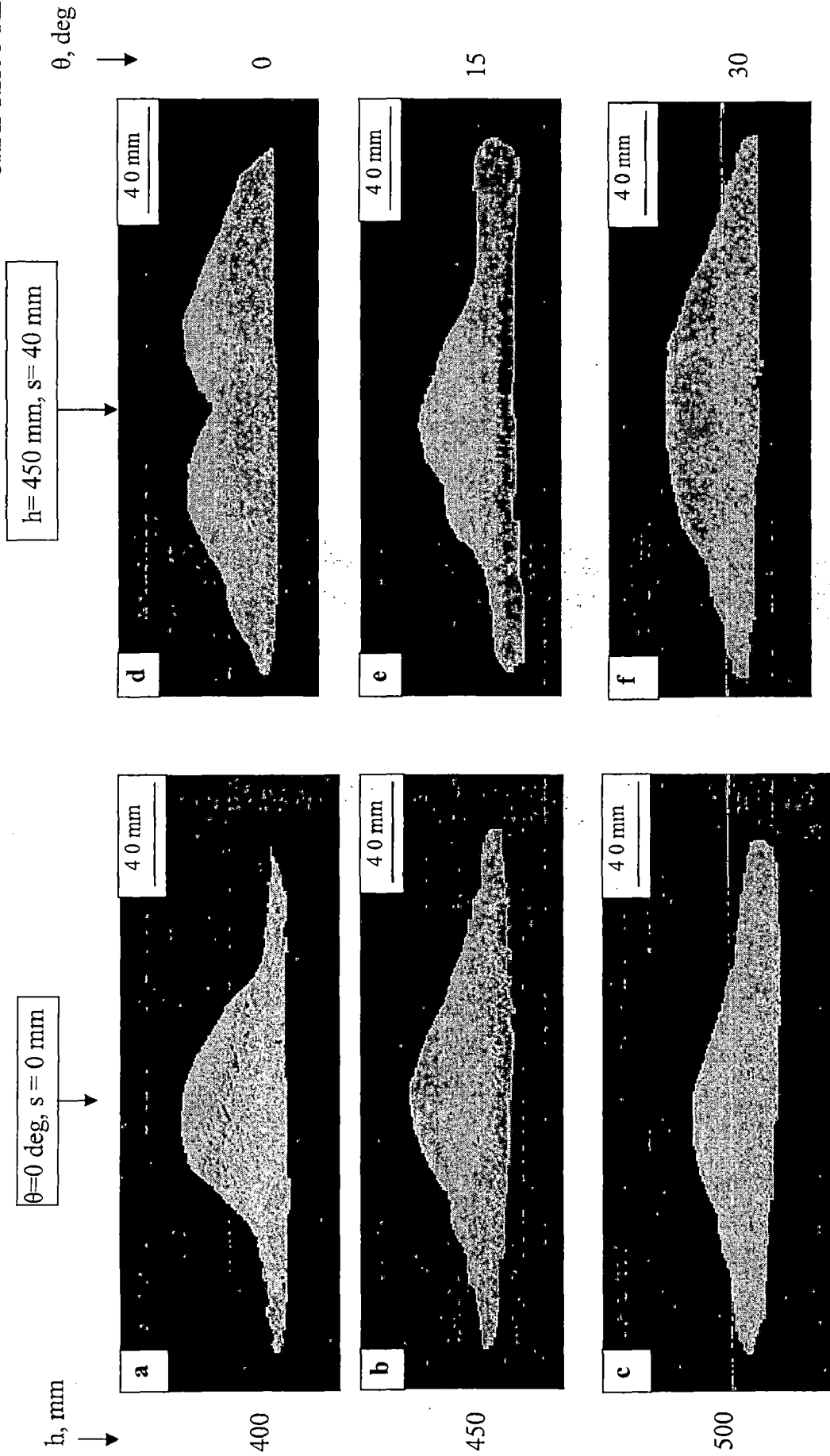


Fig. 5.10 Shape of spray deposit produced at different substrate distances ( $h$ ), offset distances ( $s$ ) and inclination angles ( $\theta$ ): (a)  $h = 400$ ,  $\theta = 0$ ,  $s = 0$ ; (b)  $h = 450$ ,  $\theta = 0$ ,  $s = 0$ ; (c)  $h = 500$ ,  $\theta = 0$ ,  $s = 0$ ; (d)  $h = 450$ ,  $\theta = 0$ ,  $s = 40$ ; (e)  $h = 450$ ,  $\theta = 15$ ,  $s = 40$  and (f)  $h = 450$  mm,  $\theta = 30$  deg,  $s = 40$  mm.

### 5.3 POROSITY IN SPRAY DEPOSIT

Theoretical densities calculated for the alloys used in present study are given in **table 5.2** and measured densities are reported with their location in the spray deposit in **fig.5.11**.

**Table 5.2** Theoretical density of Al-6Si-xPb alloys

x =	0	10	15	20	25
Density (g/cc)	2.62	2.89	3.02	3.15	3.30

It can be seen that there is no change in density in the thickness direction of the deposit. The change in density and hence porosity is observed with the increase in distance from the centre to periphery of the deposit. The total porosity calculated from these densities is shown in **fig.5.12** as a function of distance from centre to periphery of the deposit for various compositions of the lead. It can be seen that the porosity decreases with the increase in distance from centre to periphery for all compositions of the lead. The porosity is higher for higher lead content. The decay rate in porosity with the increase in distance increases with the increase in lead content. For example, for 0% and 25% Pb the average decrease in porosity is 0.036 and 0.27 per unit of distance, respectively. The decay rate in porosity also decreases towards the periphery of the deposit. For example, it is 0.15 per unit of distance for 25% Pb.

The change in porosity with lead content at four different locations viz 0, 20, 40 and 70 mm from centre of the deposit is shown in **fig.5.13**. It can be seen that the porosity increases more rapidly with the increase in lead content at the centre of the deposit as compared to that of other locations. For example, the average increase in porosity is 0.83 and 0.19 per unit of lead content at the centre and periphery (at 70 mm from centre), respectively. Initially, the rate of increase in porosity is slow with the increase in lead content. For example, it is 0.61 per unit increase in lead content at centre of the deposit.

To observe porosity and its distribution with the distance from centre to periphery of the deposit and with the lead content the recorded micrographs are shown in **figs.5.14** and **5.15**, respectively. **Fig.5.14** shows porosity for 20% Pb at distances 0,

20, 40 and 70 mm from centre to periphery of the deposit and **fig.5.15** shows porosity for 10, 15, 20 and 25% Pb at the centre of the deposit. Micrographs shown in **fig.5.15** are taken by Image analyzer. These micrographs were taken at high magnification 4000X to visualize the porosity. In micrographs (a) and (b) of **fig.5.14** large number of black spots can be seen uniformly distributed throughout the matrix. This type of porosity seems to be low at periphery i.e. 70 mm distance (**fig. 5.14(d)**) from centre of the deposit. The size of pores varies from sub-micron to  $\sim 5\mu\text{m}$ .

The effect of lead content on porosity is shown in **fig.5.15** for various lead contents. Red spots in micrographs represent porosity. It can be seen that the porosity increases with the increase in lead content. Every micrograph is having two types of areas viz. first type area is having large amount of porosity and the second type area is having small amount of porosity. The large and small amount porosity areas belong to the lead and aluminum rich areas, respectively.

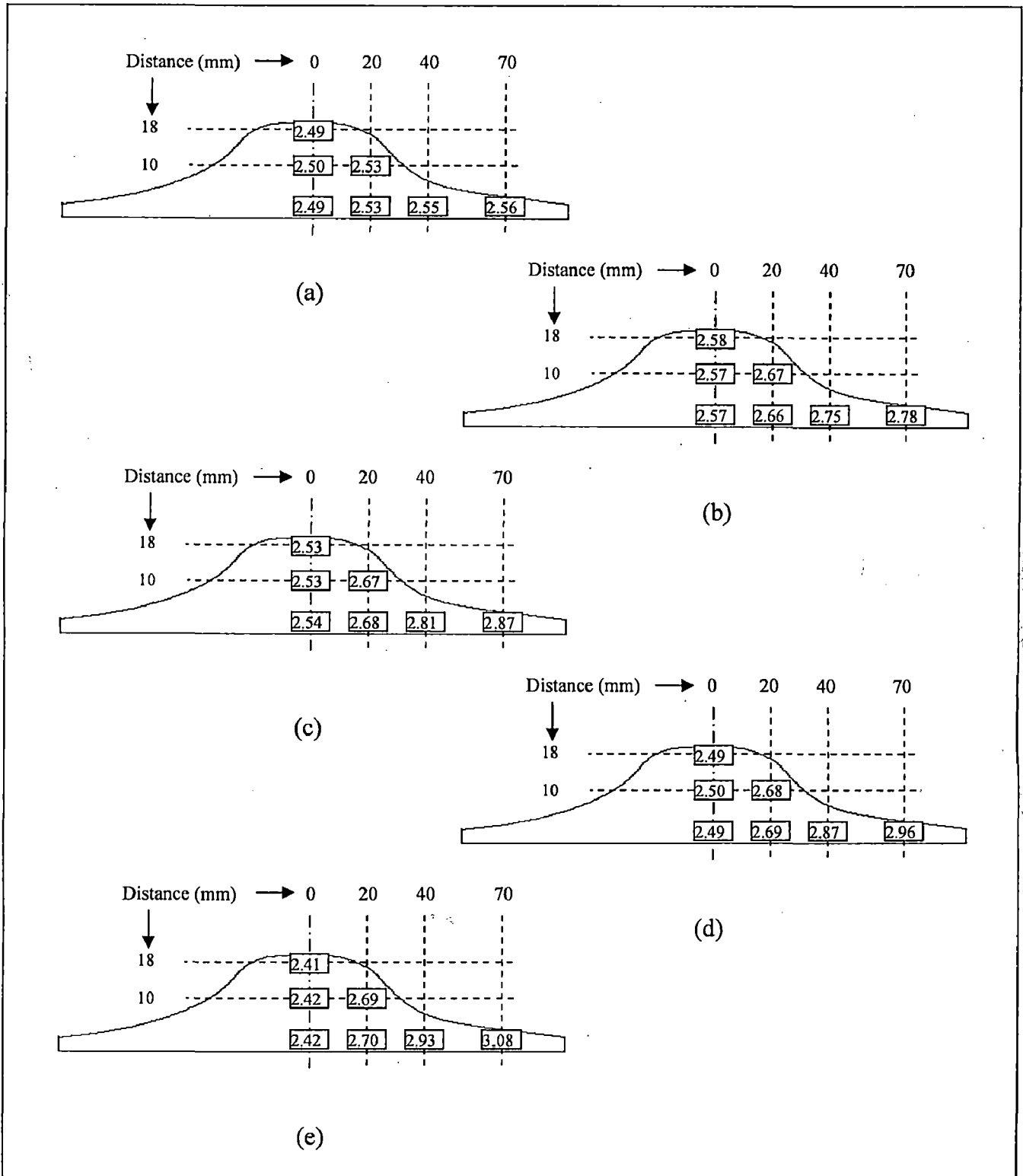


Fig.5.11 Measured densities (gm/cc) with their locations in the spray deposit for different percentage of Pb: (a) 0; (b) 10; (c) 15; (d) 20 and (e) 25%.

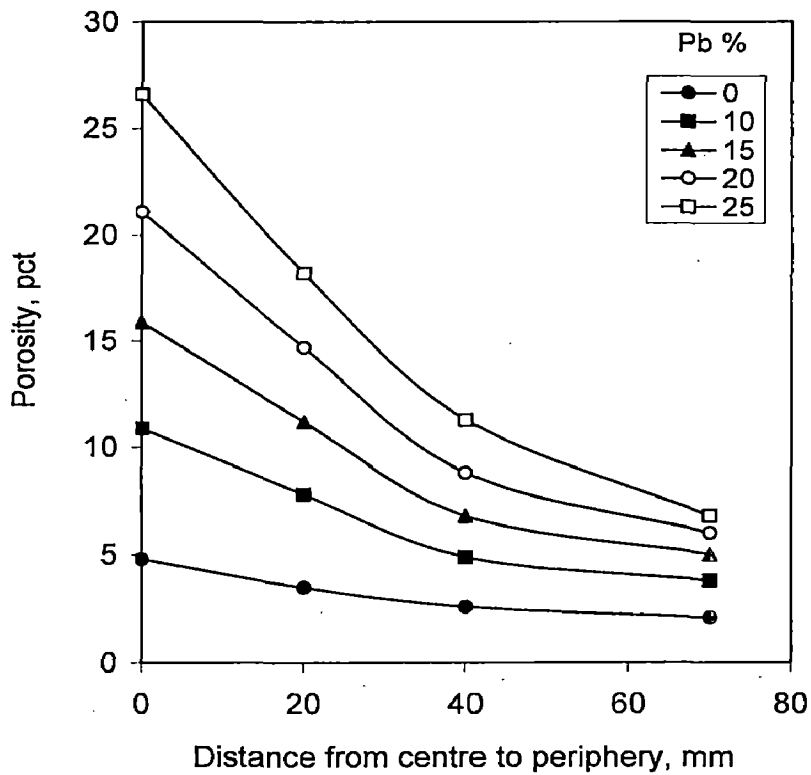


Fig. 5.12 Variation in porosity with distance from centre to periphery of spray deposited preform at different Pb content.

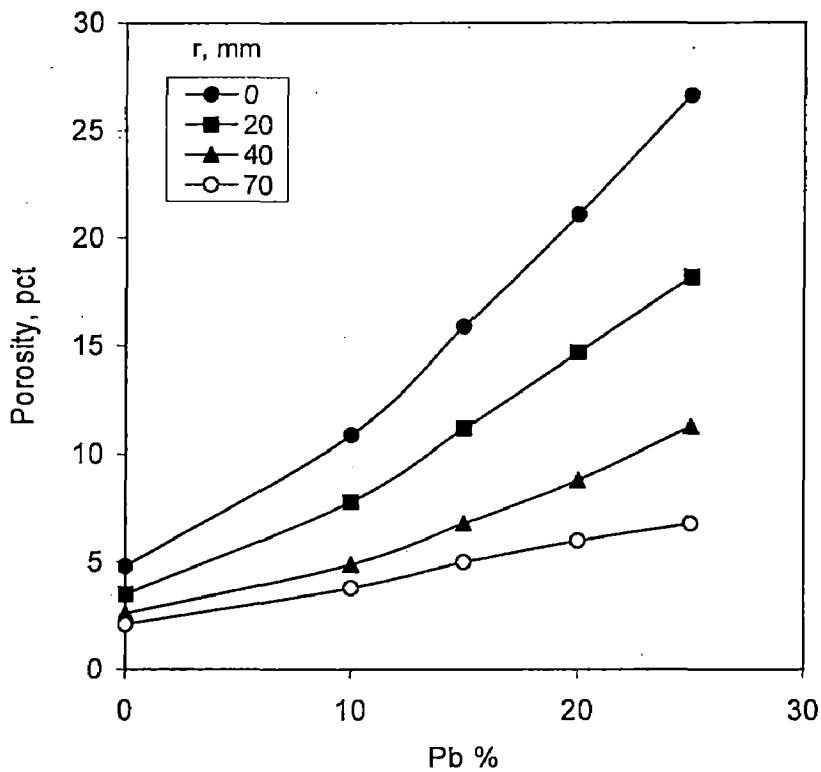
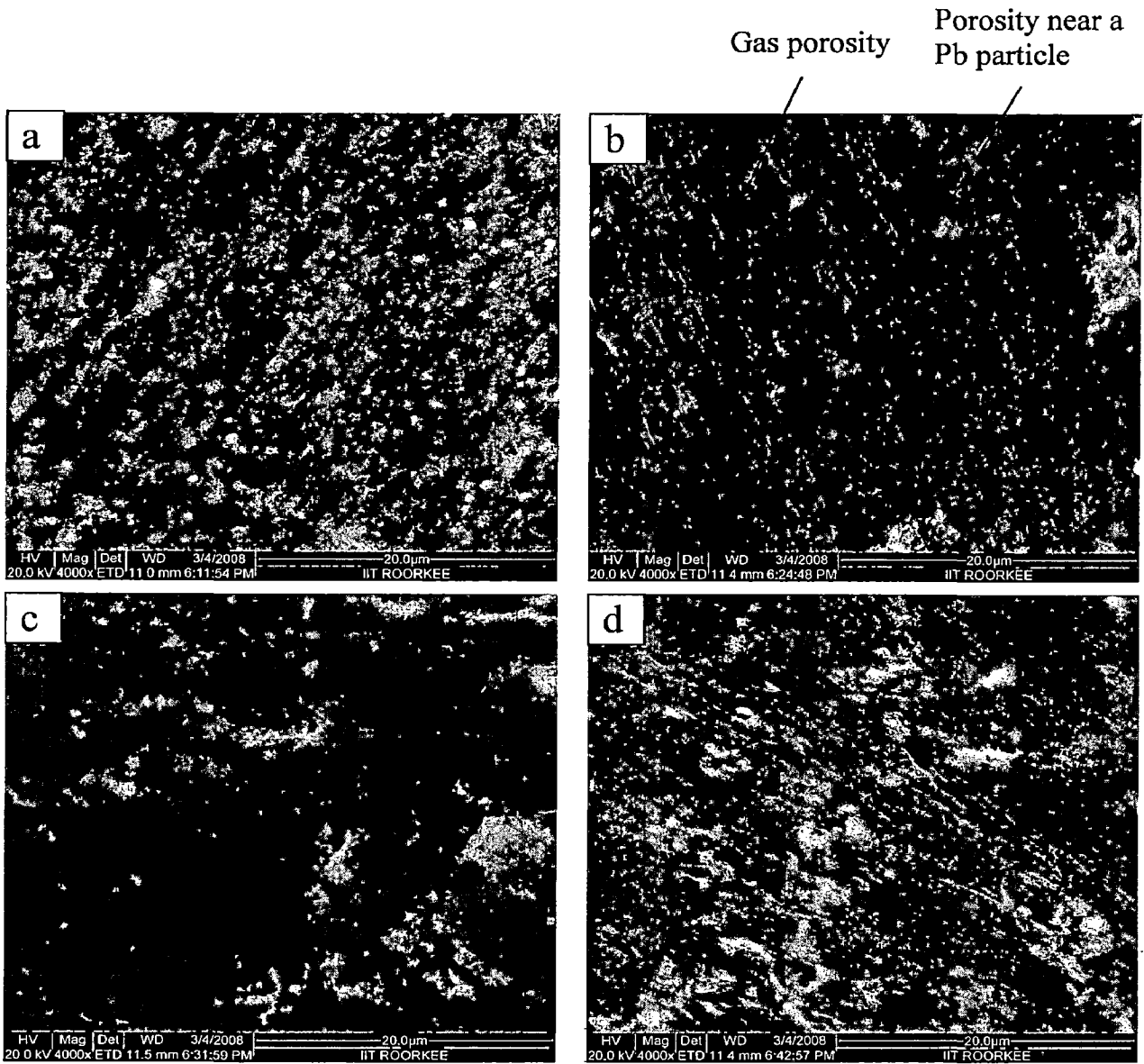
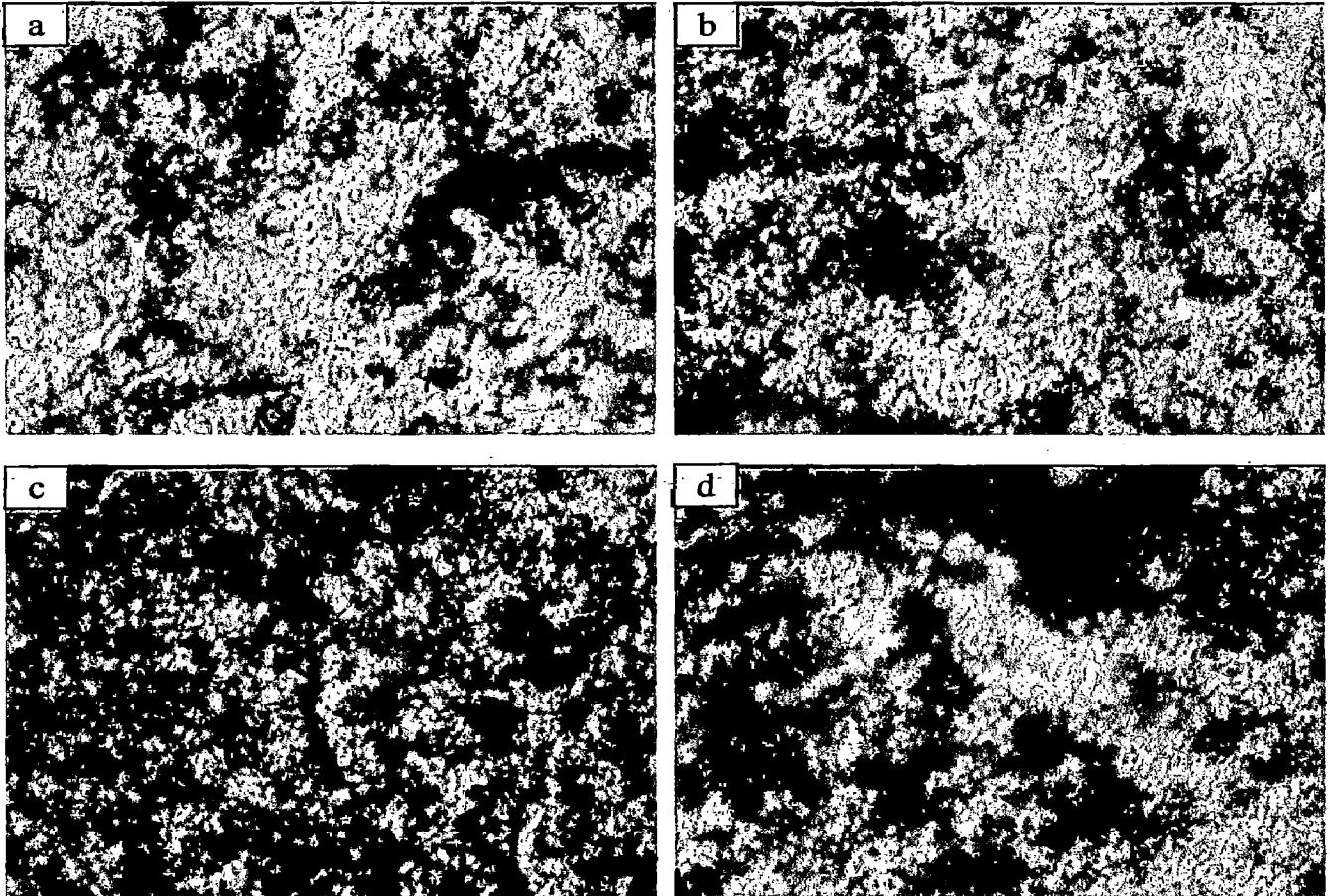


Fig. 5.13 Porosity variation with Pb content at different distances from centre of the deposit.



**Fig. 5.14** Microstructure at 4000X to show porosity variation from centre to periphery of the deposit at distances: (a) 0; (b) 20; (c) 40 and (d) 70 mm for 20% Pb.



**Fig. 5.15** Micrograph showing the porosity distribution with Pb content of (a) 10; (b) 15; (c) 20 and (d) 25% at center of the deposit.

## 5.4 MICROSTRUCTURAL FEATURES

Fig.5.16 shows the EDAX spectrums with micrographs of the analyzed region for Al-6Si-20Pb spray formed alloy. EDAX analysis of black and white regions of the micrograph gives Al, Si and Pb peaks and these two regions are shown in micrographs in the same figure. The EDAX analysis of white (bright) region shows that it is the Pb rich phase and so the black (dark) region should be Al rich phase. The further study was carried out with this knowledge of dark and bright regions.

### 5.4.1 Spray particles

Figs.5.17 and 5.18 show the SEM micrographs of the spray particles for two different compositions viz. 10 and 20% of lead, respectively, at two different magnifications viz. (a) 200x and (b) 500x. Particles size is varying from sub-micron to 100  $\mu\text{m}$ . White and black colour particles are Pb and Al rich, respectively (as revealed by EDAX analysis in fig.5.16). The shape of the particles is rounded and having rough surface. Aluminum rich particles are coarser than lead rich particles and these particles are having about 1-3  $\mu\text{m}$  size lead particles on their surface. Numbers of these lead particles are increasing with the increase in lead percentage from 10 to 20 % as visible in figs.5.17 (b) and 5.18 (b), respectively. Silicon phase in these particles could not be identified. Some particles are showing satellite formation and some are showing cracks at their surface. Aluminum or lead rich liquid phase was observed to be solidified on some particles. Particles also show surface shrinkage and no evidence of porosity as can be seen in fig.5.19.

Microstructures of the cross-section of two different powder particles are shown in fig.5.20. Size of the cross-section of fig.5.20 (a) is smaller than that of fig.5.20 (b). But, it is impossible to say which particle has larger size because it will depend on the depth of cross-section and shape of the particle. Lead particles are observed in interdendritic regions. The secondary dendritic arm spacing is about 2 and 4  $\mu\text{m}$  in fig.5.20 (a) and (b), respectively. Some porosity is also visible in the microstructures.



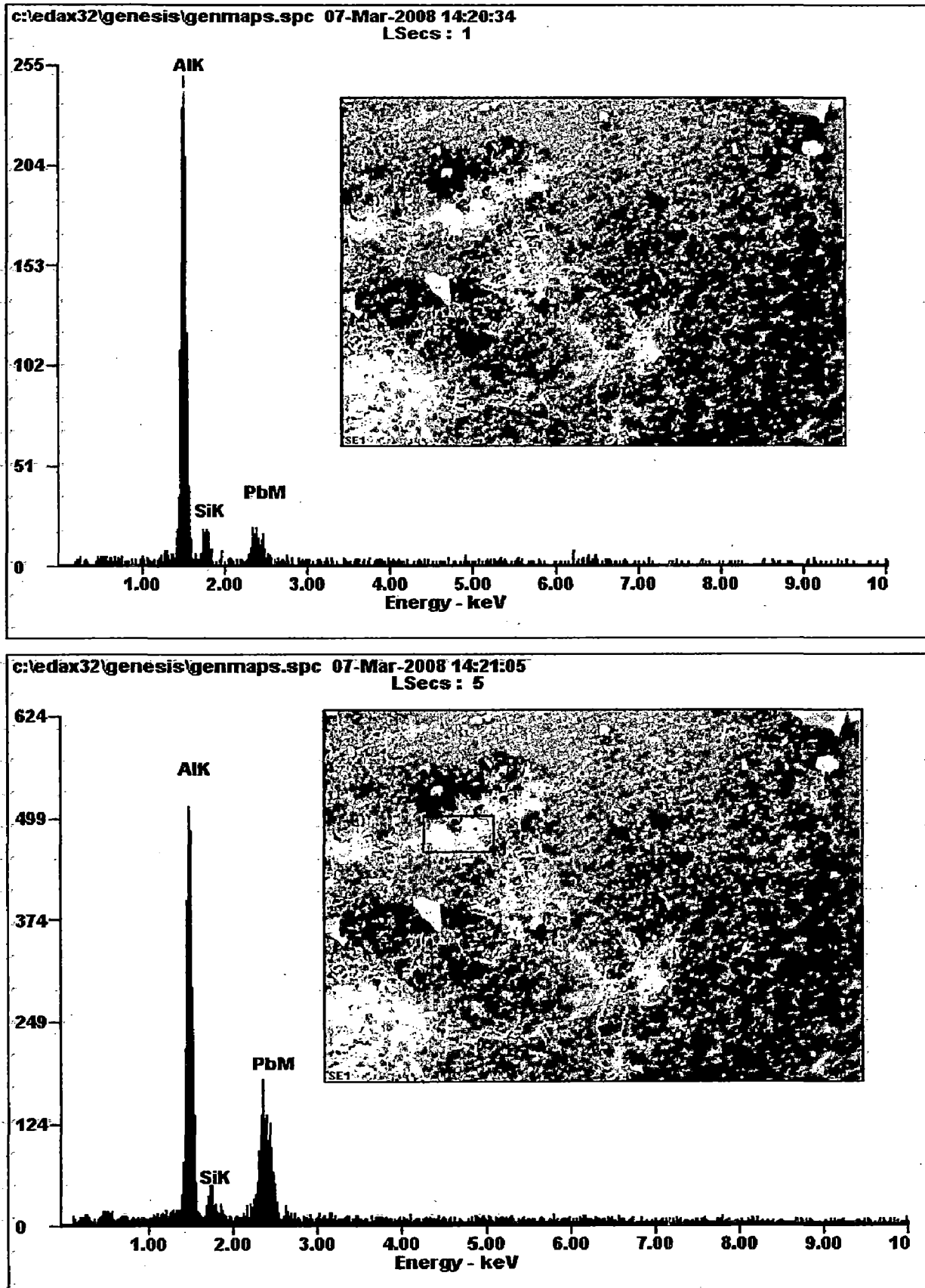


**Fig. 5.16** EDAX spectrum with analyzed (a) whole region; (b) bright region, indicating Pb and Si phases in spray deposited Al-6Si-20Pb alloy.

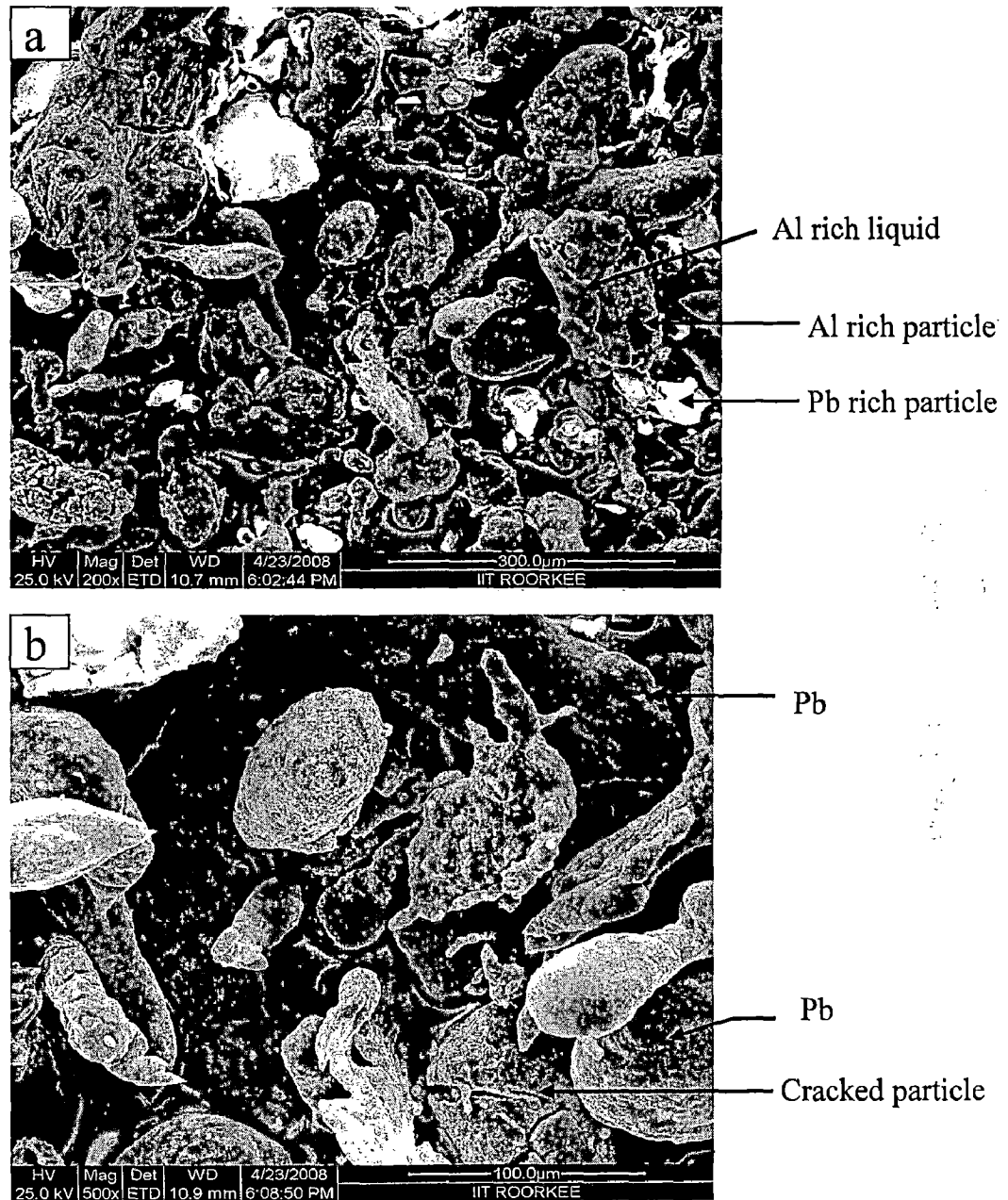


**Fig. 5.17** SEM micrographs showing the size, shape and some other characteristics of Al-6Si-10Pb alloy spray particles at magnification of (a) 200X and (b) 500X

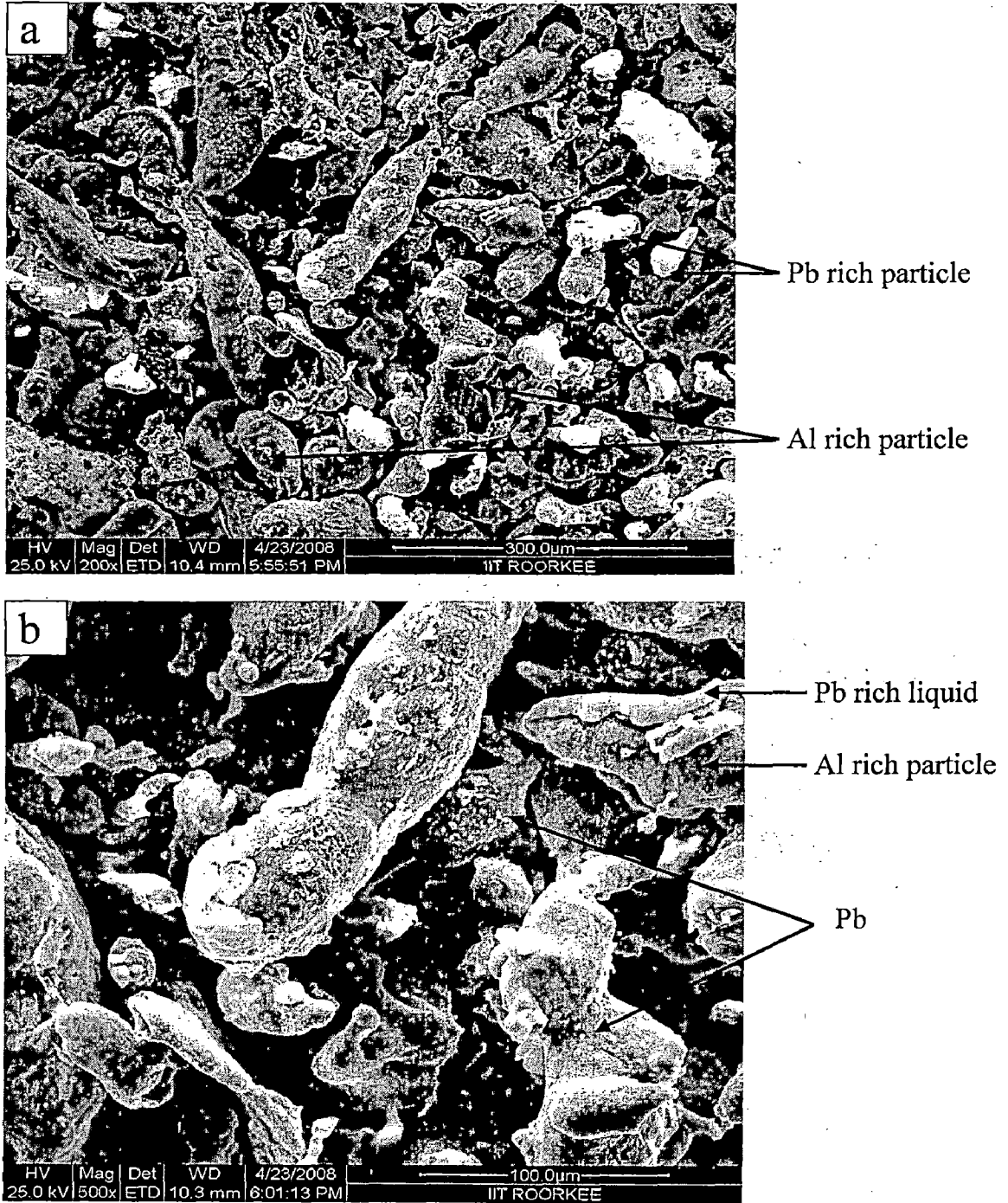


**Fig. 5.18** SEM micrograph showing the size, shape and some other characteristics of Al-6Si-20Pb alloy spray particles at magnification of (a) 200X and (b) 500X.

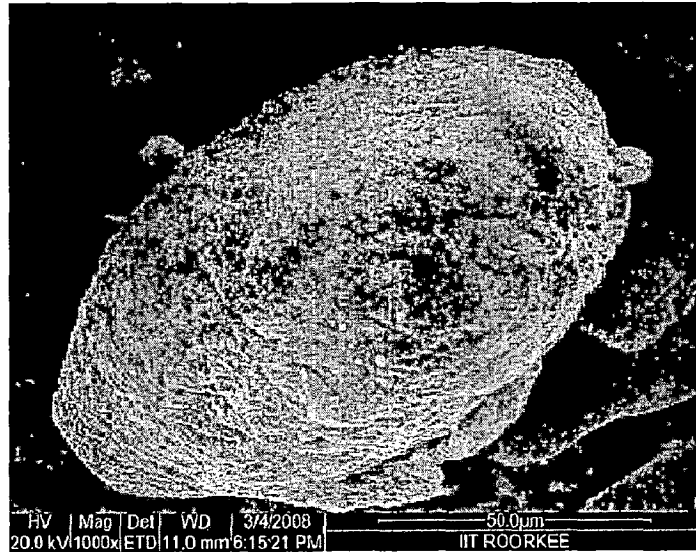


**Fig. 5.19** SEM micrograph showing the surface topography of Pb rich particle

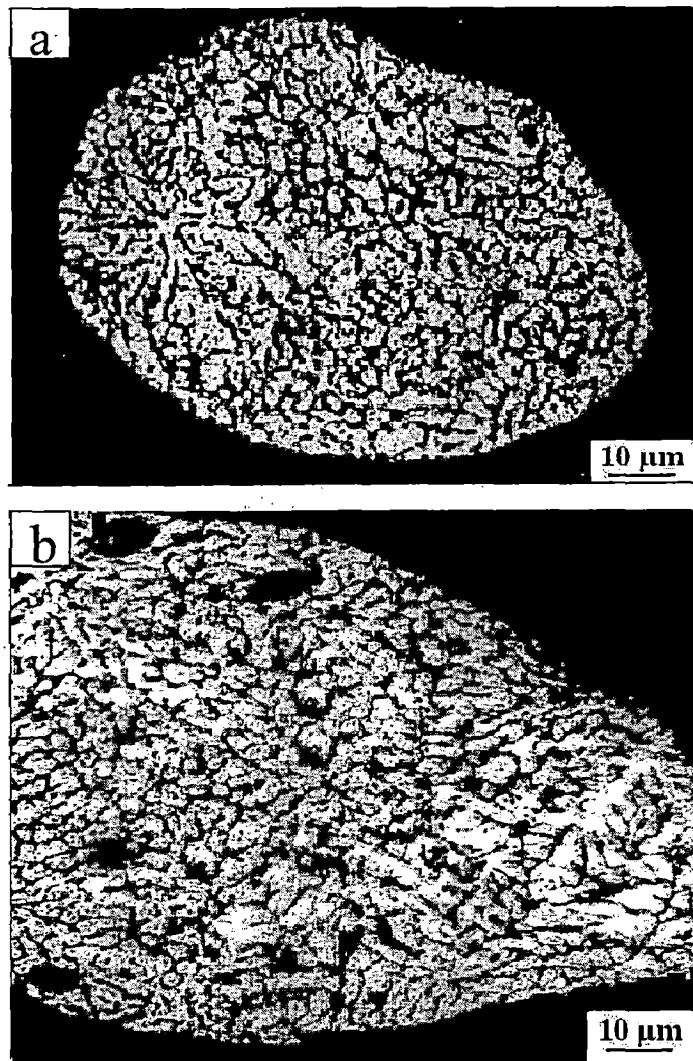


**Fig. 5.20** Microstructure of the cross-section of two different particles (a) and (b)

## 5.4.2 Spray deposit

Optical micrographs were taken at four different locations of the deposit viz. (a) top, (b) middle, (c) bottom and (d) peripheral regions. These micrographs are shown from **figs. 5.21 to 5.25** for different Pb contents varying from 0 to 25%.

**Fig.5.21** shows microstructure of spray formed Al-Si alloy (i.e. no lead). Equiaxed grains of primary Al were observed and Si was present within these grains and along the grain boundary. Dark gray colour in microstructure represents Si phase as revealed by EDAX in **fig.5.16**. The size of the Al grains was about 20-30  $\mu\text{m}$  and size of Si particles was about sub-micron to 5  $\mu\text{m}$ .

Dark black colour represents the Pb phase (as revealed by EDAX in **fig.5.16**) in **figs.5.22 to 5.25**. It can be seen that the Pb distribution is almost uniform throughout the aluminum phase. The size of Pb particles varies from about sub-micron to 10  $\mu\text{m}$  at central regions i.e. top, middle and bottom, about sub-micron to 5  $\mu\text{m}$  at peripheral region in case of 10% Pb. Similarly, the lead particles size varies from about sub-micron to 15, sub-micron to 20 and sub-micron to 25  $\mu\text{m}$  at central (top, middle and bottom) regions and about sub-micron to 10, sub-micron to 15 and sub-micron to 20  $\mu\text{m}$  at peripheral region in case of 15, 20, and 25% Pb, respectively. It can also be seen that the size of the aluminum grains is almost same at the bottom and top regions whereas it is lower at peripheral region. In middle region the grain size is a little bit coarser than at the top or bottom region. The aluminum grain size at central regions i.e. top, middle and bottom is about 5-35  $\mu\text{m}$  and it is about 2-20  $\mu\text{m}$  at peripheral region for all values of the lead content.

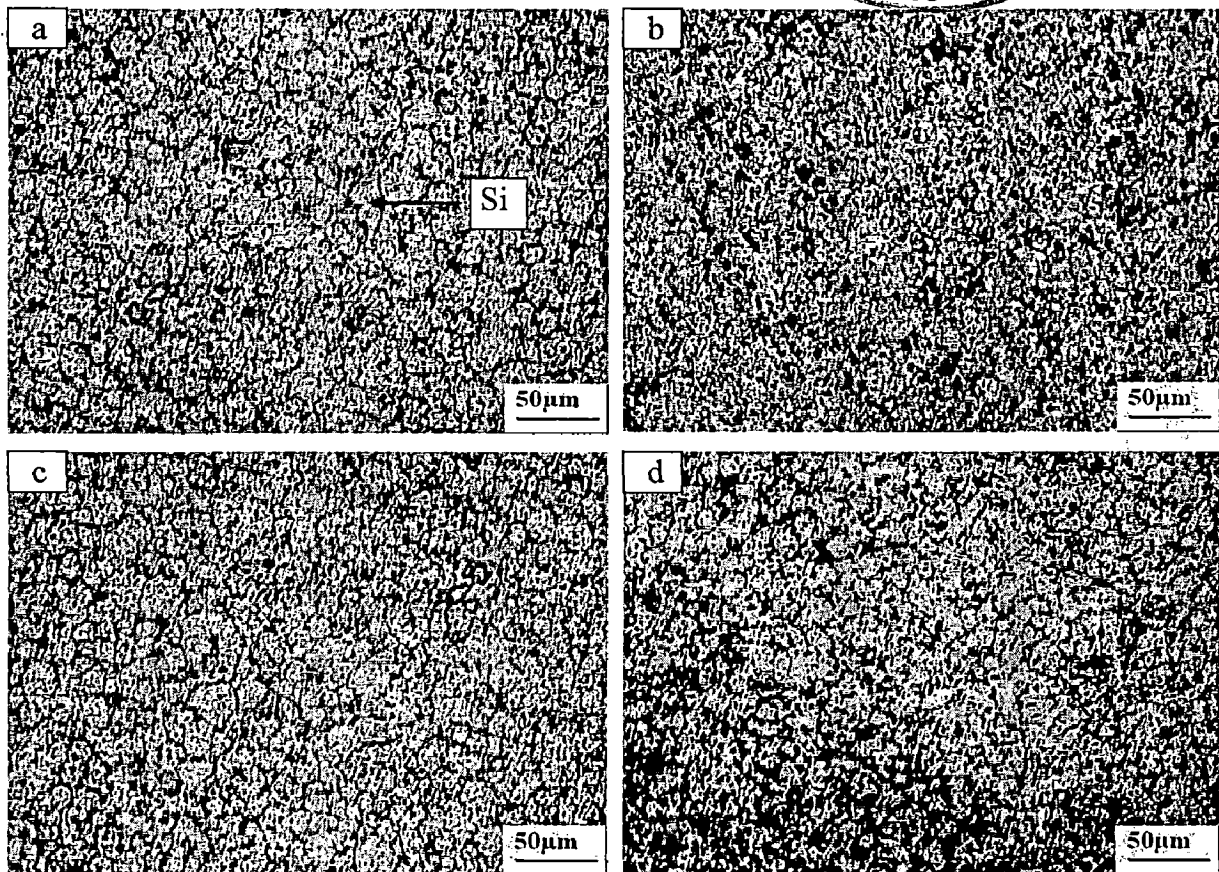
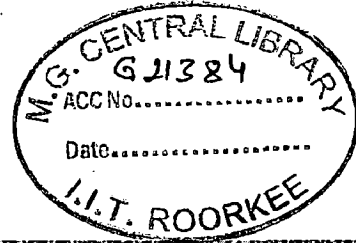


**Fig.5.21** Microstructure of spray deposited Al-6Si alloy showing (a) top; (b) middle; (c) bottom and (d) peripheral regions.

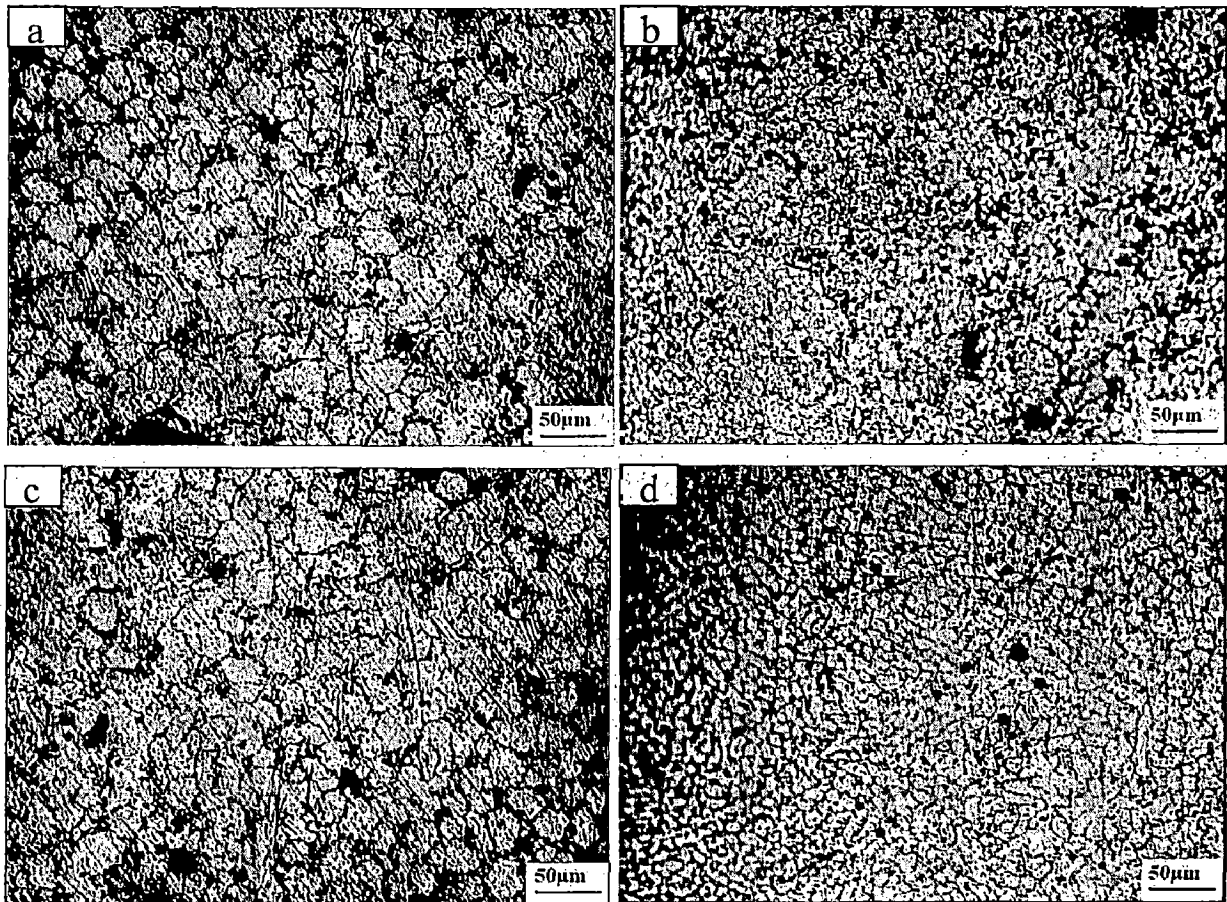


**Fig.5.22** Micrograph of spray deposited Al-6Si-10Pb alloy showing distribution of Pb and Si particles at (a) top; (b) middle; (c) bottom and (d) peripheral regions.

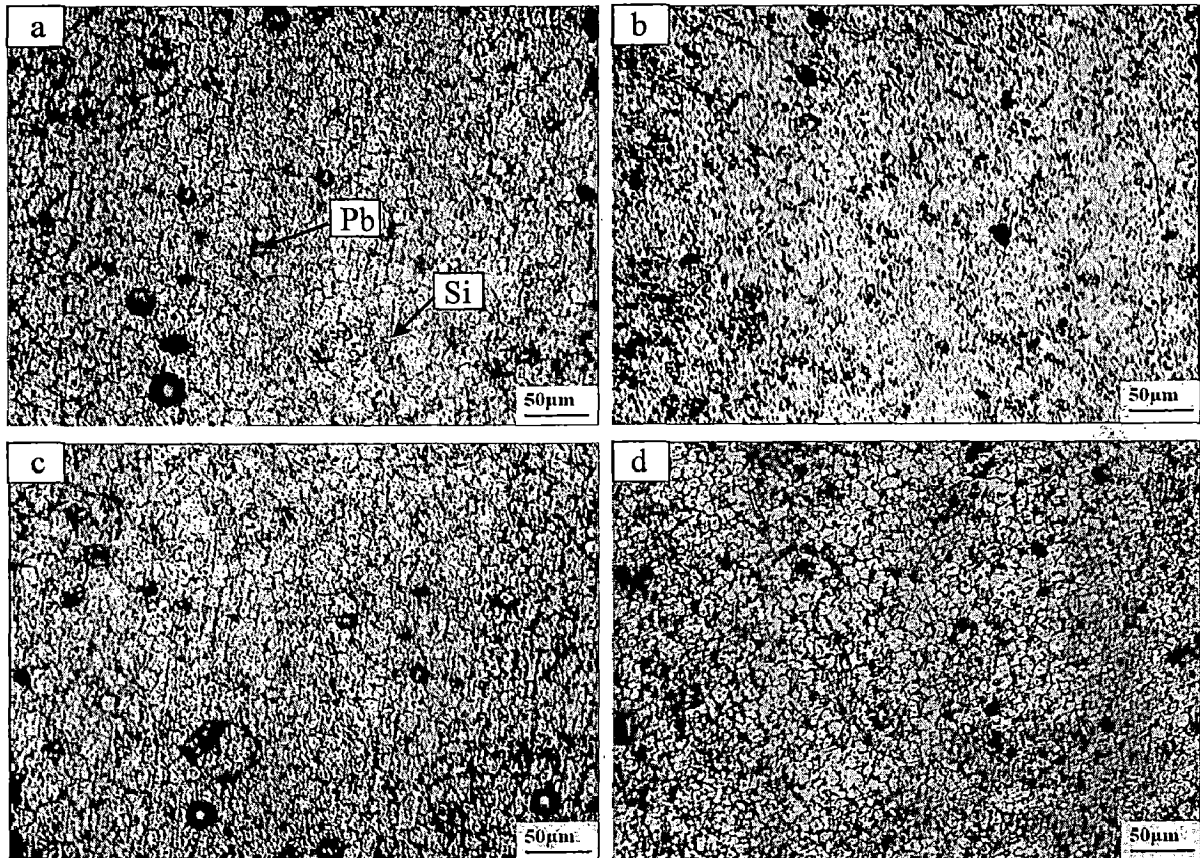


**Fig.5.23** Micrograph of spray deposited Al-6Si-15Pb alloy showing distribution of Pb and Si particles at (a) top; (b) middle; (c) bottom and (d) peripheral regions.



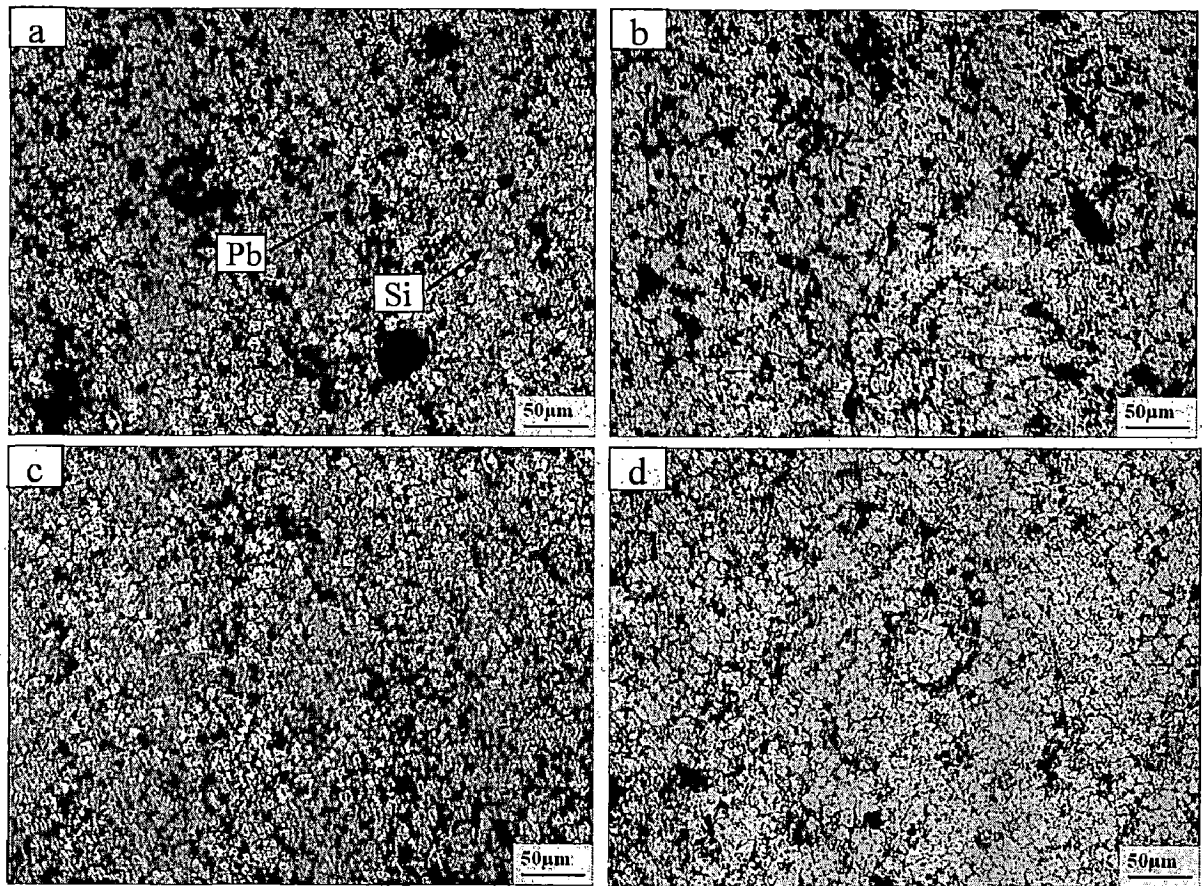


**Fig.5.24** Micrograph of spray deposited Al-6Si-20Pb alloy showing distribution of Pb and Si particles at (a) top; (b) middle; (c) bottom and (d) peripheral regions.

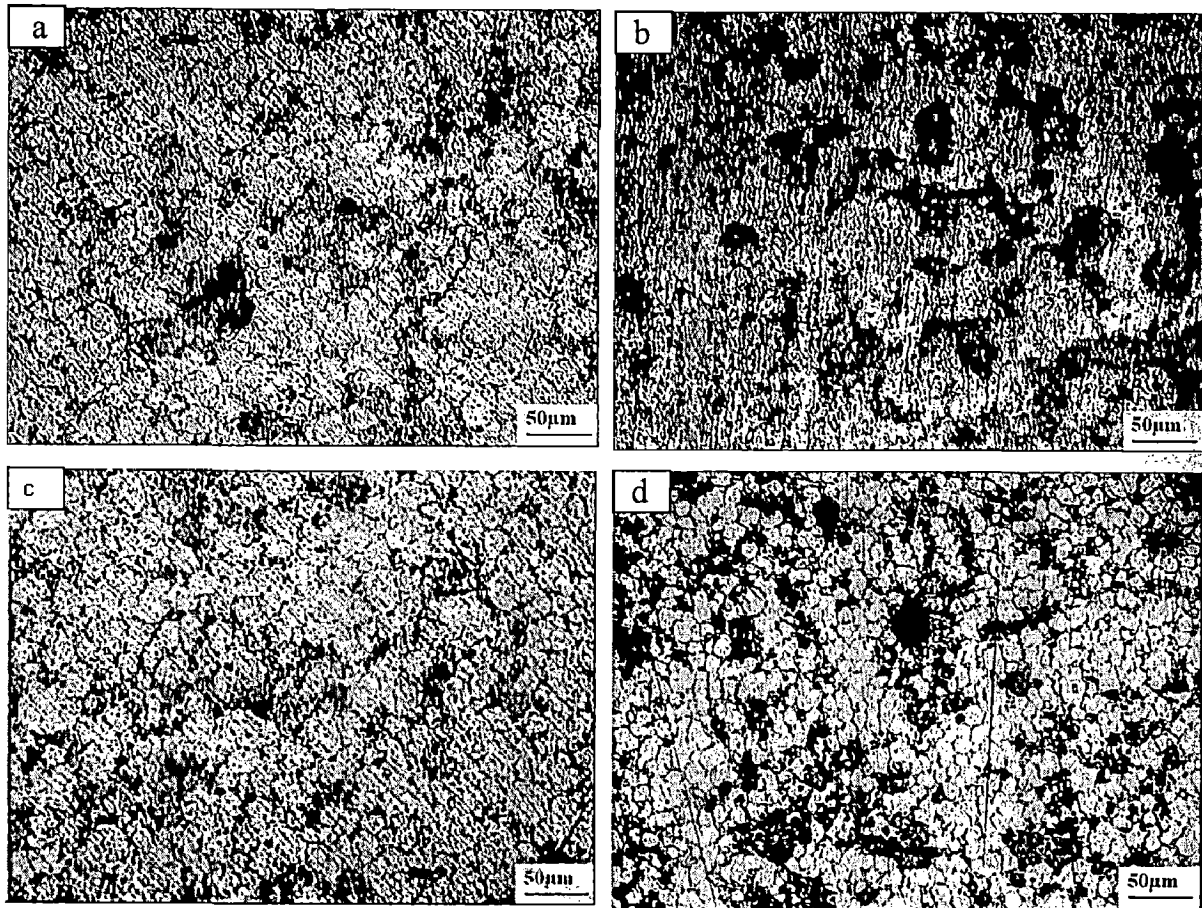


**Fig.5.25** Micrograph of spray deposited Al-6Si-25Pb alloy showing distribution of Pb and Si particles at (a) top; (b) middle; (c) bottom and (d) peripheral regions.

**Fig.5.26** shows the SEM micrographs for (a) 10, (b) 15, (c) 20 and (d) 25% Pb at central region of the deposit. It can be seen that grain boundaries are not as clear as in optical micrographs as percentage of lead increases from 10 to 25%. The white phase is Pb, which is distributed along grain boundaries and inside the Al grains. Maximum amount of lead is on the grain boundaries. Pb particles size varies from sub-micron to 25  $\mu\text{m}$  and it is higher for higher lead content. Color dot maps of Al, Si and Pb distribution in Al-6Si-15Pb alloy are shown in **fig.5.27** which represents a uniform distribution of these elements in the spray deposit.

No change in microstructure, except that more Si, was present along grain boundaries and within the grain for 12% Si alloys with Pb variation from 10 to 25%.

The XRD patterns of Al-6Si-Pb spray deposited alloys are shown in **fig.5.28** for different lead content. These patterns were taken for samples obtained from the centre of the deposit. The diffractograms clearly shows only the three phases Al, Si and Pb in the deposit.

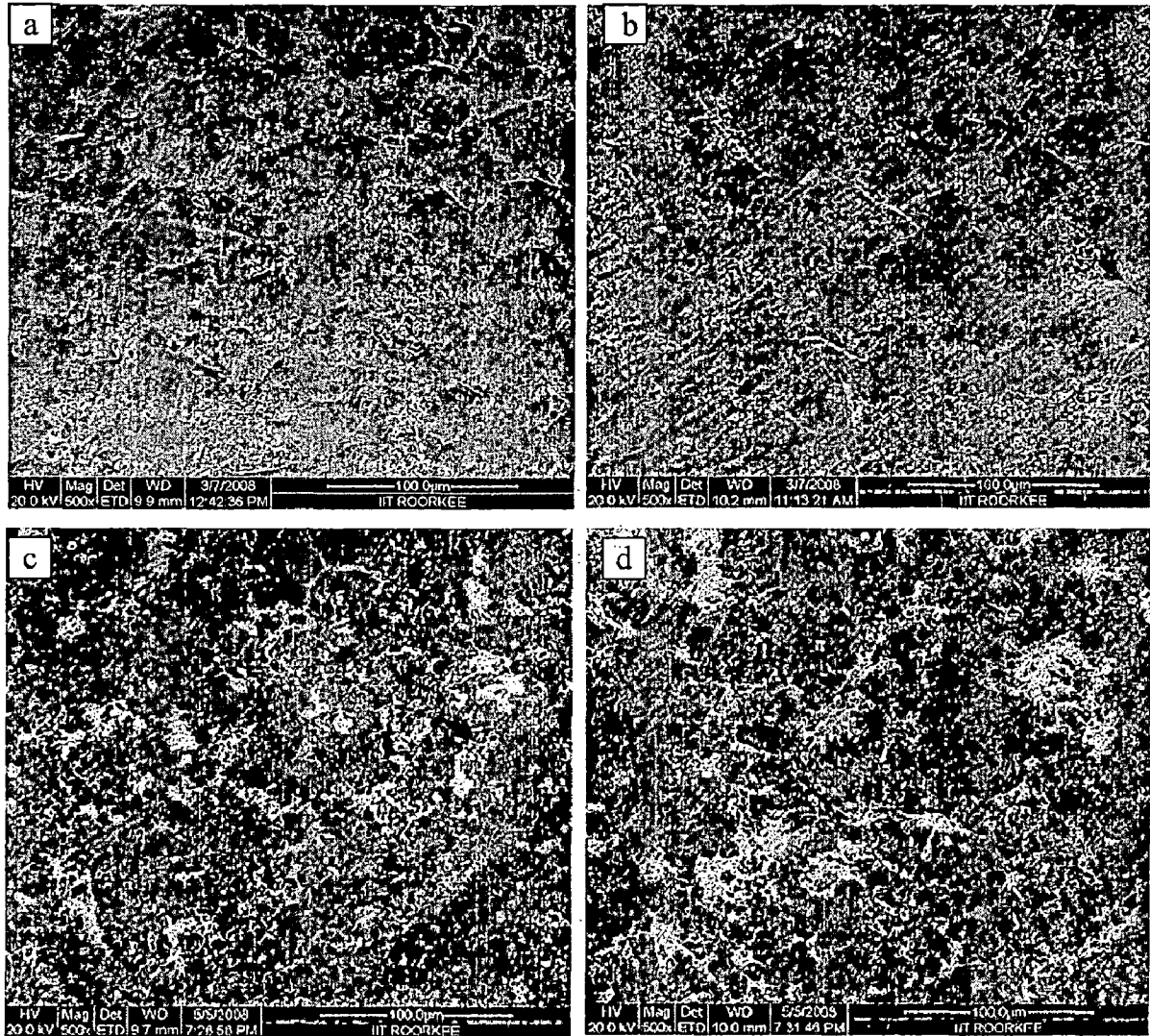


**Fig.5.26** SEM micrographs showing the Pb (white phase) distribution in Al-6Si matrix for (a) 10; (b) 15; (c) 20 and (d) 25 % Pb.

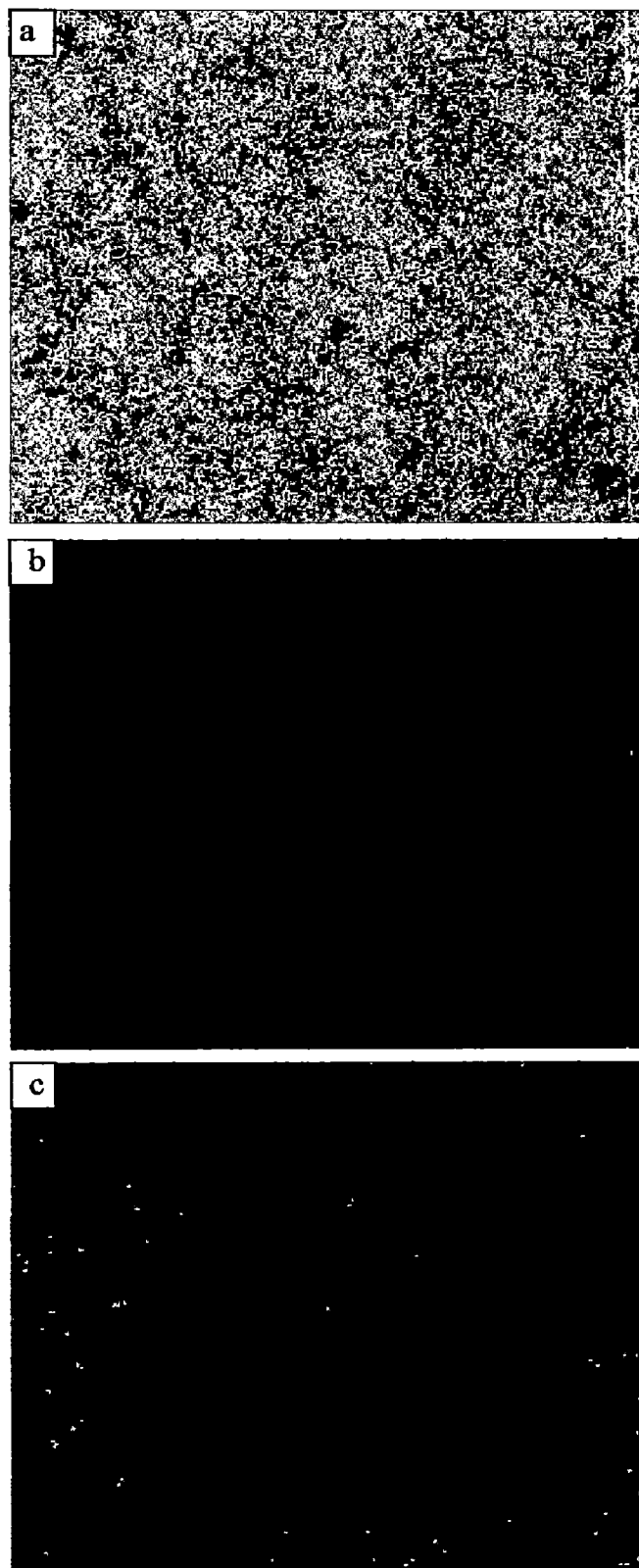


**Fig.5.27** Color dot maps of all three elements: (a) Al; (b) Si and (c) Pb in the Al-6Si-15Pb spray deposit

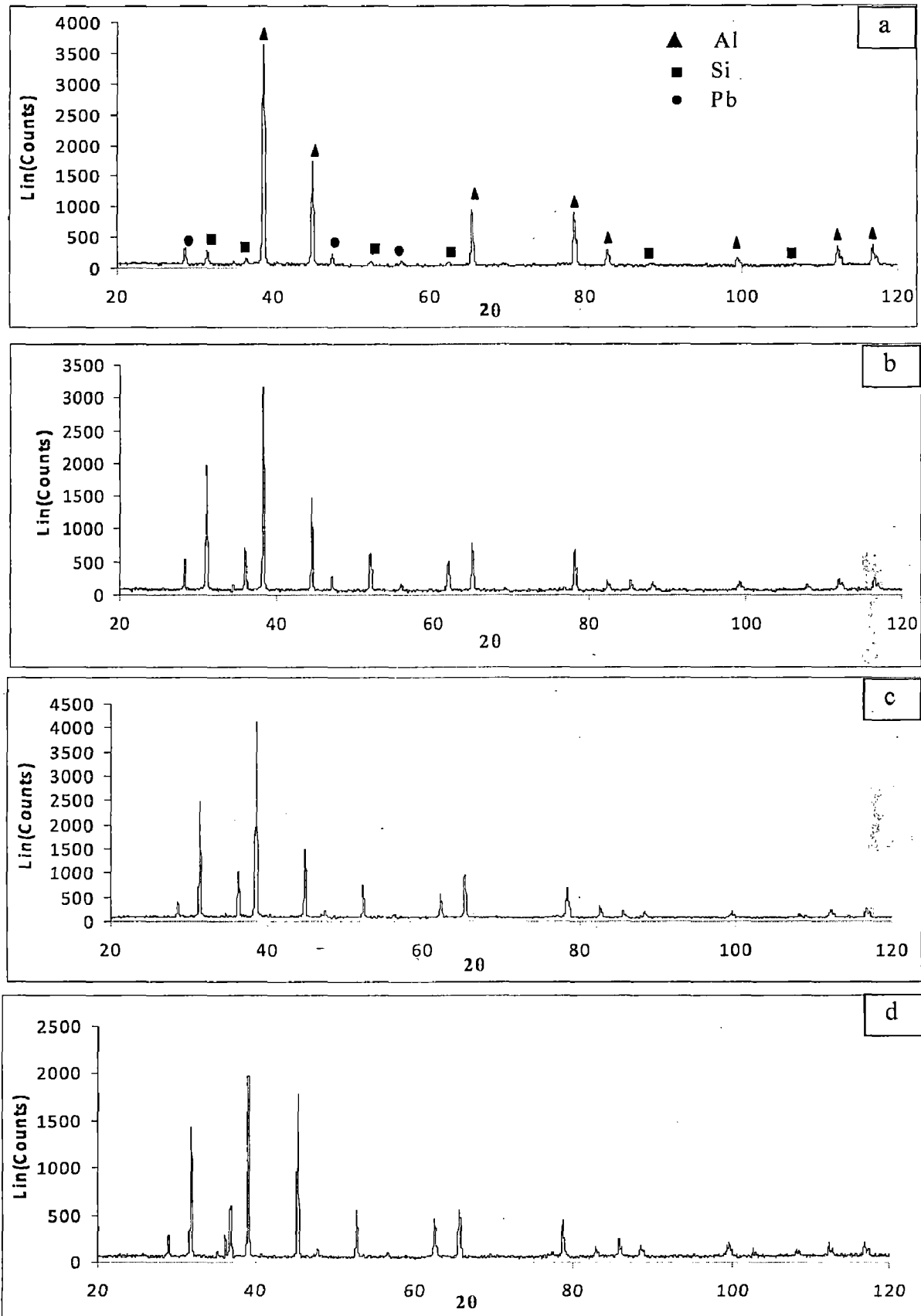


**Fig.5.28** XRD patterns at centre of Spray deposit for different composition of Pb: (a) 10; (b) 15; (c) 20 and (d) 25% in Al-6Si-Pb alloy.

## 5.5 MECHANICAL PROPERTIES

### 5.5.1 Hardness

Variation in hardness with lead content at different distances from centre to periphery of the deposit is shown in **fig.5.29**. It can be seen that the hardness decreases with the increase in lead content for all values of the distances. Also, the hardness value is higher for higher distances from centre to periphery of the deposit. The decrease rate in hardness with the increase in lead content seems to be higher at higher lead content. For example, initially for the increase in lead content from 0 to 15 % the decay rate of hardness with lead content is about 0.5 unit per unit increase in % Pb. Whereas, for the increase in lead content from 15 to 25 % the decay rate in hardness is about 0.8 unit per unit increase in the % Pb.

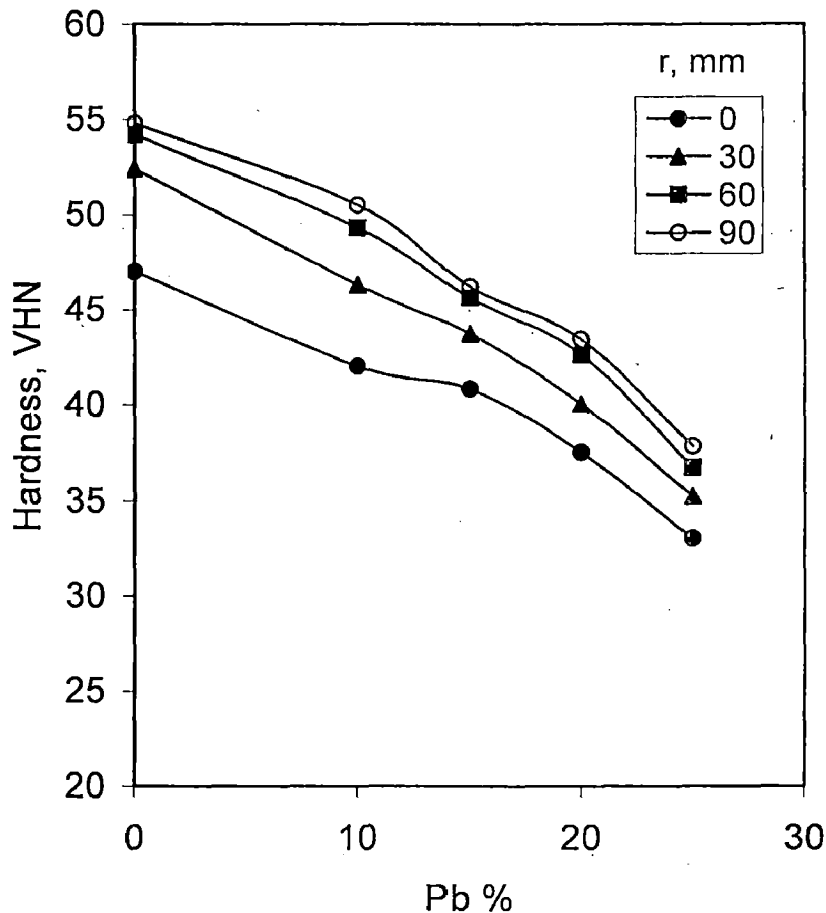


**Fig. 5.29** Variation in hardness with Pb content at different distances from centre to periphery of spray deposit.

The hardness variation with the distance from centre to periphery of the deposit for various lead contents is shown in **fig.5.30**. It can be seen that the hardness increases slowly with the increase in distance. The average rate of increase in hardness is about 0.03 per unit increase in the distance.

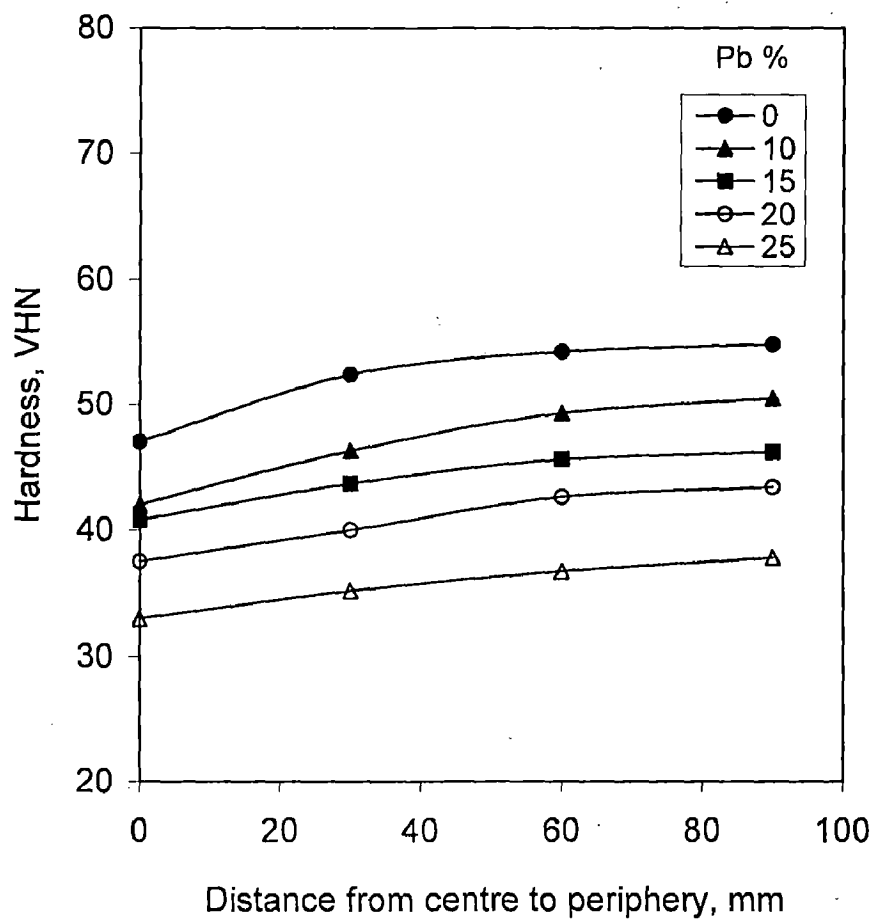


**Fig. 5.30** Variation in hardness with distance from centre to periphery at different Pb content.



Fig.5.31 shows the hardness of deposit as a function of distance from bottom to top (height) of the preform for various lead contents in Al-Si-Pb alloy. The hardness was found almost constant at all the heights of the preform.

The hardness was observed to be higher for 12% silicon content as compared to that of 6% Si as shown in fig.5.32 for Al-Si-15Pb alloy. The hardness values are 41 and 54 for 6 and 12% Si, respectively.

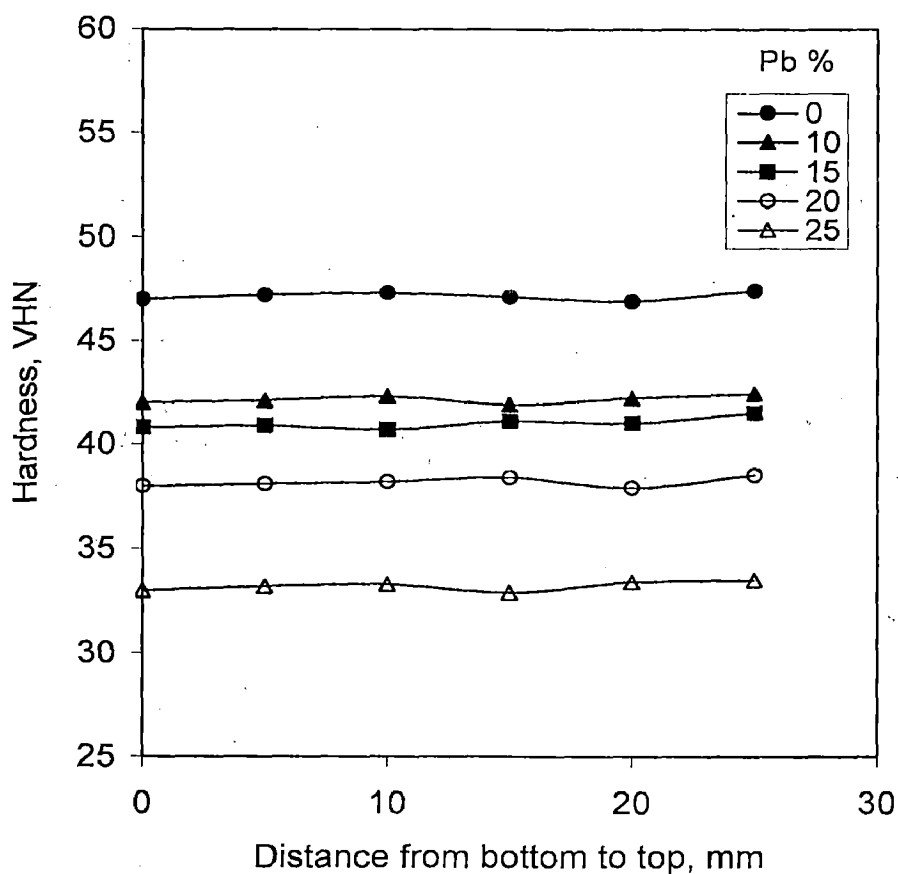
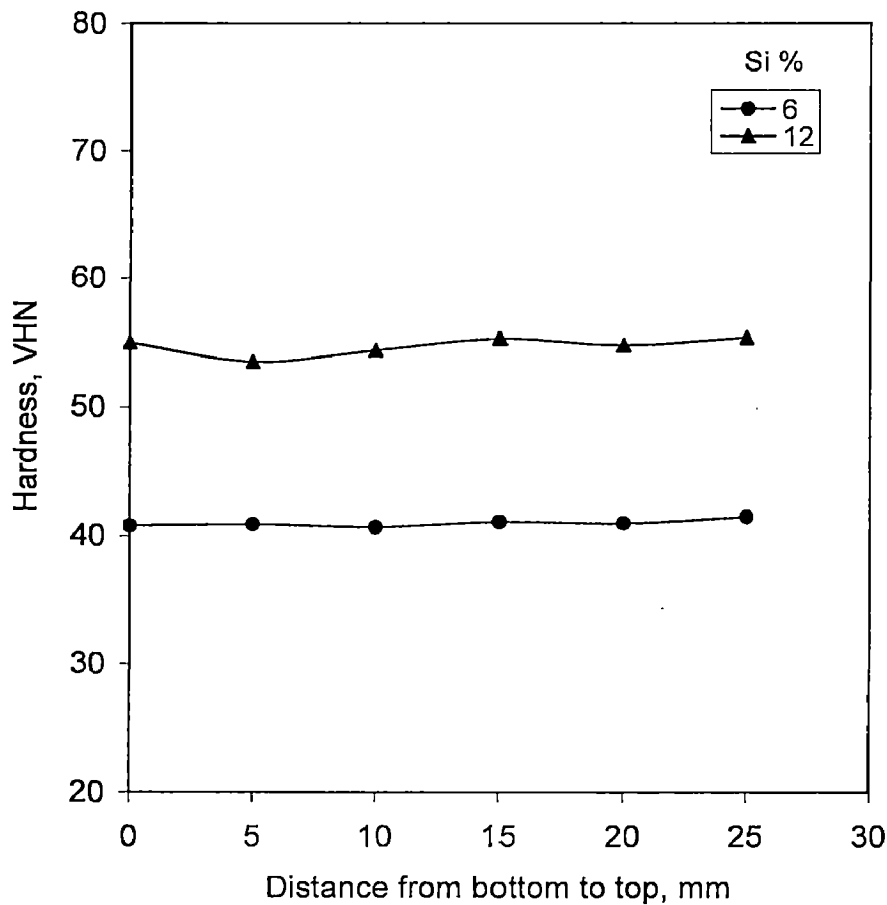


Fig.5.31 Variation in hardness with distance from bottom to top at centre of the deposit.



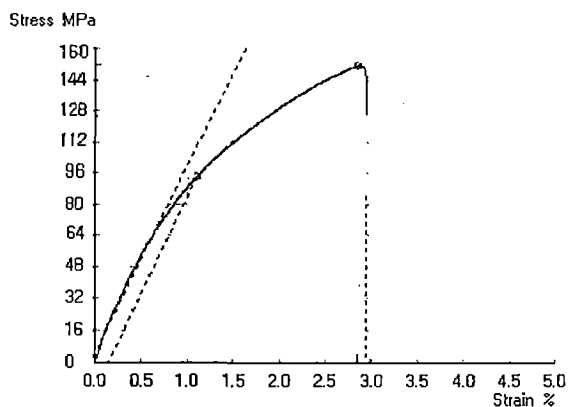
**Fig. 5.32** Variation in hardness with distance from bottom to top of Al-Si-15Pb alloy at centre of the deposit.

## 5.5.2 Strength and Elongation

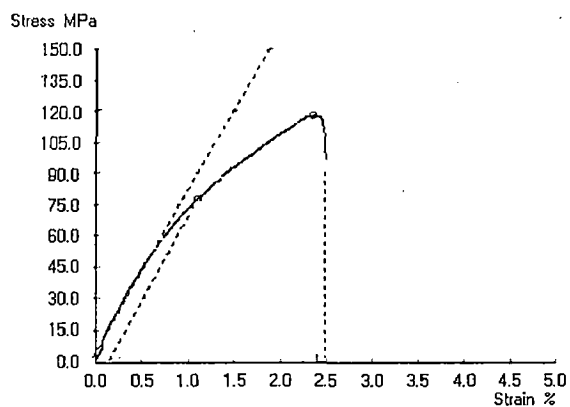
Strength and elongation to fracture of spray deposit were measured as a function of lead content, silicon content and distance from centre to periphery of the deposit.

**Fig.5.33** shows stress-strain plots obtained from the tensile testing machine for different lead contents viz. (a) 0, (b) 10, (c) 15, (d) 20 and (e) 25% in Al-6Si-Pb alloy. Yield point was not observed in any of these plots. Therefore, proof stress was determined at 0.2% strain as shown by dotted lines in the same plots. From these plots, the strain to fracture seems to decrease with the increase in lead content.

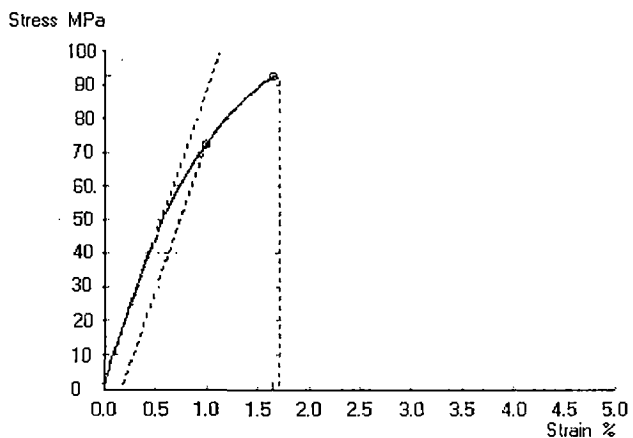
Proof stress and ultimate tensile strength (UTS) obtained from stress-strain plots as a function of lead contents are shown in **fig.5.34**. It can be seen that both the stresses



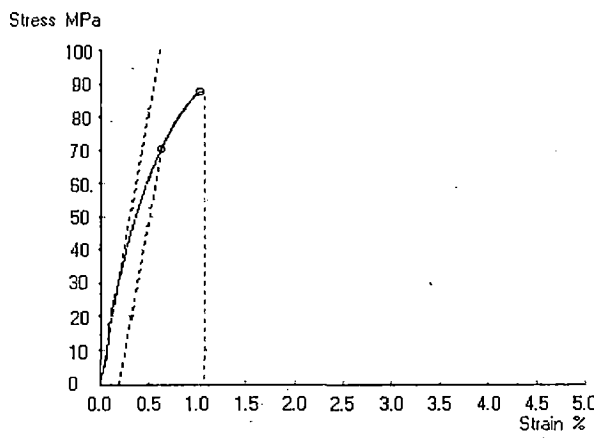
(a)



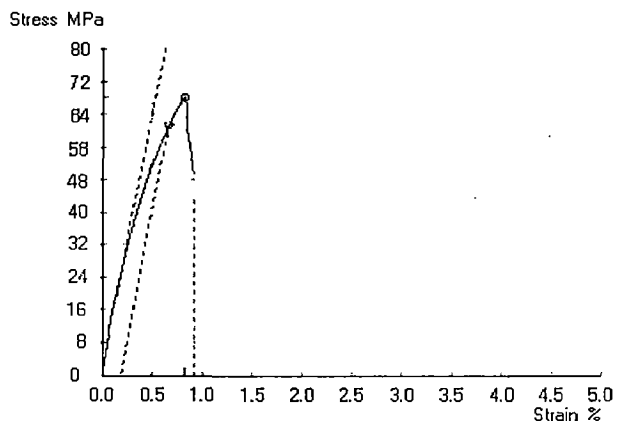
(b)



(c)



(d)



(e)

**Fig. 5.33** Stress-strain plots for (a) Al-6Si, (b) Al-6Si-10Pb, (c) Al-6Si-15Pb, (d) Al-6Si-20Pb and (e) Al-6Si-25Pb.

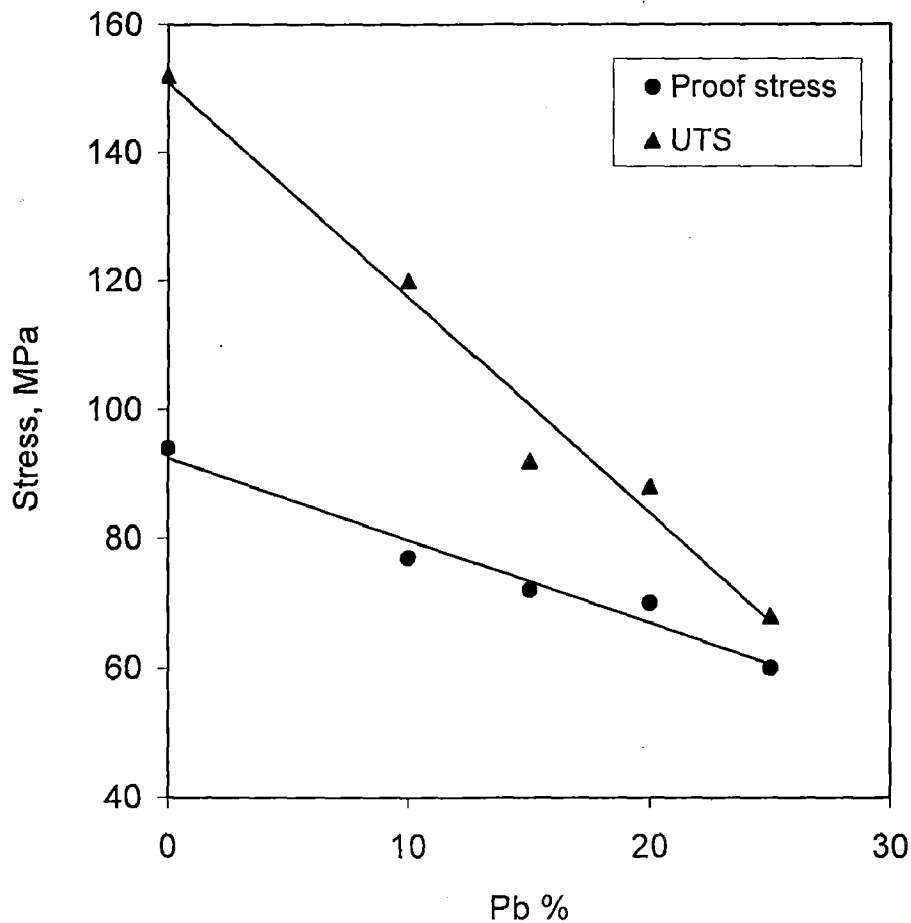


**Fig. 5.34** Variation in stress of spray formed Al-6Si-Pb alloys with Pb content.

decreases with the increase in lead content. However, the rate of decrease with the increase in lead content is higher in case of UTS as compared to that of proof stress. The rate of decrease in UTS is 3 MPa per unit increase in %Pb. While, the decay rate of proof stress is 1.2 MPa per unit increase in %Pb.

Variation in percentage elongation of spray deposit with lead content is shown in **fig.5.35**. The % elongation decreases at the rate of 0.1 per unit increase in % lead.

**Fig.5.36** shows the proof stress and UTS variation with distance from centre to periphery of the preform for 6 and 12% silicon. Both stresses increase with the increase in distance almost at the same rate for both 6 and 12% silicon. The rate of increase of stress is about 0.1 MPa per mm increase in distance. Both proof and UTS are higher for 12% silicon as compared to that of 6% silicon.

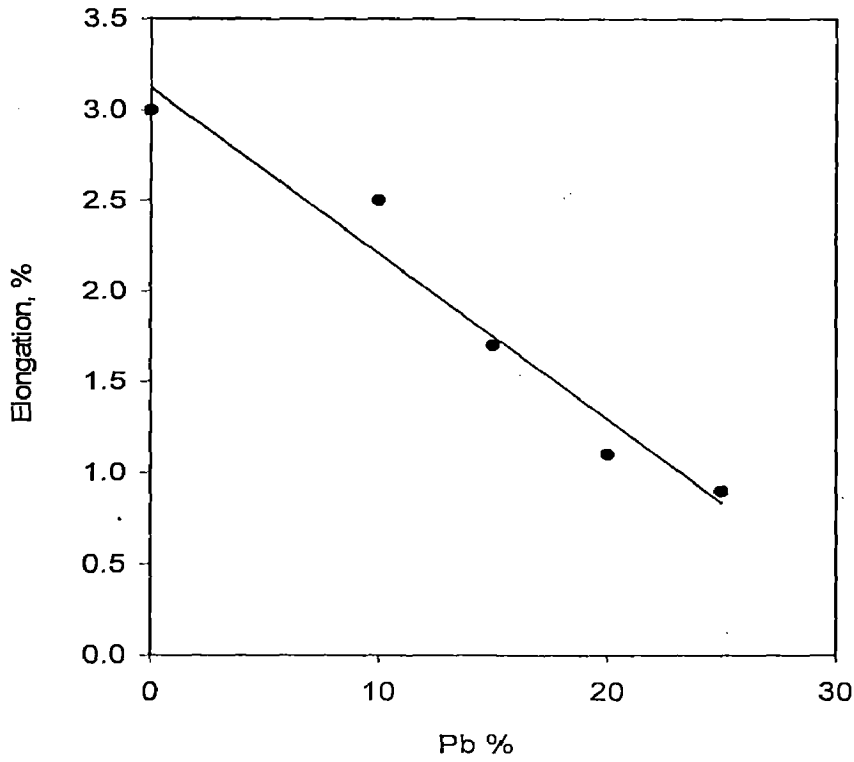


Fig. 5.35 Variation in elongation of spray formed Al-Si-Pb alloy with Pb content.

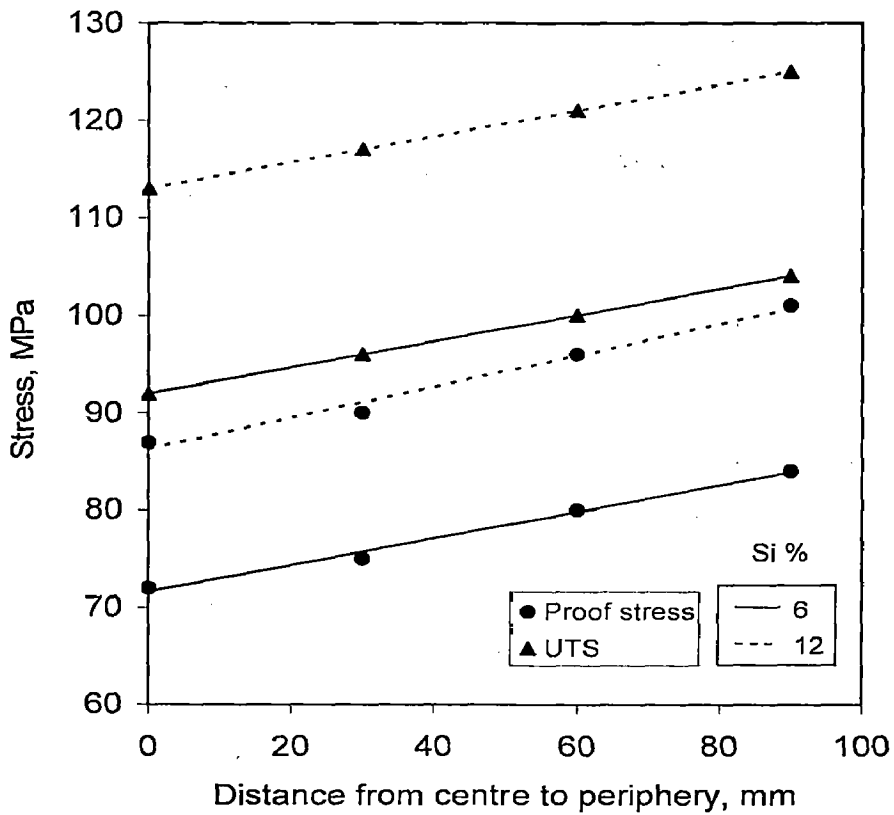
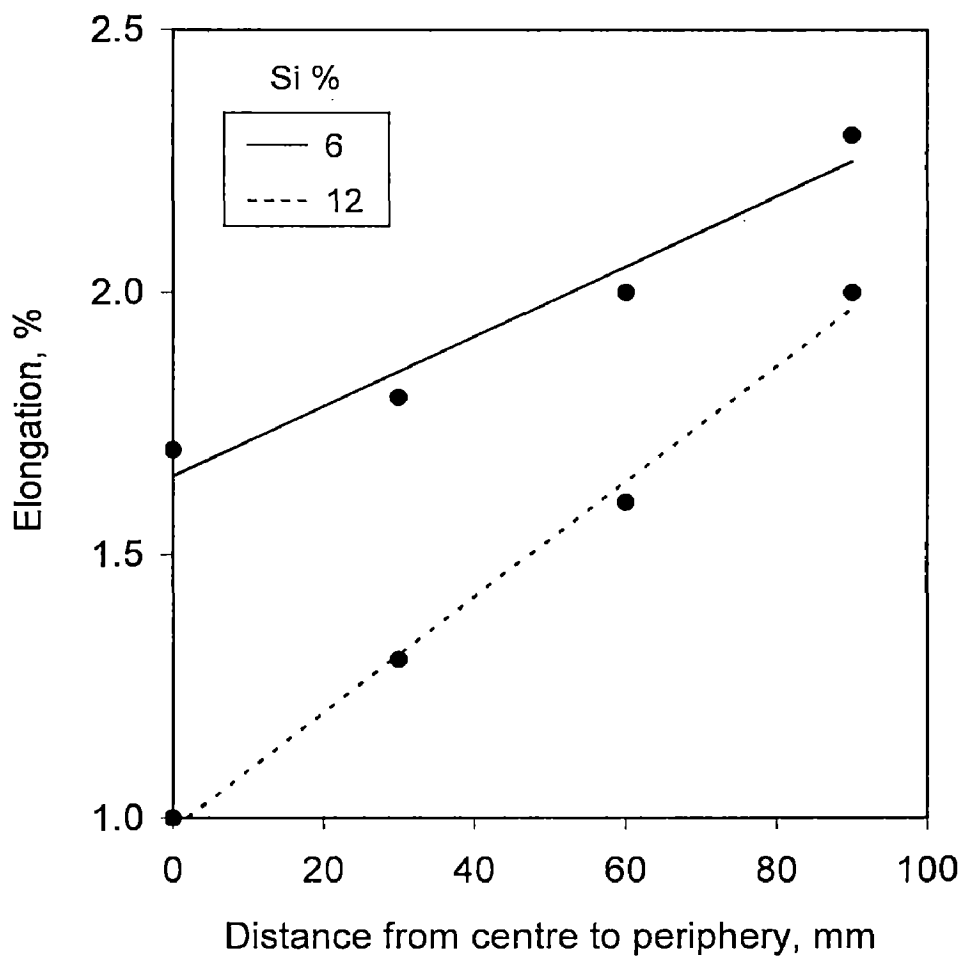


Fig. 5.36 Variation in stress of spray formed Al-Si-15Pb alloy with distance from centre to periphery of the deposit for 6 and 12 % Si.

Variation of % elongation with the distance from centre to periphery of spray deposit is shown in **fig.5.37** for 6 and 12 % silicon in Al-Si-15Pb alloy. Percentage elongation increases with the increase in distance. The rate of increase in percentage elongation is higher for 12% silicon as compared to that of 6% silicon. It increases at the rate of 0.005 and 0.01 for 6 and 12% silicon, respectively. The % elongation to fracture is higher for 6% silicon as compared to that of 12% silicon.



**Fig. 5.37** Variation in elongation of spray formed Al-Si-15Pb alloy with distance from centre to periphery of the deposit at 6 and 12 % Si.

## 5.6 TRIBOLOGICAL PROPERTIES

### 5.6.1 Wear Rate

Wear rate as a function of applied load for different lead content in Al-6Si-Pb alloy is shown in **fig.5.38**. Wear rate increases with the increase in applied load for all values of the lead contents. Also, the wear rate is higher for lower lead contents. In the initial stage, wear rate increases rapidly up to a load of 30 N and then slowly up to a load of 50 N. For example, the wear rate increases at the rate of 0.75 units per unit increase in applied load in the initial stage i.e. up to a load of 30 N. Beyond this load the wear rate increases at the rate of 0.25 units per unit increase in the applied load up to 50 N. Beyond a load of 50 N, wear rate again increases but at a higher rate as compared to that of up to a load of 30 N. For example, it increases at the rate of 1.0 unit per unit increase in applied load beyond 50 N.

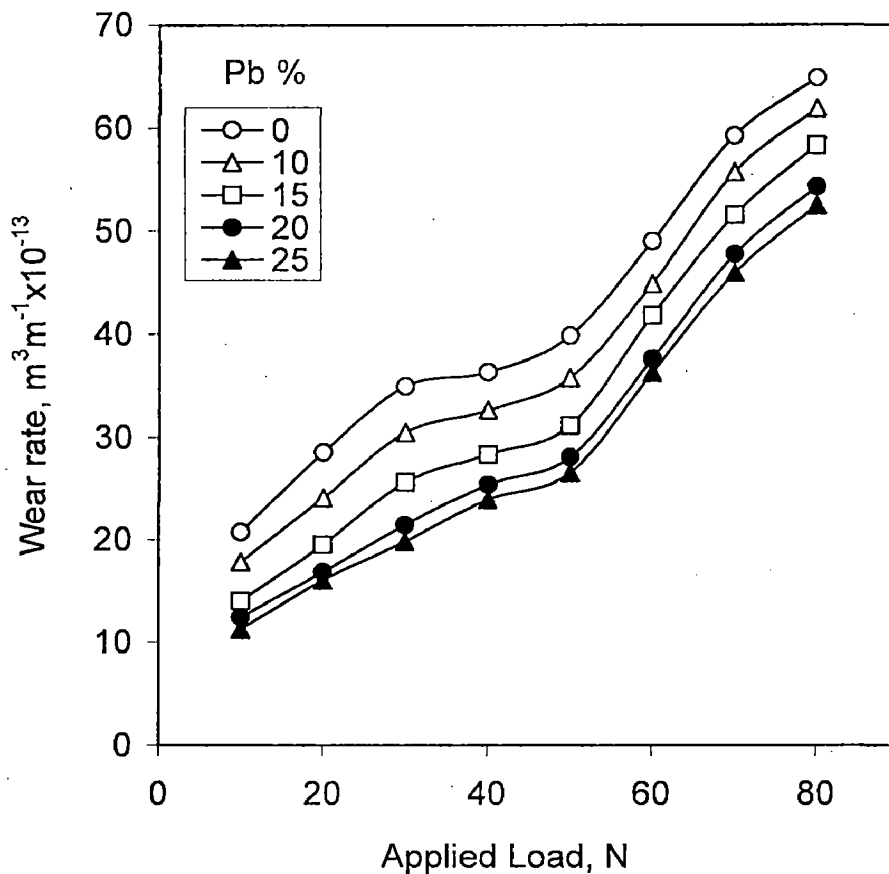


**Fig. 5.38** Variation in wear rate of Al-6Si-Pb alloy as a function of applied load for different Pb content.

**Fig.5.39** shows the variation of wear rate of spray deposit as a function of lead content at different applied loads. Wear rate decreases linearly with the increase in lead content at all the applied loads. Obviously, the wear rate is higher at higher load. The decay in wear rate with the increase in lead content seems to be the same at all the loads.

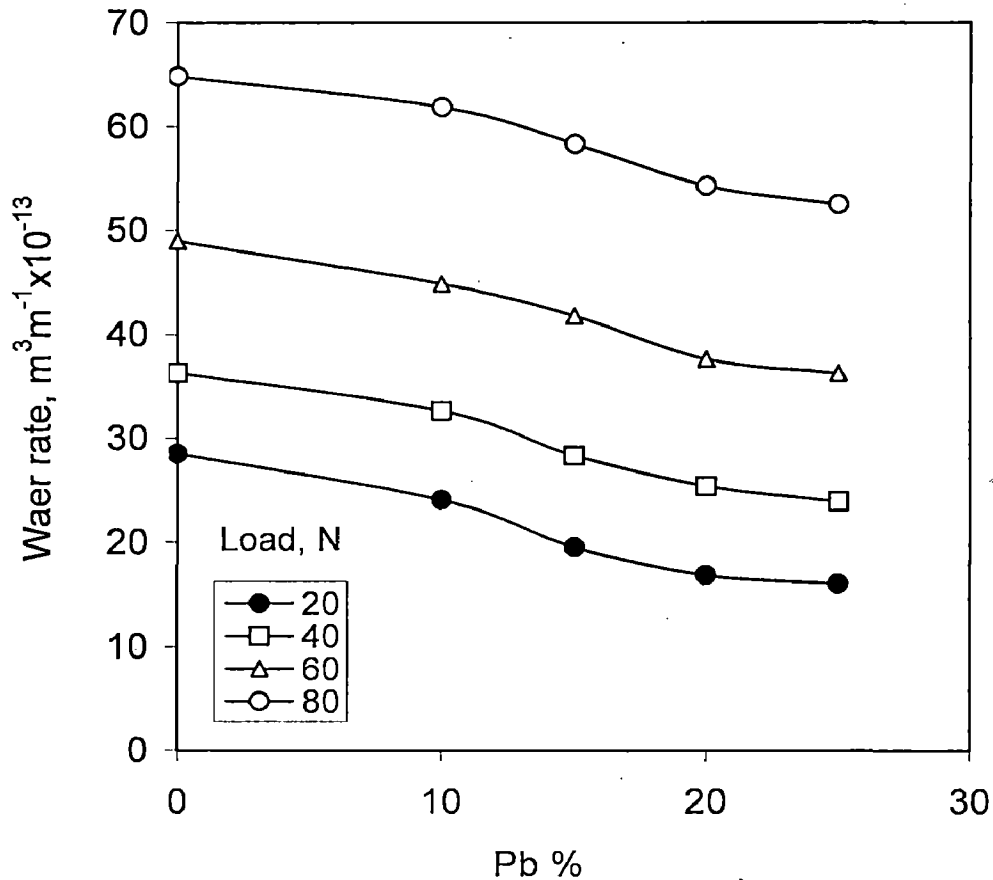


**Fig. 5.39** Variation of wear rate with Pb content in spray deposited Al-6Si-Pb alloy at different applied load.

The variation of wear rate with distance from centre to periphery of the deposit at different loads is shown in **fig.5.40**. It can be seen that the wear rate decreases with the increase in distance at all the loads. The decay rate in wear with the increase in distance also seems to be the same whatever be the applied load. For example, the decay rate in wear is about 1.2 units per unit increase in distance from centre to periphery of the deposit irrespective of the applied load.



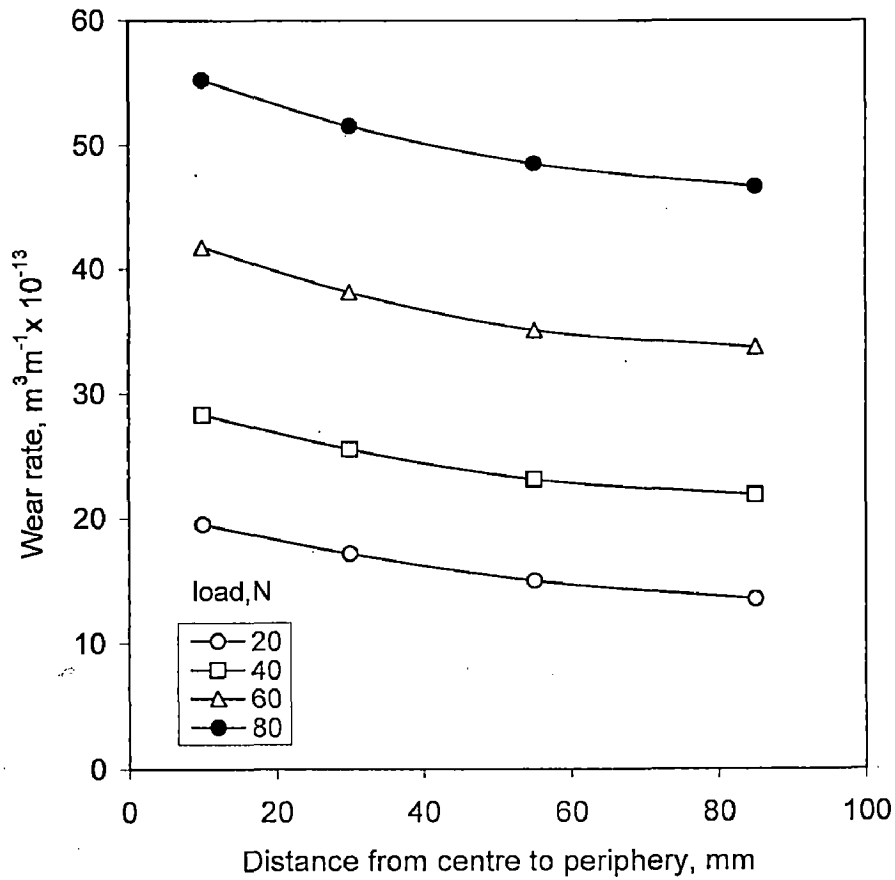
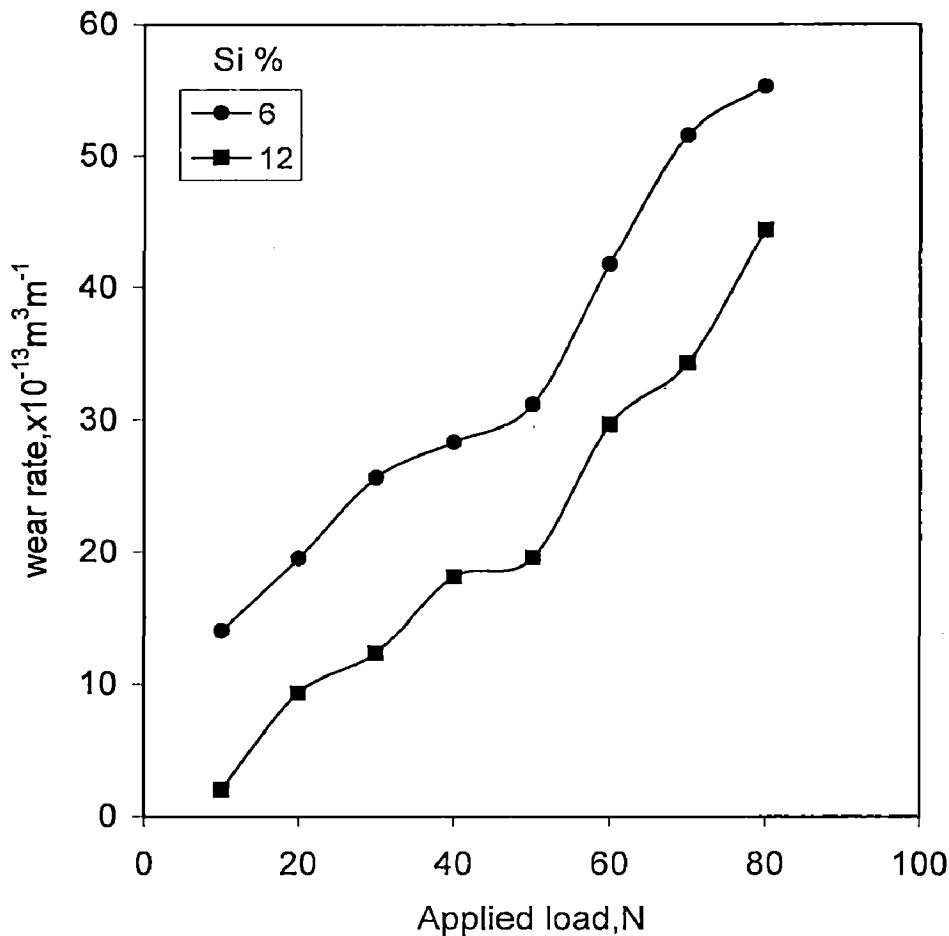


Fig. 5.40. Variation in wear rate of spray formed Al-6Si-15Pb alloy with distance from centre to periphery at different loads.

Variation of wear rate with applied load for 6 and 12 % Si in Al-Si-15Pb is shown in fig.5.41. It can be seen that the trend in the variation for 12% Si is almost similar to that of at 6 % Si. The wear rate of 12 % Si alloy is lower than that of 6 % Si.



**Fig.5.41** Variation in wear rate of spray formed Al-Si-15Pb alloy as a function of applied load for 6 and 12 % Si.

## 5.6.2 Coefficient of friction

**Fig.5.42** shows the variation of coefficient of friction with applied load at different lead contents in Al-6Si-Pb alloys. It can be observed that the coefficient of friction decreases rapidly up to a load of 40 N at all values of the lead contents. For example, the average decay rate of the coefficient of friction up to a load of 40 N is 0.01 per unit increase in the load. Beyond this load the friction coefficient is almost constant. The coefficient of friction is lower for higher lead content. For example, the coefficient of friction for 0 % and 25 % Pb are 0.78 and 0.48, respectively at a load of 10 N.

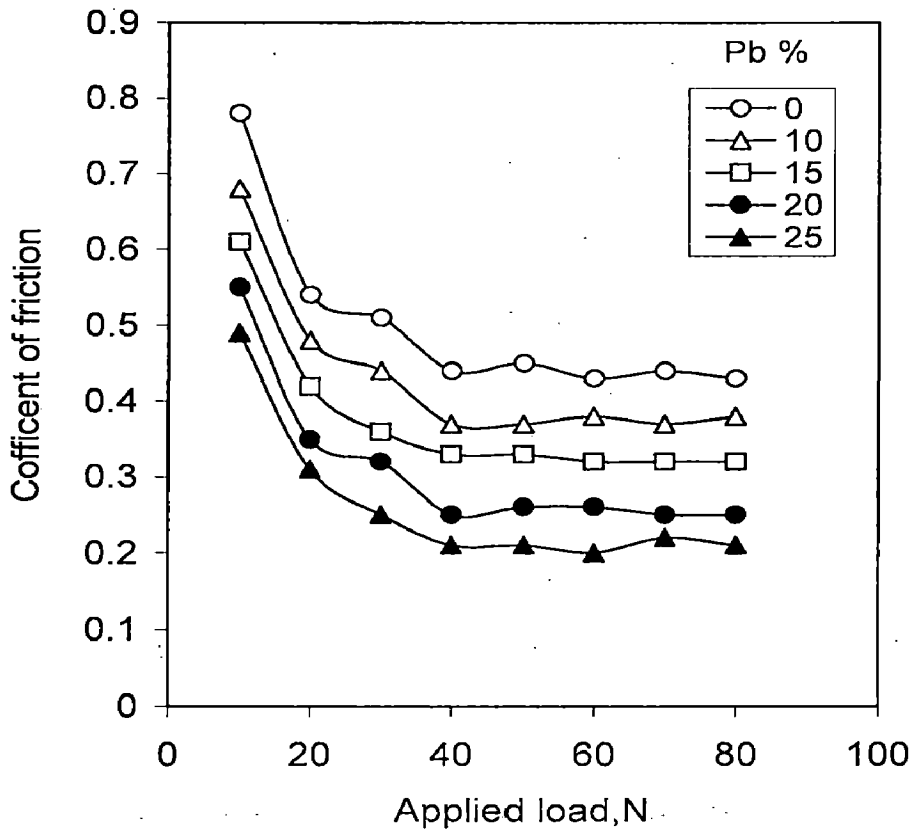


Fig.5.42 Variation in coefficient of friction with applied load at different % of Pb in Al-6Si-Pb alloy.

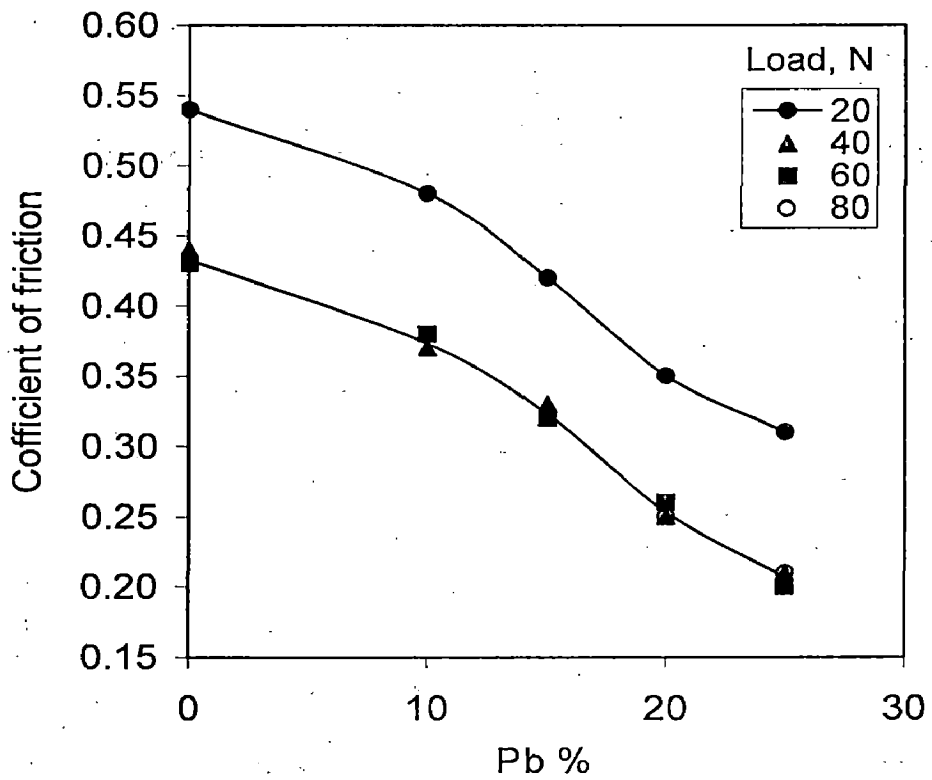


Fig. 5.43 Variation in coefficient of friction with Pb content in spray deposit at different applied load.

### 5.6.3 Worn-out surfaces analysis

Scanning electron micrographs of worn-out surfaces of wear test specimen at different applied loads viz. 10, 40, 60 and 80 N for Al-6Si-15Pb spray formed alloy are shown in **fig. 5.44**. At a load of 10 N, it can be seen that there are primarily small particles on the surface. Some grooves and a white colour discontinuous film can also be observed. White small particles are also present inside the grooves. The size of particles varies roughly from submicron to 50  $\mu\text{m}$ .

At a load of 40 N, it can be seen that there is a white layer/ film of large size as compared to that of at a load of 10 N. Very few particles are also present in the deep recess.

At a load of 60 N, there are long grooves of black colour. The white film also seems to be elongated in one direction.

At a load of 80 N, large damage appears to the white colour film. There are more deep black grooves on the surface. White film is covering lesser area than that of at other loads.

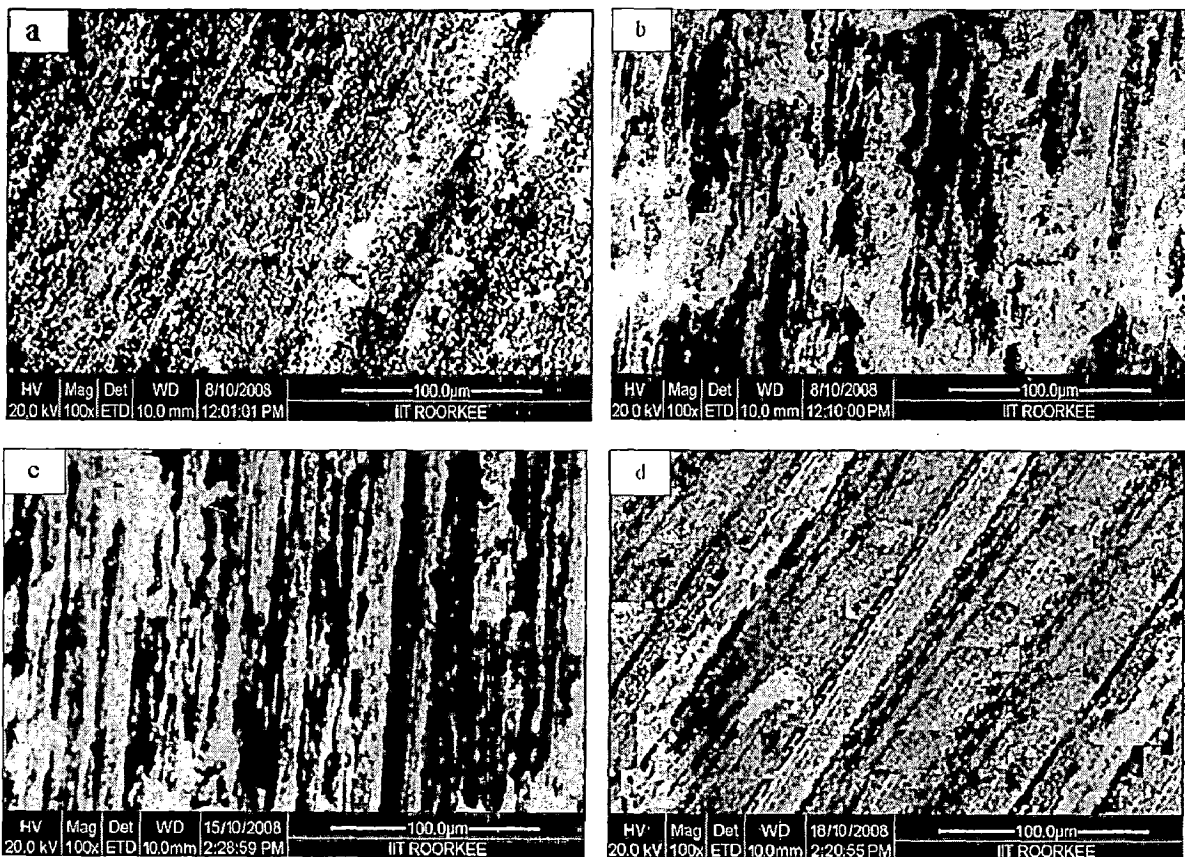


**Fig.5.44** Scanning electron micrographs of worn out surfaces of wear test specimen at different applied loads: (a) 10 N; (b) 40 N; (c) 60 N and (d) 80 N for 15% Pb alloy.

### 5.6.4 Worn-out debris analysis

XRD patterns of the wear debris of Al-6Si-15Pb alloy at two different loads are shown in **fig. 5.45**. This analysis shows that at lower load (30 N) there is oxidation of the alloying elements and hence there is oxidative wear. At high load (70 N) there is some metal without oxidation as represented by Al, Si and Pb peaks and hence there is metallic wear.

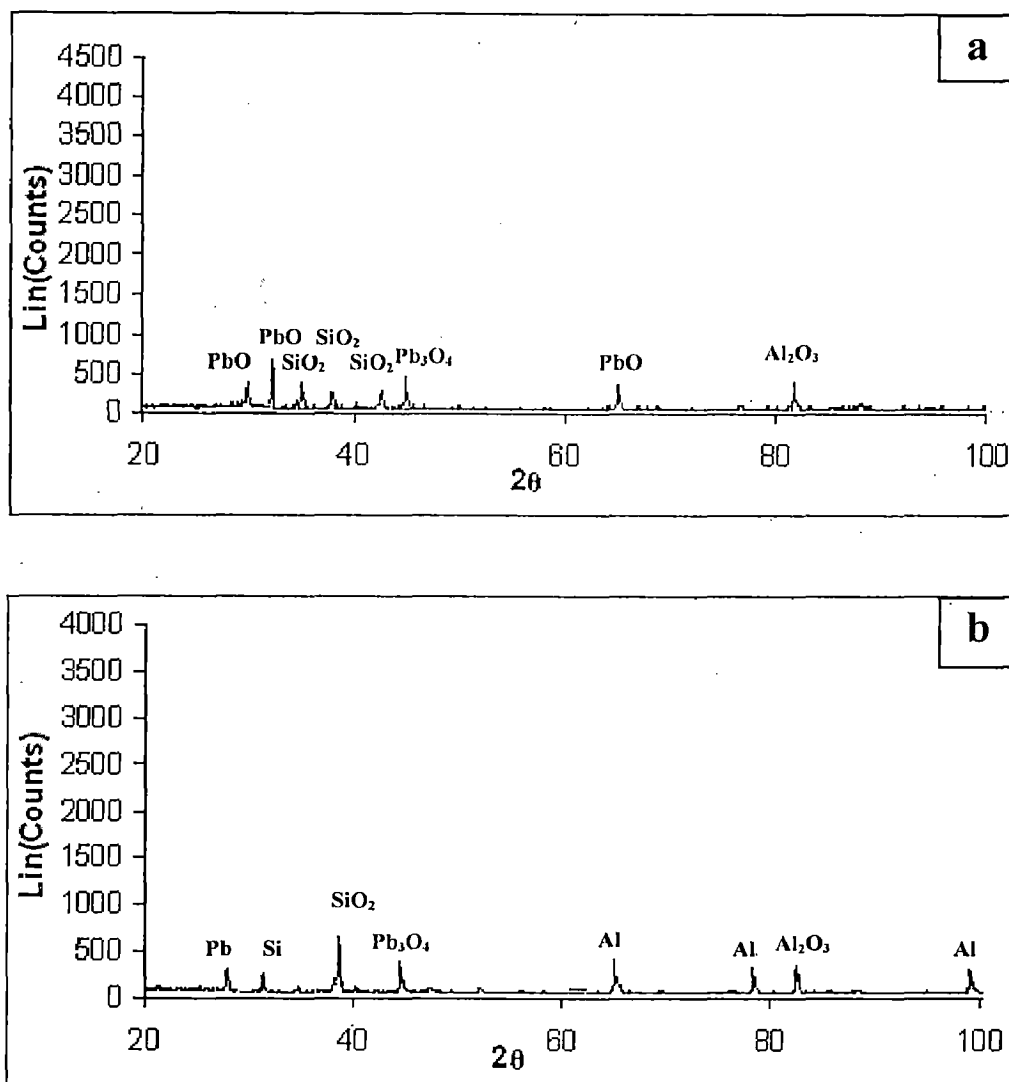


**Fig.5.45** XRD patterns for the wear debris of Al-6Si-15Pb alloy at the load of (a) 30 N and (b) 70 N.



**CHAPTER-6**  
**DISCUSSION**

### 6.1 ATOMIZER CHARACTERISTICS

In present design of nozzle the opposite axes of slit do not intersect at a common point in contrast to the conventional design of the nozzle. Also, the gas flows parallel to the melt delivery tube as represented in **fig.6.1**. Therefore, metal stream and droplets have more freedom to move towards periphery of gas jet as compared to that of conventional nozzle (**fig. 2.1**) where gas jets impinge on the melt stream and thereby it can produce more uniform thickness of the spray deposit.

Two important characteristics of the gas atomizer are the gas velocity field formation and the gas discharge coefficient.

#### 6.1.1 Gas velocity field formation

Aspiration region was experienced up to 12 mm axial distance of the nozzle, beyond this distance pressure build up region was observed. The aspiration occurs in the nozzle due to the following gas flow phenomenon. According to Bernoulli's equation the sum of pressure and kinetic energies is constant in fluid flow and is given by the following expression [80].

$$\frac{P}{\rho} + \frac{v^2}{2} = \text{constant} \quad (6.1)$$

Therefore, the pressure drops (aspiration) at the exit of melt flow tube because of fast flowing gas in the vicinity of the tube as shown in **fig.6.1**. Due to this low pressure region i.e. aspiration the gas will start to enter in this low pressure region from the gas jet and neutralize the aspiration effect after traveling a certain distance i.e. 12 mm in the present study.

In pressure build up region the maximum centre line velocity was found at 25 mm below the nozzle. Initially the velocity increases to some maximum value at this distance and then it decreases at all plenum pressures. The maxima in velocities were

observed at different axial distances for different radial distances in the present nozzle. The gas jet forms a cone below the atomizer and therefore as the cone surface moves downward, the point of maximum velocity will also move downward with the axial distance. Beyond 25 mm axial distance gas jet will behave like a normal gas jet and its behavior could be explained as reported elsewhere [50,58].

The gas velocity was observed to be constant up to about 10 mm radial distance in case of 25 and 50 mm axial distances. It can be due to the value of annular slit diameter of present atomizer which is about 16 mm and it is hollow to insert melt delivery tube. So, gas will move towards this hollow region from the outer region of jet. This movement may prevent decay up to some radial distance and thereby also causing a rapid decay beyond it. Beyond 50 mm axial distance, the effect of the hollow region will vanish and there will be continuous decrease in gas velocity with the radial distance.

The gas flow field of the present atomizer is having widely varying gas velocity depending on axial and radial distances (**fig.5.1 to fig.5.8**). The literature review in section 2.2 suggests that this gas velocity in pressure built up region can be simply correlated by the following power function:

$$v_z = a v_{z0}^b z^c (r+1)^d \quad (6.2)$$

Where,  $v_z$  is the gas velocity at any location in the gas field created by the atomizer,  $v_{z0}$  is the maximum gas velocity at zero radial distance,  $z$  is axial distance from nozzle,  $r$  is the radial distance from the axis of atomizer, 'a' is a constant and 'b', 'c' and 'd' are exponents to be determined. Their values are determined by multi dimensional regression analysis [81] and these are  $a = 1.5$ ,  $b = 1.2$ ,  $c = -0.45$  and  $d = -0.27$ . Substituting these values in above equation results the following equation.

$$v_z = \frac{1.5 v_{z0}^{1.2}}{(r+1)^{0.27} z^{0.45}} \quad \text{for } z > 25 \text{ mm} \quad (6.3)$$



Equation 6.3 shows that the exponent of  $v_{z0}$  is higher than that of  $r$  and  $z$ . Therefore,  $v_{z0}$  has more effect on  $v_z$  as compared to that of  $r$  and  $z$ . The exponent of the  $z$  is higher than that of  $r$ , hence gas velocity decreases more rapidly with the increase in  $z$  as compared to that of  $r$ .

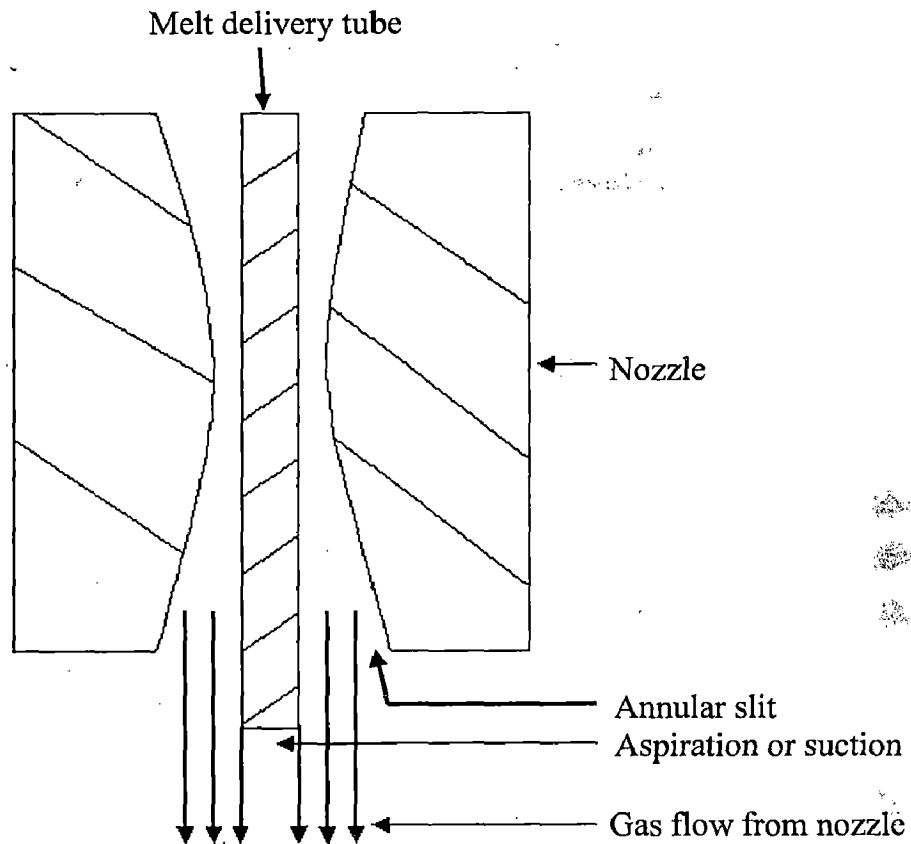


**Fig.6.1.** Schematic of gas flow from nozzle and aspiration at the exit of melt delivery tube.

Gas velocities calculated from this equation are compared with experimental values in **fig.6.2**. For the purpose of comparison a line is drawn at  $45^\circ$  from the x-axis. A value on this line represent that the calculated value exactly match with the experimental one. Gas velocities calculated from Equation 6.3 for the data reported by Bewlay et al. [50] and Moir et al. [82] are also shown in the same figure. It can be seen that this equation predicts reasonably satisfactory values of present study data except for some velocity points. But, most of the velocity points of other workers lie in above

region of the plot i.e. in calculated velocity side. It means that the gas velocity from present nozzle is higher than that of other workers. It can be due to the parallel flow of gas to the melt flow tube in present study whereas in conventional nozzle it flows at some angle from the melt delivery tube.

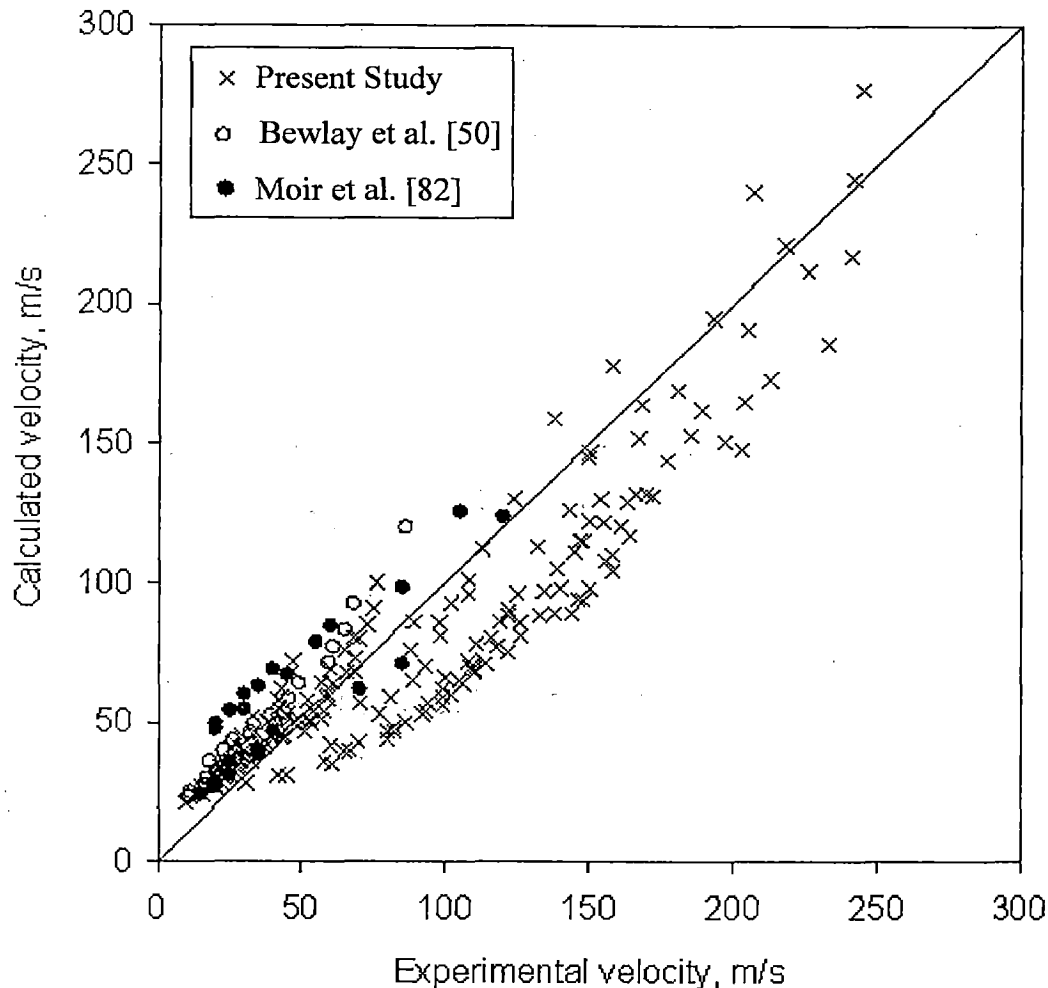


Fig.6.2. Comparison of calculated and experimental gas velocities.

### 6.1.2 Discharge coefficient

Gas flow rate through an atomizer of a given cross sectional area is an important parameter since it not only influences droplets and spray deposit properties but also the economic viability of the process [83]. The flow rate of the gas can be readily

determined by considering the flow to be isentropic i.e. reversible adiabatic. The maximum mass flow rate of gas passing through a nozzle of a given cross sectional area under isentropic flow condition is given by [80].

$$\dot{m}_A = AP \sqrt{\frac{\gamma M}{RT} \left( \frac{2}{\gamma + 1} \right)^{\frac{\gamma+1}{2(\gamma-1)}}} \quad (6.4)$$

Where,  $\dot{m}_A$  is the gas mass flow rate, A is throat area of nozzle, P is the plenum pressure, M molecular wt. of gas, T is the temperature of gas, R is universal gas constant and  $\gamma$  is the specific heat ratio.

The flow of gas in an atomizer does not follow the isentropic flow condition. The deviation from isentropic flow condition is caused by the atomizer design such as nozzle geometry, pressurizing manifold, total throat/slit area of nozzle etc. Therefore, a correction has to be applied in Equation 6.4 to take into account the effect of the aforementioned factors on the flow rate of gas. Discharge coefficient is one such factor and it is given by [80]:

$$C_D = \frac{\dot{m}_a}{\dot{m}_A} \quad (6.5)$$

Where,  $\dot{m}_a$  is the actual mass flow rate of gas passing through the atomizer. In the experiments volume flow rate of air passing through the atomizer is measured as a function of plenum pressure. The volume flow rate is converted into mass flow rate by taking density of air as 1.18 Kg/m<sup>3</sup> (at 25°C and 1 atm.). The value of  $\dot{m}_A$  is determined by Equation 6.4 using the value of physical constants. The discharge coefficient is calculated by Equation 6.5 and is shown in **fig.6.3** as a function of plenum pressure. A best fit line is determined for the data shown in this figure and it is found that the slope of this line is negligible according to t-test. Therefore, a horizontal best fit line is drawn corresponding to a value of 0.86 of the discharge coefficient.

Singh et al. [52] and Moir et al. [82] have measured the gas flow rate  $\dot{m}$  through free fall atomizers as a function of plenum pressure. From their data gas flow rate was calculated at various plenum pressures using Equation 6.4 while  $C_D$  was determined by

using Equation 6.5. The values of  $C_D$  are given in **table 6.1**. It was seen that the discharge coefficient of the atomizer in the present study and that of Singh et al. and Moir et al. is almost independent of plenum pressure. The value of discharge coefficient of present nozzle is higher as compared to that of other workers which may be due to the difference in the nozzle design.

**Table 6.1** Gas discharge coefficient  $C_D$  of atomizer with given experimental parameters.

Atomizer	Nozzle type	Gas	$\rho_g$ , kg/m <sup>3</sup>	P, kPa	$C_D$	Reference
Free fall	Discrete	Air	1.182	700-1900	$0.825 \pm 0.025$	<b>Singh et.al. [52]</b>
Free fall	-do-	Air	1.182	700-1900	$0.575 \pm 0.025$	<b>Singh et al. [52]</b>
Free fall	-do-	Air	1.182	700-1500	$0.560 \pm 0.010$	<b>Singh et al. [52]</b>
Free fall	-do-	N <sub>2</sub>	1.141	690-1380	$0.635 \pm 0.015$	<b>Moir et.al. [82]</b>
Confined	Annular slit	Air	1.182	300-1200	$0.860 \pm 0.031$	<b>Present Study</b>

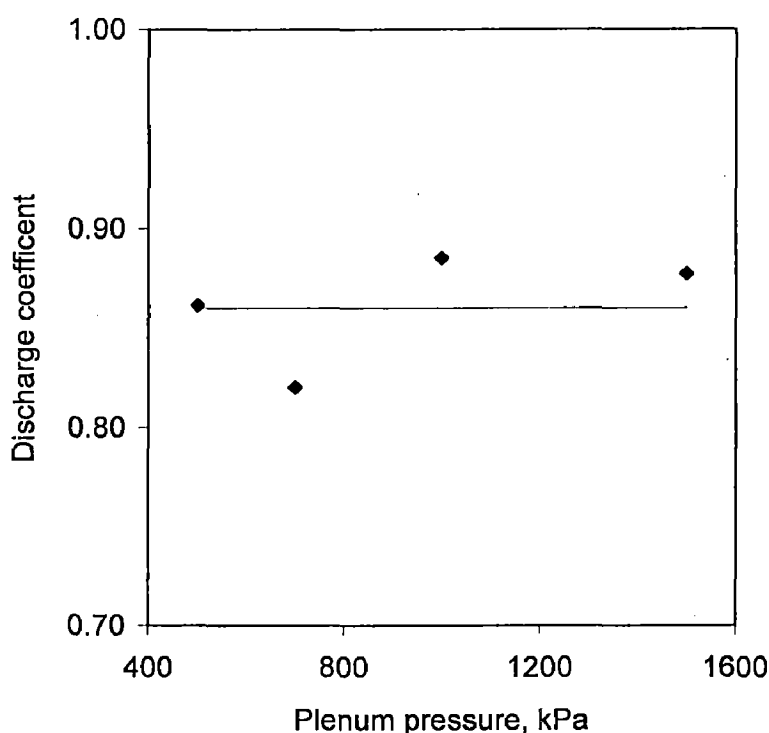


**Fig.6.3** Variation of gas discharge coefficient with plenum pressure.

## 6.2 THICKNESS UNIFORMITY OF THE DEPOSIT

Mass flux of the droplets varies from centre to periphery of the spray cone and hence the spray deposit or preform can not have a uniform thickness. The variation in preform thickness needs to be determined before further study of its physical and mechanical properties because this thickness variation will affect these properties. Heat transfer, porosity, microstructure, hardness, strength, wear rate etc. of the spray deposit will change with the variation in thickness of the deposit. Therefore, study of aforementioned parameters can produce misleading values without reporting the thickness uniformity or thickness variation of the deposit. In present study inclination angle, offset distance and distance of substrate from the atomizer were observed to affect the thickness uniformity of the spray deposit or preform.

### 6.2.1 Effect of inclination angle

At  $0^\circ$  inclination angle of the substrate from horizontal plane and without its offsetting, the deposition or substrate area per unit change in radius of the substrate increases with the increase in radius of the substrate i.e.

If

$$A_s = \pi r_s^2 \quad (6.6)$$

Then,

$$\frac{dA_s}{dr_s} = 2\pi r_s \quad (6.7)$$

Therefore, the mass distribution of particles/ droplets in spray cone should also increase in same proportion to get a deposit of uniform thickness. But, unfortunately this mass decreases instead of increasing as given by the following Gaussian distribution [25-29] function.

$$\dot{m} = \dot{m}_{\max} \exp(-a r^K) \quad (6.8)$$

Where,  $\dot{m}_{\max}$  is the maximum mass flux in the spray cone,  $K$  ( $=1.4$ ) is a constant and  $a$  is a radial distribution coefficient given by

$$\alpha = \ln 2 \left( \frac{1}{r_{0.50}} \right)^K \quad (6.9)$$

Where,  $r_{0.5}$  is the half width of the spray cone.

From Equations (6.8) and (6.9)

$$\dot{m} = \dot{m}_{\max} \exp \left[ -\ln 2 \left( \frac{r}{r_{0.50}} \right)^K \right] \quad (6.10)$$

Therefore, at  $0^\circ$  inclination angle it is impossible to produce a deposit of uniform thickness.

At an inclination angle ' $\theta$ ' of the substrate the  $\dot{m}_{\max}$  will shift continuously towards periphery of the deposit with the increase in its thickness i.e. more mass is shifted towards periphery and hence inclination of the substrate increases the thickness uniformity of the deposit.

The thickness uniformity with the increase in inclination angle will also increase due to the distribution of same mass of particles over more area of the inclined surface in the same spray cone as shown in **fig.6.4**. Mathematically, the mass distribution of the spray cone along the tilted substrate can be given by the Equation (6.10) in a modified form as explained below.

The radius of depositing mass will be distributed from  $r_1$  to  $r_2$  on the substrate surface and hence mass distribution will also vary from  $\dot{m}_1$  to  $\dot{m}_2$  given by the following equations:-

$$\dot{m}_1 = \dot{m}_{\max} \exp \left[ -\ln 2 \left( \frac{r_1}{r_{0.50}} \right)^K \right] \quad (6.11)$$

and

$$\dot{m}_2 = \dot{m}_{\max} \exp \left[ -\ln 2 \left( \frac{r_2}{r_{0.50}} \right)^K \right] \quad (6.12)$$

Where  $r_1$  and  $r_2$  are given by following expressions (derived in appendix A)

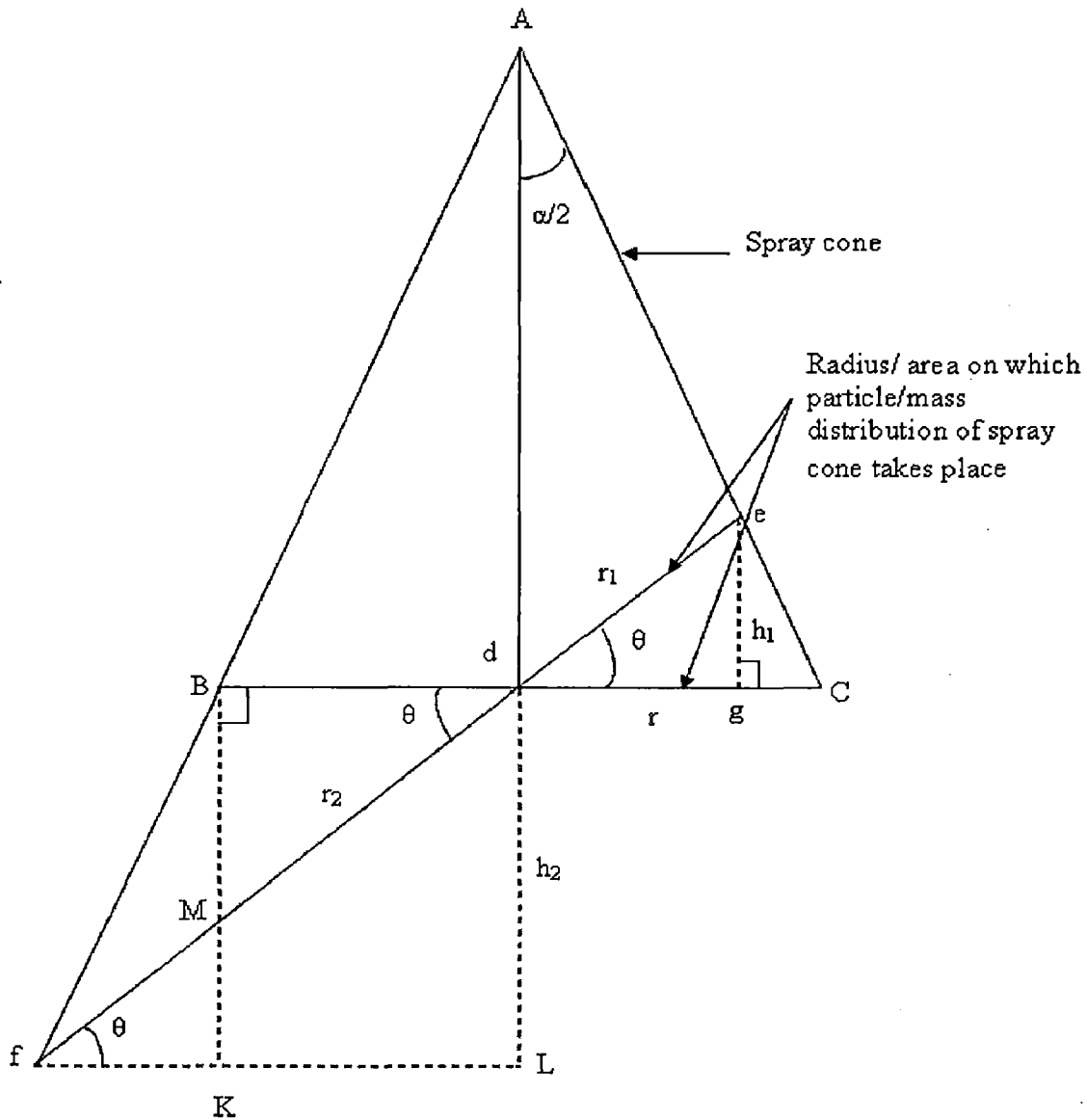


**Fig.6.4** Schematic to show the radius/area on which particle/mass distribution of spray cone takes place after tilting substrate an angle ' $\theta$ '.

$$r_1 = \frac{r}{\cos \theta + \sin \theta \tan \alpha / 2} \tag{6.13}$$

and

$$r_2 = \frac{r}{\cos \theta - \sin \theta \tan \alpha / 2} \tag{6.14}$$

With every rotation of substrate, the mass deposition rate on every point of substrate will vary from  $\dot{m}_1$  to  $\dot{m}_2$ . So, effective or average deposition on every point of substrate is given by the following equation.

$$\dot{m}_\theta = \frac{\dot{m}_1 + \dot{m}_2}{2} = \frac{\dot{m}_{\max}}{2} \left[ \exp\left(-\ln 2 \left(\frac{r_1}{r_{0.50}}\right)^K\right) + \exp\left(-\ln 2 \left(\frac{r_2}{r_{0.50}}\right)^K\right) \right] \quad (6.15)$$

Fig.6.5 shows a plot between the ratio of mass deposition rate at inclination angle of  $30^\circ$  ( $\dot{m}_{30}$ ) to that of at  $0^\circ$  ( $\dot{m}_0$ ) and the ratio of spray cone radius ( $r$ ) to half width of spray cone ( $r_{0.50}$ ) for a spray cone angle of  $40^\circ$ . It can be seen that the mass

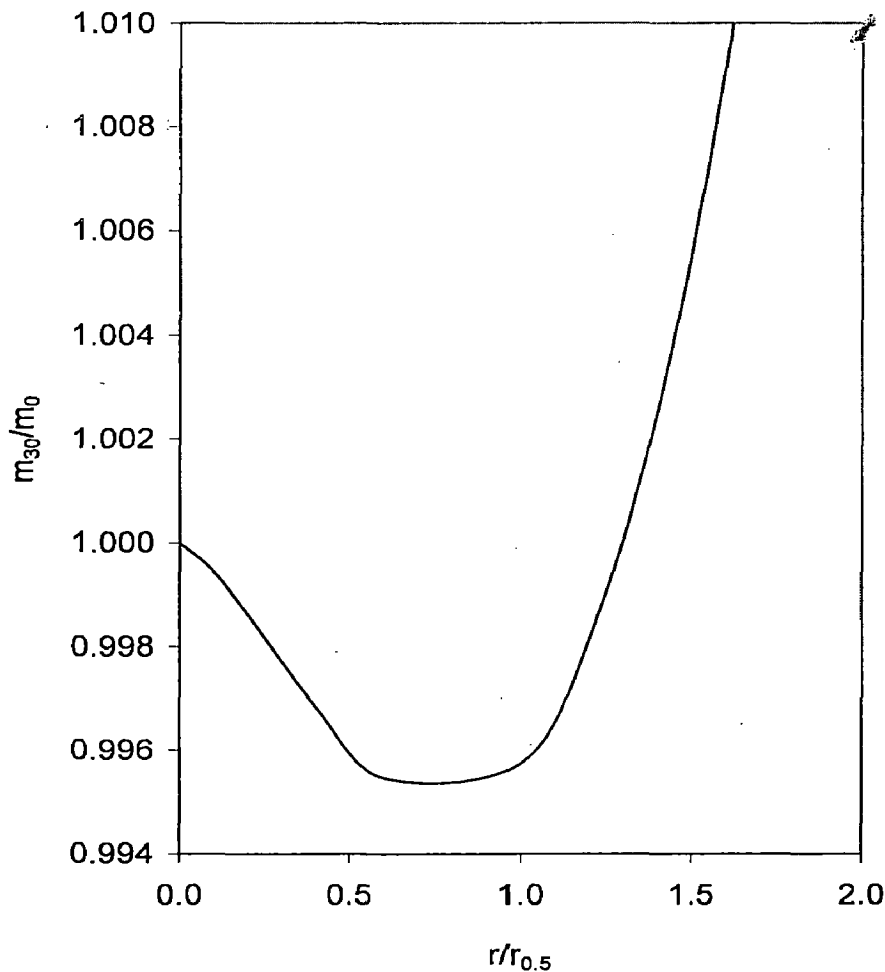


Fig.6.5 Ratio of mass flux at 30 deg inclination angle ( $m_{30}$ ) to mass flux rate at 0 deg angle ( $m_0$ ) with ratio of radius  $r/r_{0.5}$  of the spray cone.



in spray cone first decreases from centre to periphery and then it increases, which is required to increase the thickness uniformity. Therefore, the thickness uniformity was observed to increase in **fig. 5.10 (d), (e) and (f)** with the increase in inclination angle from 0 to 30°.

## 6.2.2 Effect of offset distance

The offsetting of substrate after its tilting can be in left or right side of the central axis (or atomizer axis) of the spray cone. Both the offsetting will have different effect on mass distribution of spray cone over the substrate surface. In present study substrate was tilted anticlockwise and moved in the right side. To understand the effect of offsetting on thickness uniformity of the deposit, no tilting is assumed for the simplicity. Therefore, for horizontal substrate with an offset distance 's' as shown in **fig.6.6**, the mass distribution of droplets in spray cone on the substrate in left and right of its centre can be given by the following equations which are derived from equation (6.10).

In right hand side the equation is

$$\dot{m}_3 = \dot{m}_{\max} \exp \left[ -\ln 2 \left( \frac{r+s}{r_{0.50}} \right)^K \right] \quad (6.16)$$

and in left hand side the equations are

$$\dot{m}_4 = \dot{m}_{\max} \exp \left[ -\ln 2 \left( \frac{s-r}{r_{0.50}} \right)^K \right] \quad \text{for } 0 \leq r \leq s \quad (6.17)$$

$$\dot{m}_5 = \dot{m}_{\max} \exp \left[ -\ln 2 \left( \frac{r-s}{r_{0.50}} \right)^K \right] \quad \text{for } r \geq s \quad (6.18)$$

With every rotation of substrate, the mass deposition rate on every point of substrate will vary from  $\dot{m}_3$  to  $\dot{m}_4$  for  $0 \leq r \leq s$  and  $\dot{m}_3$  to  $\dot{m}_5$  for  $r \geq s$ . Therefore, there will be two regions on the substrate having mass deposition given by the following equations.

$$\dot{m}_{s1} = \frac{\dot{m}_3 + \dot{m}_4}{2} = \frac{\dot{m}_{\max}}{2} \left[ \exp\left(-\ln 2 \left(\frac{r+s}{r_{0.50}}\right)^k\right) + \exp\left(-\ln 2 \left(\frac{s-r}{r_{0.50}}\right)^k\right) \right] \quad \text{for } 0 \leq r \leq s \quad (6.19)$$

and

$$\dot{m}_{s2} = \frac{\dot{m}_3 + \dot{m}_5}{2} = \frac{\dot{m}_{\max}}{2} \left[ \exp\left(-\ln 2 \left(\frac{r+s}{r_{0.50}}\right)^k\right) + \exp\left(-\ln 2 \left(\frac{r-s}{r_{0.50}}\right)^k\right) \right] \quad \text{for } r \geq s \quad (6.20)$$

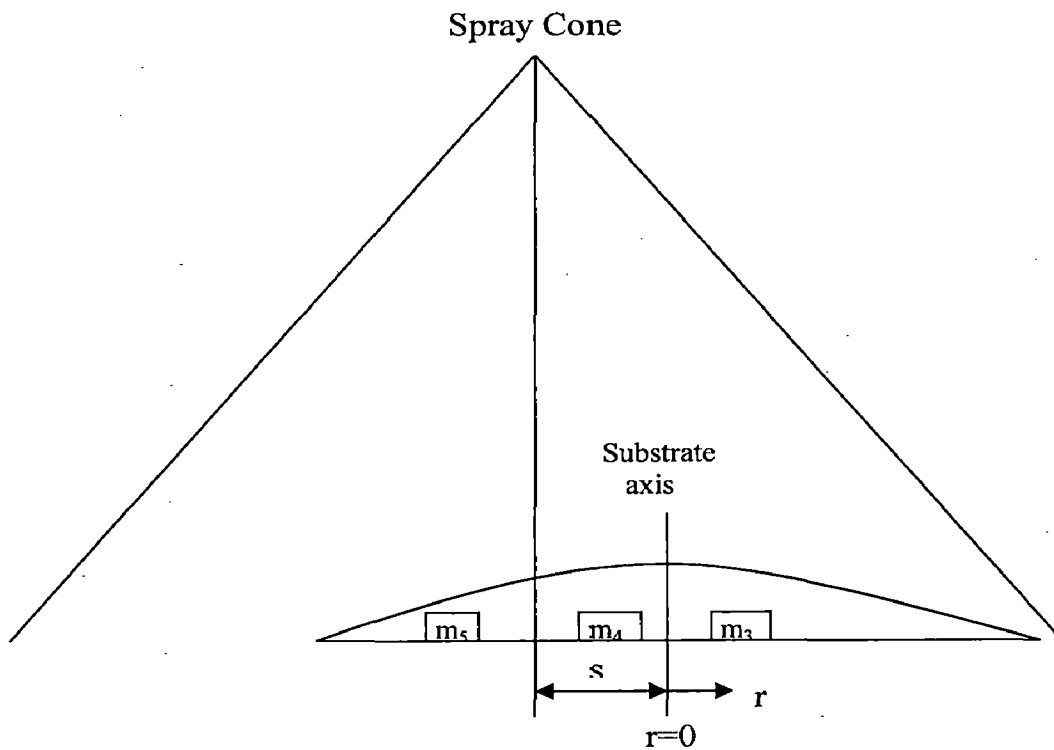


**Fig.6.6** Schematic to represent the mass distribution about substrate axis with an offset distance 's' from spray cone axis.

Fig.6.7 shows a plot between the ratio of mass deposition rate at an offset distance of 40 mm ( $\dot{m}_{40}$ ) to that of maximum mass flux and the ratio of spray cone radius ( $r$ ) to half width of spray cone ( $r_{0.50}$ ). It can be seen that the mass on substrate in the spray cone first decreases up to 's' from cone centre to periphery and then it increases as compared to that of without offsetting, which is required to increase the thickness uniformity. Therefore, by offsetting the substrate from 0 to 40 mm a more uniform deposit in thickness was produced as shown by comparing the deposit shape in fig. 5.10 (b) and (d). In fig. 6.7 it can also be seen that the shape generated theoretically from the above explained model is similar to that of the produced experimentally in fig.5.10.

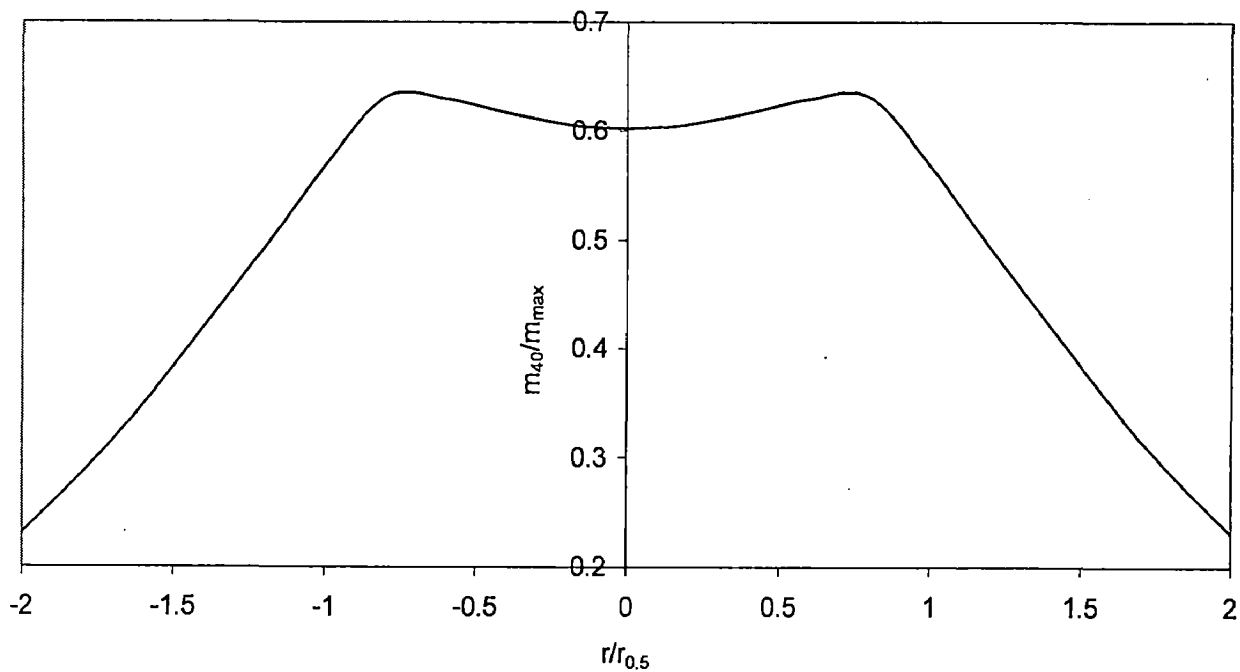


Fig.6.7 Variation of mass distribution in spray cone on the substrate with an offset distance of 40 mm

### 6.2.3 Effect of substrate distance

Mass flux distribution in spray cone is given by [25] the following equation

$$\dot{m}(r, h) = \dot{m}_{\max_0} \left( \frac{h_0}{h} \right)^2 \exp \left[ -a_0 \left( \frac{h_0}{h} \right)^K \cdot r^K \right] \quad (6.21)$$

Where,  $\dot{m}_{\max_0}$  is the maximum mass flux in spray cone at distance  $h_0$  and  $a_0$  is the radial distribution coefficient at distance  $h_0$ , which is given by

$$a_0 = \ln 2 \left( \frac{1}{r_{0.50}} \right)^K \quad (6.22)$$

From Equations (6.21) and (6.22) for  $K=1.4$  the following equation can be obtained.

$$\frac{\dot{m}(r, h)}{\dot{m}_{\max_0}} = \left( \frac{h_0}{h} \right)^2 \exp \left[ -0.693 \left( \frac{r}{r_{0.50}} \cdot \frac{h_0}{h} \right)^{1.4} \right] \quad (6.23)$$

A plot of above Equation (6.23) in terms of dimensionless terms  $\dot{m}(r, h) / \dot{m}_{\max_0}$  versus  $r/r_{0.50}$  for different values of  $h/h_0$  is shown in fig.6.8. It can be

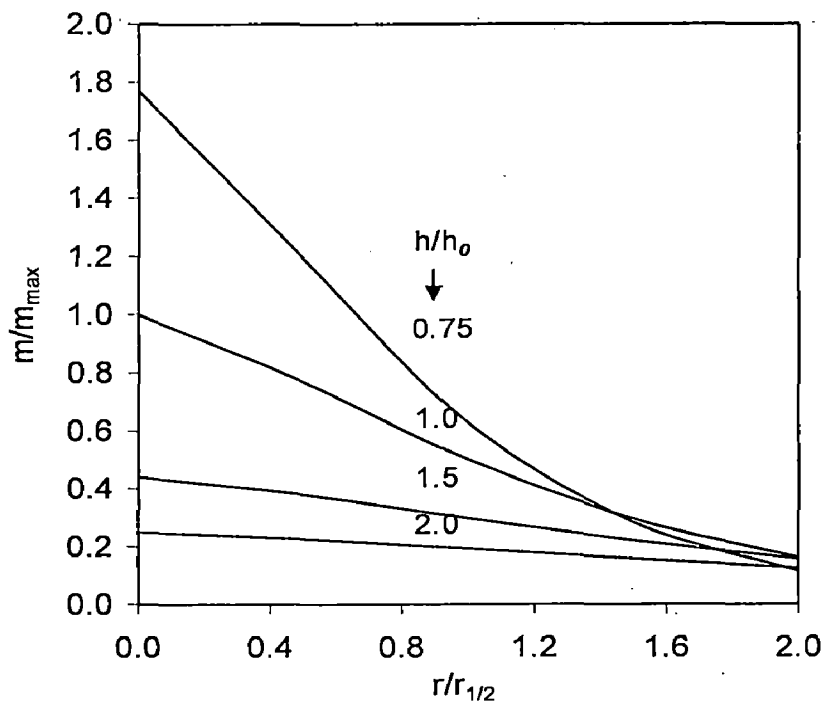


**Fig.6.8** Variation of spray cone mass with spray cone radius for different values of deposition distance

was no silicon. It could be due to large density difference between aluminum and lead as compared to that of aluminum and silicon.

The solidification shrinkage on particles (**fig.5.19**) shows that the surface of droplets should solidify at the end of droplet solidification, so that no liquid will be present to fill the shrinkage and cavity [85].

Droplets move in very high gas velocity which causes under cooling of the melts. This under cooling leads to the formation of dendrites in particles. The solidification rate of these particles can be determined from the microstructure of their cross-section (**fig.5.20**). As dendritic arm spacing is 2 to 3  $\mu\text{m}$ . So, using the empirical relationship  $\lambda = B (dT / dt)^{-n}$  where B and n are constants, the solidification rate is of the order of  $10^3$ -  $10^4$  K/s. The values of B and n are taken as 47 and 0.33 as reported by Jones [88] to get cooling rate (dT / dt) in K/s.

The porosity inside the particles can be due to solidification shrinkage and entrapment of atomizing gas.

### 6.3.2 In spray deposit

Atomized droplets in liquid, semi-solid and fully solid state deposit over the substrate kept at a distance of 450 mm. At this distance the maximum velocity of gas is 50 m/s (from Equation 6.3). This velocity is not supposed to disintegrate further the droplets [89] or melt depositing on the substrate. However, the impact of the momentum of droplets striking the deposit can break some melts further on the deposit. The impact of this momentum also leads breaking of semi-solid droplets into finer fragments on the deposition surface. These fine fragments act as nuclei for the solidification of melt on the surface [27].

A semi-solid or semi-liquid mass is continuously depositing and solidifying on the deposition surface. This continuously depositing mass will release heat rapidly to the surroundings having high gas velocity, and already / previously deposited mass. The high gas velocity leads to high rate of heat transfer by convection and previously deposited mass leads to heat transfer by conduction from the depositing mass.

Therefore, the formation of nuclei and high rate of heat transfer from the melt leads to very high solidification rate of the spray deposit and thereby formation of equiaxed structure (**figs.5.21 to 5.26**). The silicon in the structure is in particulate form,

contrary to that of the convective cast structure [78,90,91]. It also indicates rapid solidification of the deposit [78].

Molten lead will diffuse towards the liquid present in the deposit during solidification of the Al-rich deposit. Therefore, molten lead diffuses towards the grain boundary of aluminum and accumulates over there in small droplets (fig.5.26). More amount of lead in aluminum rich melt means more accumulation of lead at the grain boundaries (figs.5.22 to 5.26). The shape of these lead droplets will depend on their spherodization time and the solidification time of Al-rich melt. If Al-rich melt solidify after the spherodization time of lead, the lead droplet will be spherical (figs.5.22, 5.23 and 5.26(a) & (b)) otherwise non-spherical (figs.5.24, 5.25 and 5.26(c) & (d)). The large size lead droplets will take more time to spherodize and hence these will remain non spherical. It was revealed in both optical and SEM micrographs.

Silicon will also diffuse to the grain boundary and solidify before solidification of the lead. Therefore, some silicon particles at grain boundaries were observed to be surrounded by lead.

The microstructure of the deposit was found to depend on the central and peripheral regions of the deposit (figs.5.21 to 5.25). The small thickness of the deposit at peripheral region leads to an increase in the heat transfer rate ( $\dot{Q} \propto dT/dx$ ) by conduction and hence more cooling rate at peripheral region as compared to that of the central region. The more cooling rate at peripheral region leads to the formation of more fine grains structure as compared to that of the central region.

Heat transfer from the deposit also takes place by convection in high gas velocity field. The difference in gas velocity at the centre and periphery is not very large (3.4 m/s from Equation 6.3). So, there will not be a significant difference in cooling rate by convection at the centre and periphery of the deposit.

No significant change in microstructure was observed at the bottom and top of the deposit, which indicate almost same solidification rate at these locations. Actually, the solidification rate can not vary along the thickness of the deposit under steady state condition i.e. when there is no change in substrate temperature with time and metal is depositing continuously on it. It can be understood as follows. A constant mass flow rate of droplets/ particles varying in radial direction (Equation 6.23) in the spray cone moves towards the substrate. The deposit grows in thickness direction with a constant

seen that the mass flux distribution ( $m$ ) uniformity with spray radius ( $r$ ) increases with the increase in spray distance ( $h$ ). This increase in thickness uniformity was observed in present study as shown in **fig.5.10 (a), (b) and (c)** with the increase in substrate distance from 400 to 500 mm. It has been observed that both tilting as well as offsetting of the substrate increases the thickness uniformity of the preform. Therefore, combination of both tilting and offsetting will give more uniform thickness of preform as observed in **fig. 5.10 (f)**

## 6.3 SOLIDIFICATION & MICROSTRUCTURE EVOLUTION

### 6.3.1 In Powder particles

Pb, Al and Si alloy melted in the crucible flow through the delivery tube into the energetic gas field of atomizer. Silicon is soluble in aluminum in molten state, so two liquids Al-Si rich and Pb rich are atomized by the gas. Consequently, two type of droplets (**figs.5.17 and 5.18**) viz. one with aluminum rich and other one with lead rich form in the spray. Cooling of these droplets takes place during their flight in gas stream. Some droplets solidify completely, some partially and some remain in liquid state before deposition on the substrate to form the spray deposit. Which droplet will be in which state depends on its size, shape and alloy composition.

If size and shape are similar Al-rich droplets will have more liquid content as compared to that of lead rich droplets before deposition on substrate. It is due to about two times the solidification time [39,61,62,64,69,71,84-87] of aluminum as compared to that of lead as shown below by Equation (6.24). The values of physical constants used are reported in **table 6.2**.

$$\frac{t_{sol,Al}}{t_{sol,Pb}} = \frac{[\rho \cdot \Delta H / (T_m - T_g)]_{Al}}{[\rho \cdot \Delta H / (T_m - T_g)]_{Pb}} = \frac{2700 \times 390000 / (933 - 298)}{11000 \times 23215 / (605 - 298)} = 1.994 \approx 2 \quad (6.24)$$

In lead rich droplet some lead can solidify even before the solidification of aluminum in it. This aluminum will keep lead in molten state which is just around it and lead away from this aluminum can solidify. Although, lead near the aluminum will solidify after solidification of the aluminum (as it has higher melting point). More

liquid in Al rich droplets implies more cracks in these droplets. The large size particles which do not solidify up to collection tray will show cracks [85].

**Table 6.2** Physical properties of Pb and Al [85]

Metals	T <sub>m</sub> (K)	ρ (Kg/m <sup>3</sup> )	μ (Pas)	σ (N/m)	C <sub>p</sub> (J/Kg-K)	ΔH (J/Kg)
Al	933	2700	0.0014	0.914	1100	390000
Pb	605	11000	0.0026	0.458	156	23215

The sphereodization time [65] of aluminum droplets is much lower than that of lead droplets as shown below by Equation (6.25). So, aluminum rich droplets should be more rounded than that of lead rich droplets for the same size. To support this theory, there were very small numbers of particles present in the powder sample of present study because particles of the same size need to be compared but there was a large difference between the sizes of aluminum rich and lead rich particles.

$$\frac{t_{sph,Al}}{t_{sph,Pb}} = \frac{(\mu/\sigma)_{Al}}{(\mu/\sigma)_{Pb}} = \frac{0.0014/0.914}{0.0026/0.458} = 0.27 \quad (6.25)$$

In present study Al rich particles were very coarser as compared to that of Pb rich (**figs.5.17** and **5.18**) which is supported by the following Equation [66].

$$\frac{X_{M,Al}}{X_{M,Pb}} = \sqrt{\frac{(\mu\sigma/\rho^2)_{Al}}{(\mu\sigma/\rho^2)_{Pb}}} = \sqrt{\frac{(0.0014 \times 0.914)/2700}{(0.0026 \times 0.458)/11000}} = 4.22 \quad (6.26)$$

Both lead and silicon are not soluble in solid aluminum. Therefore, during the solidification of aluminum rich droplets Pb and Si should come out from the droplets on their surface. Lead was seen (**figs.5.17** and **5.18**) on the droplets surface but there



rate. This deposition rate varies only in radial direction of the deposit which results in a non-uniform thickness of the deposit. It implies that the solidification rate should be constant in thickness direction and vary in radial direction. If solidification rate is not constant in thickness direction i.e. it is decreasing or increasing with the thickness, in that case one condition will arrive at which nothing or everything will solidify on top surface of the deposit. Both of these events are not occurring. Therefore, under steady state condition, solidification rate will not vary along the thickness of the deposit.

In the beginning, the substrate is at room temperature, and its temperature increases with the increases in deposit mass. So, in the beginning there is no steady state and hence up to the deposition thickness at which steady state is achieved, the solidification rate will vary. It will decrease with the increase in the deposit thickness up to the steady state condition. So, the grain size of bottom mass of the deposit should be finer to that of the top mass. But, it was not the case. It indicates same solidification rate at both the locations. Actually, the deposition stop after some time and solidification of the top surface also takes place under unsteady state condition (like bottom surface) in the high gas velocity. So, it can give rise to same solidification rate and hence same grain size.

Fig. 6.9 shows the average lead particle size as a function of lead content in the Al-Si-Pb alloy. The values of lead particles size reported by An J. et al. [2] for the cast Al-Si-Pb alloy are also shown in the same figure. It can be seen that their values and the data of the present study represent a straight line variation and the lead particle size increases with the increase in lead content. The aluminum grains are coarser in the cast alloy. In present study the size of aluminum grains is also higher at the centre as compared to that of the periphery of the deposit. Therefore, same figure also shows that the lead particles size increases with the increase in the size of aluminum grains.

The Porosity formation observed in all microstructures is discussed in the subsequent section.

## 6.4. POROSITY FORMATION

The porosity formation can take place due to the gas entrapment, insufficient melt to fill porosity, dissolved gas evolution and solidification shrinkage. All these factors are explained for some metals or alloy systems in the literature [47,48,92]. In present study

some interesting features observed on porosity formation were the decrease in porosity from centre to periphery of the deposit (**fig.5.12**) and the increase in porosity with the increase in lead content (**fig.5.13**). The other feature was more porosity around the lead particles.

The decrease in porosity from centre to periphery can be explained as follows. There can be two reasons. First, the grain size decreases from centre to periphery as explained above in section 6.3. The decrease in grain size of aluminum also decreases the grain size of lead droplets (**figs.5.22 to 5.25**). These fine lead droplets pushed into the interstitial voids generated due to the solidification of Al-rich phase and thereby decrease the porosity of the deposit. That is why the porosity also decreases at higher rate with the increase in lead content. The second reason could be the decrease in gas velocity from centre to periphery of the deposit (Equation 6.3). High gas velocity at the centre can lead to more entrapment of the gas in the deposit as compared to that of the periphery (**fig.5.14**) and hence more porosity formation at the centre of the deposit. The decrease in porosity with the distance from centre to periphery was observed to decrease at a faster rate in the initial stage and then at a slow rate. The gas velocity Equation (6.3) also shows similar trend for decay in velocity with radial distance. Therefore, gas entrapment could be a major reason for the decay in porosity with distance from centre to periphery of the deposit. In contrast to the decay in porosity from centre to periphery of the present study, Sahu et al. [48] have shown an increase in the porosity of the commercially pure aluminum spray formed strip but the reason for it is not reported.

Surface tension of aluminum decreases [93] by increasing the lead content and hence the flow of aluminum should take place easily. The easy flow of aluminum should decrease the porosity of preform. But it was found that porosity increases by increasing lead content. The increase in porosity with increase in lead content (**fig.5.15**) can be due to the difference in solidification shrinkage of aluminum and lead. The solidification shrinkage of lead is higher than that of aluminum. In the deposit lead solidifies after the solidification of aluminum rich phase, so there can be formation of shrinkage cavity around lead particles. Also, by increasing the lead content, the fraction of melt (as Pb) increases on the deposition surface. More melt will give rise to more solidification shrinkage porosity.

There can be significant dissolution of hydrogen in the Al-Si-Pb alloy. This hydrogen comes from the humidity and it can dissolve mainly in aluminum because in lead its solubility is very low [48]. Therefore, the decrease in lead content should decrease the porosity but the reverse is true in the present study. Hence, the prior reason of solidification shrinkage explained above dominates over this factor of gas dissolution.

The lower rate of increase in porosity at periphery as compared to centre of the deposit with the increase in lead content can be explained as follows. The droplets or particles depositing at periphery will travel more distance and also with low velocity in the low gas velocity field as compared to that of at centre of the deposit. Therefore, temperature of these droplets should be lower than that of at the centre of the deposit. It should be noted that lead will be in molten state at both the locations because aluminum will keep it in molten state. So, the lead in droplets at the periphery will solidify from a lower temperature as compared to that of at the centre of the deposit and hence lesser solidification shrinkage at the periphery. Less solidification shrinkage leads to less rate of porosity increase at periphery as compared to that of at

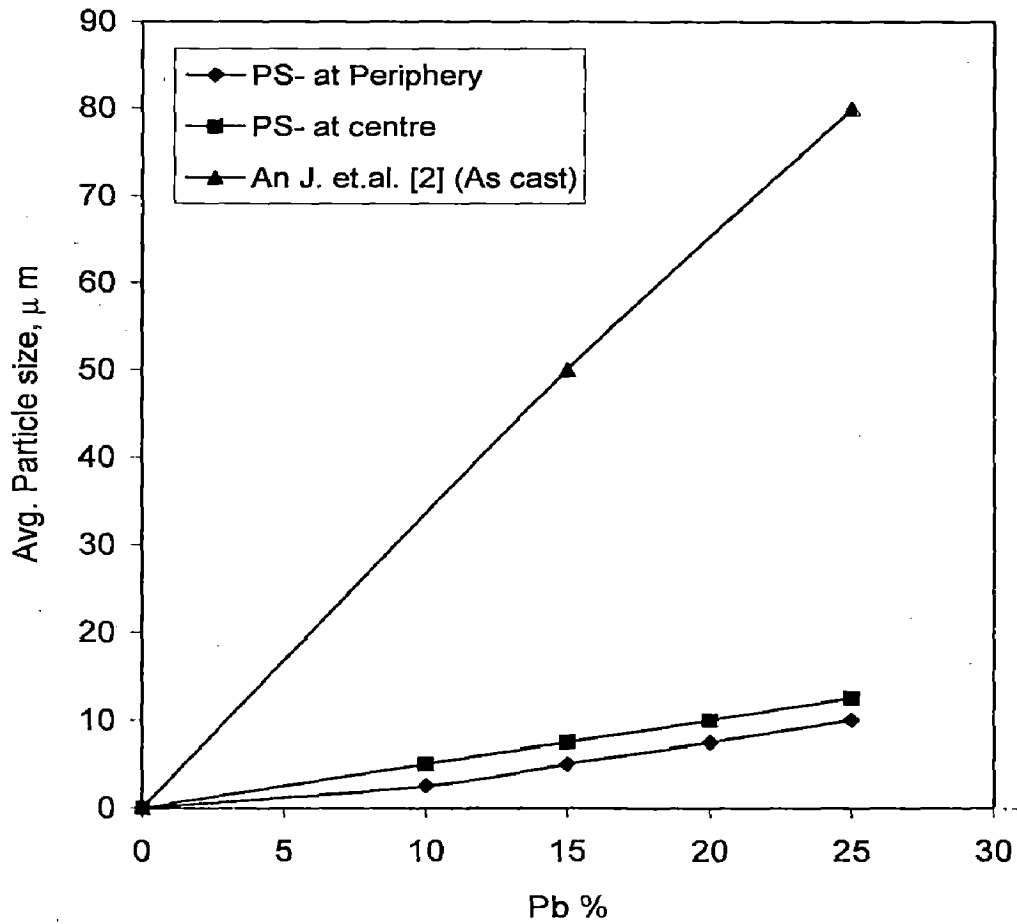


Fig.6.9 Average lead particle size as a function of lead content in Al-Si-Pb alloy

## 6.5 HARDNESS CHARACTERISTICS

Hardness of the Al-Si-Pb alloy preform was recorded as a function of lead content, distance from centre to periphery and height i.e. distance from top to bottom of the preform for 6 and 12 % silicon content. Preform height was not observed to have any significant effect on hardness. Although, grains are finer at the top and bottom surface as compared to that of the middle part of the preform. It means that the grain size has no effect on hardness. To study the effect of other two parameters viz lead content and distance from centre to periphery of the preform, a factorial design analysis [94] was conducted which is as follows. The design matrix of these two variables is given in table 6.3.

**Table 6.3** Design matrix for hardness study

Pb	$R_s$
-	-
+	-
-	+
+	+

*Note: Pb = % Pb,  $R_s$  = distance from centre to periphery of the preform.*

Values of required parameters for this design matrix are given below in table 6.4

**Table 6.4** Values of various parameters according to design matrix

Pb	$R_s$	Hardness
0	0	47
25	0	33
0	90	54.8
25	90	37.8

The calculated effects of both the parameters on hardness are given below in **table 6.5**.

**Table 6.5** Effects of various parameters on hardness

Parameters	Effects
Pb	-16
R	6
Pb.R	-3

From above table it can be seen that the effect of lead content on hardness is much higher as compared to that of the distance from centre to periphery of the deposit. Negative sign indicates that hardness decreases by increasing the lead content. Both, porosity and grain size change with the distance from centre to periphery of the deposit. Therefore, a small effect of the distance on hardness means that both porosity and grain size or any one of them has small effect on the hardness. But, it was seen (**fig.5.31**) that there is no effect of grain size on the hardness. Hence, the increase in hardness with the increase in distance from centre to periphery of the preform is due to the decrease in porosity of the deposit (**fig.5.30**) i.e. decrease in grain size with radial distance has no impact on hardness. The interaction value of Pb and  $R_s$  is very small = -3), therefore effect of Pb is almost same whatever be the distance  $R_s$ .

Finally, it can be concluded that porosity has effect on hardness whereas grain size has no effect. Therefore, the decrease in hardness with the increase in lead content (**fig.5.29**) is attributed to the increase in soft phase (Pb rich) and the increase in porosity with the increase in lead content.

## 6.6 PREFORM STRENGTH AND ELONGATION

Lead particles act as inclusion in Al-Si matrix [11,95]. Therefore, as the size of lead particles increase their influence on stress and elongation to fracture increases. In present study the size of lead particles increases by increasing the lead content and as lead is a soft phase compared to Al-Si matrix, therefore addition of lead in Al-Si-Pb

alloys decreases the proof stress and UTS (**fig 5.34**). With the increase in lead content the UTS decreases at a faster rate as compared to that of proof stress and it seems that at some particular lead content both will become equal i.e. there will be no strain hardening. In other words the ductility will become zero and alloy will behave as a brittle material i.e. the ductility of Al-Si-Pb alloy decreases with the increase in lead content (**fig. 5.35**).

It has been observed that the porosity of Al-Si-Pb alloy increases with the increase in lead content. Therefore, in addition to the above mentioned points, the increase in porosity with the increase in lead content will also contribute in the decay of alloy strength.

The grain size, porosity and lead particle size decrease with the distance from centre to periphery of the deposit. All these factors are responsible for the increase in stress and elongation to fracture with the increase in distance from centre to periphery of the deposit. The higher strength for 12 % Si as compared to that of 6 % Si is due to the high hardness of Si phase over Aluminum [96].

**Fig. 6.10** shows the ultimate tensile strength (UTS) and proof stress (FS) as a function of porosity of Al-6Si-Pb alloy at the centre of the deposit. It can be observed that both the strengths are well correlated by the following equations:

$$\ln(UTS) = -0.036 (Porosity) + 5.17 \quad (6.27)$$

and

$$\ln(UTS) = -0.019 (Porosity) + 4.60 \quad (6.28)$$

**Fig. 6.11** shows that the elongation to fracture can be correlated with the porosity by the following equation:

$$\ln(\%elongation) = -0.06(Porosity) + 1.45 \quad (6.29)$$

Equation 6.27 to 6.29 represents exponential decay in UTS, FS and % elongation with the increase in porosity of the spray deposit.

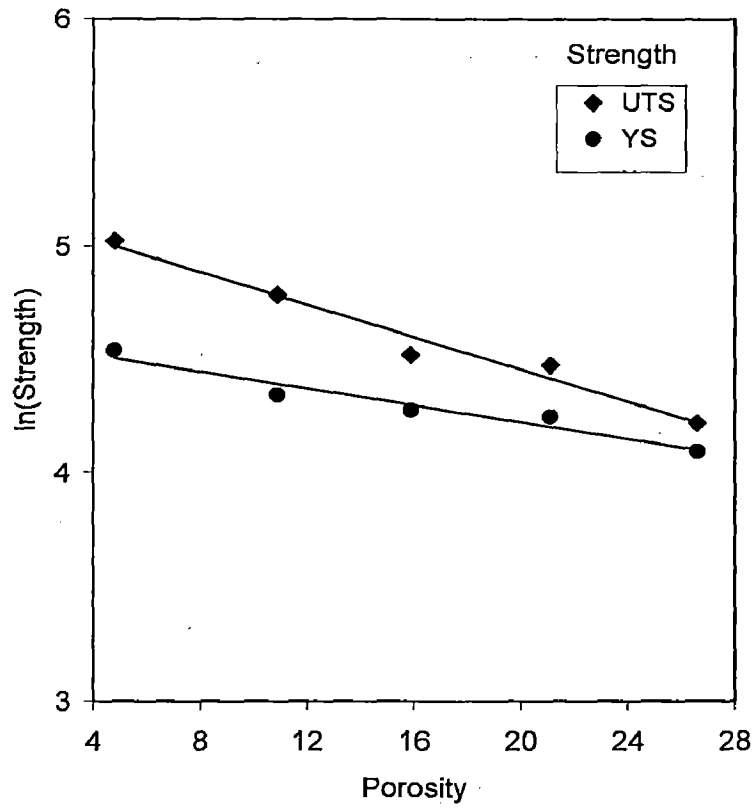


Fig. 6.10 Variation in strength with porosity at the centre of spray deposit.

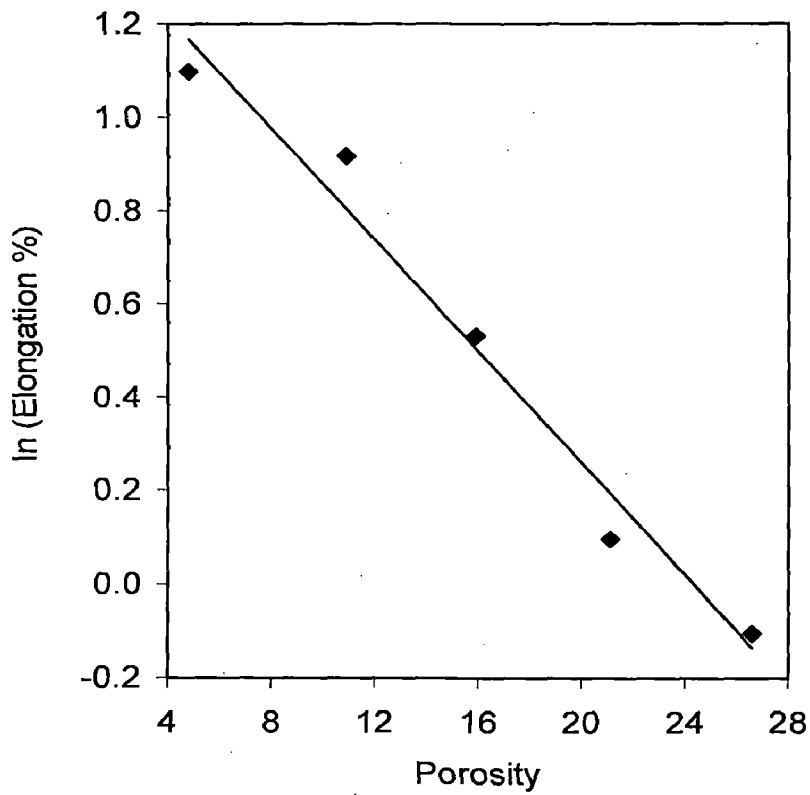


Fig. 6.11 Variation in elongation to fracture with porosity at centre of the spray deposit.



Fig. 6.12 shows that the ultimate tensile strength and proof stress can be correlated with the hardness of the deposit by the following equation.

$$UTS = 6.0(Hardness) - 135 \quad (6.30)$$

and

$$FS = 2.3(Hardness) - 18 \quad (6.31)$$

Equation 6.30 and 6.31 represents a linear increase in UTS and FS with the increase in hardness. Bocchini [97] also reported exponential decay in UTS, YS and % elongation with the increase in porosity for sintered alloys. A linear relationship (like equations 6.30 and 6.31) between UTS and FS with porosity was also reported. All the above equations represents similar trends in mechanical properties as reported by other workers [97,98] for sintered alloys.

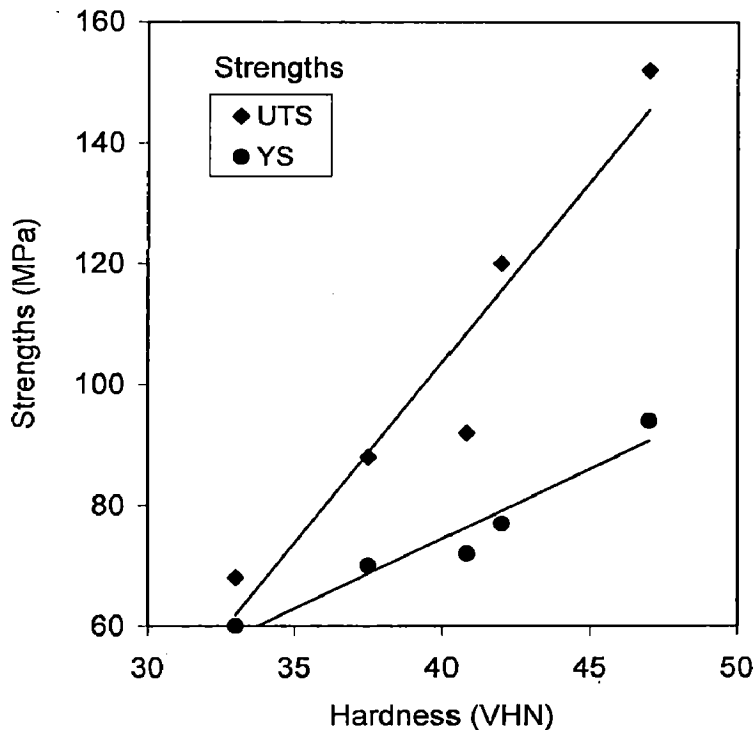


Fig. 6.12 Variation in strengths with hardness at centre of the spray deposit.

## 6.7 WEAR CHARACTERISTICS

### 6.7.1 Wear Rate

Under an applied load the relative movement of the test pin with respect to a metallic surface causes its wear and the friction between mating surfaces increases temperature of the test pin. The increase in temperature causes the oxidation of the test pin alloy. Therefore, at a lower applied load (10 to 30 N) only oxidative wear of test pin takes place. Oxides present in debris particles conforms it (**fig.5.45**).

Wear rate versus load variation (**fig 5.38**) can be divided into three regions having three different rate of increase in wear rate with the increase in applied load. In first region (at low load) formation of a white film grow over the test pin with the increase in applied load (**fig. 5.44 (a) and (b)**). Wear rate increases in this region linearly with the increase in applied load because more and more white film is available to wear with the increase in load.

In second region, there is damage to the white film as load is increased further (**fig. 5.44 (c)**). It means that the film formation area is decaying with the increase in applied load and hence there is no more and more white film available to wear with the increase in applied load. Therefore, the rate of increase in wear rate has decreased in this region as compared to that of the first region.

In third region, deep black groove and more damage to white film appears with the increase in applied load (**fig. 5.44(d)**). The rate of increase of the wear rate (with the increase in applied load) is higher than that of other two regions. It is due to the starting of metallic wear as revealed by XRD analysis of the debris (**fig. 5.45(b)**).

Lead in the test pin alloy causes formation of the white film over the test pin surface and hence for high lead content i.e. 20 and 25% the rate of increase in wear rate start decreasing at higher load (40 N in present study) as compared to that of (30 N in present study) the lower lead content i.e. 0 to 15 %.

The film formations over the test pin due to lead in test pin alloy acts as a lubricant and hence the wear rate decreases as lead content increases (**fig. 5.39**) in Al-Si-Pb alloys. It has been explained in previous section 6.4 that the porosity increases with the increase in lead content. The porosity increases the wear rate [99-101]. It

means that lead has more effect on wear rate as compared to that of the porosity, which finally resulting a decrease in the wear rate with an increase in the lead content.

The decrease in wear rate with the increase in distance from centre to periphery (fig. 5.40) of the preform is due to the decrease in porosity with the increase in distance from centre to periphery (fig. 5.12) of the preform. The decrease in wear rate with the increase in Si content is of course due to the increase in this harder phase.

To quantify the effect of three parameters viz applied load on test pin, its lead content and distance from centre to periphery of the preform, a factorial design analysis [94] was conducted which is as follows. The design matrix of these three variables is as given in table 6.6.

**Table 6.6** Design matrix for wear study.

Load	Pb %	R <sub>s</sub>
-	-	-
-	-	+
-	+	-
+	-	-
-	+	+
+	-	+
+	+	-
+	+	+

Values of the required parameters for this design matrix are given below in table 6.7

**Table 6.7** Values of various parameters as per design matrix.

load	Pb %	R <sub>s</sub>	wear rate
10	0	10	21
10	0	90	12
10	25	10	11
80	0	10	65
10	25	90	3
80	0	90	57
80	25	10	52
80	25	90	44

The calculated effect of both the parameters on hardness is given below in **table 6.8**.

**Table 6.8** Effects of various parameters on wear rate.

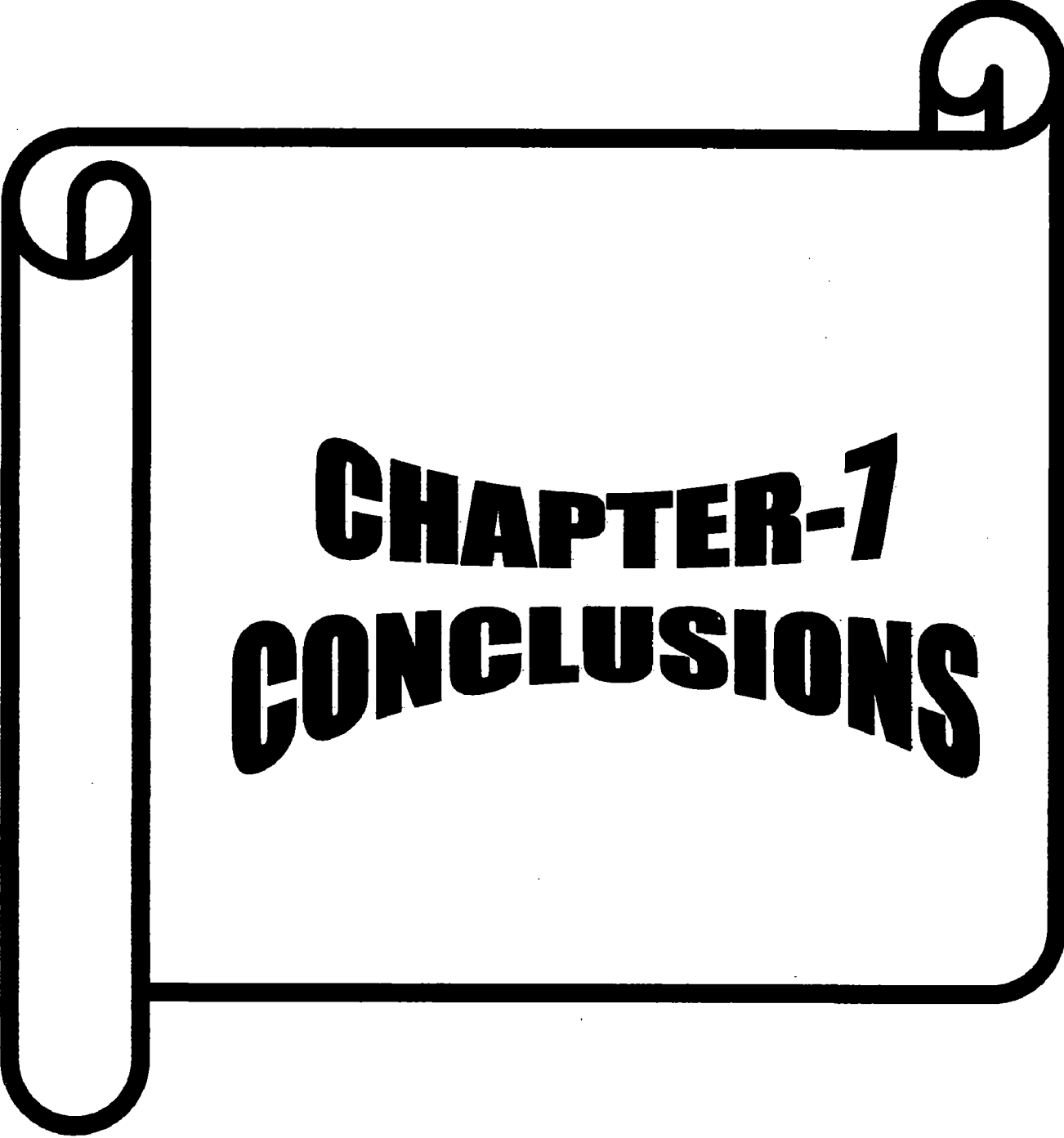
Parameters	Effects
Load	85.5
Pb %	- 22.5
R	- 16.5

From above table it can be seen that the effect of distance on wear rate from centre to periphery of the preform is a little bit lower to that of lead content. As porosity decreases from centre to periphery of the preform therefore it can be concluded that the wear rate decreases with the decrease in porosity [99-101]. The value calculated for its effect (-16.5) shows that the effect of porosity can not be neglected for the spray

deposit. Value calculated for the effect of applied load indicated that load has much higher effect on wear rate as compared to that of lead content or distance from centre to periphery of the spray deposit.

### **6.7.2 Coefficient of friction**

The coefficient of friction decreases very rapidly in the initial stage (up to a load of 40 N) and then it becomes almost constant. This decay in coefficient of friction is due to the formation of a white film of lead and the growth of this film increases up to 40 N which causes the decay in coefficient of friction up to this load. Beyond this load metallic wear starts and there is no growth of this film, therefore coefficient of friction remains constant.



**CHAPTER-7**  
**CONCLUSIONS**

# CONCLUSIONS

---

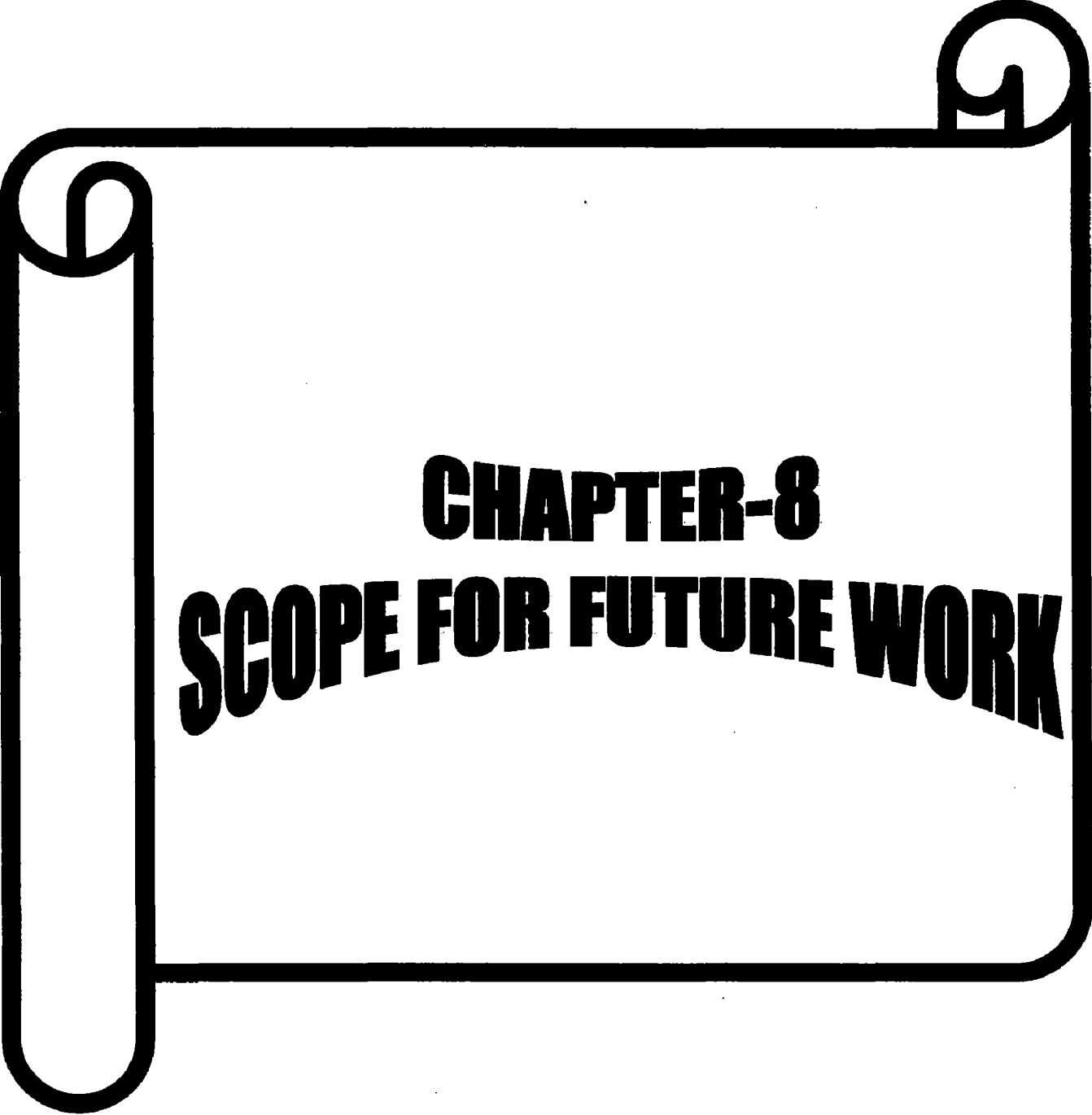
1. Gas velocity in the gas field of an atomizer decreases more rapidly with the increase in axial distance as compared to that of the radial distance.
2. A mathematical correction was derived to determine the gas velocity at any location in the gas field of the atomizer.
3. The gas velocity from the present atomizer was observed to be higher than that of the conventional atomizer.
4. The discharge coefficient of the atomizer having annular slit in the present study was found to be 0.86 which was higher than that of free fall atomizers having discrete nozzles available in the literature. Its value was also observed to be independent of plenum pressure of the atomizer.
5. The thickness uniformity of the disc shape deposit increases with the increase in its distance from the atomizer, with the offset distance from the atomizer axis and with the increase in its inclination angle.
6. Mathematical models presented in this study were found to describe the effect of substrate distance, its offset distance and inclination angle on thickness uniformity of the deposit.
7. The porosity of the Al-Si-Pb spray deposited alloy increases with the increase in lead content and decreases with the distance from centre to periphery of the deposit. It remains constant with thickness of the deposit.
8. The effect of lead content on porosity decreases with the distance from centre to periphery of the deposit.
9. The areas having large and small amount of porosity were observed in the microstructure of Al-Si-Pb alloys. The large and small amount porosity areas belong to the lead and aluminum rich areas, respectively.
10. Particles/droplets of two different types were found to deposit on the substrate. First type particles were aluminum rich and the second type were lead rich. Lead rich particles increases with the increase in lead content. Aluminum rich

particles were coarser than lead rich particles. Lead particles were observed in inter-dendritic regions of the particle microstructure.

11. The lead was uniformly dispersed in the spray deposit. The size of lead particles increases linearly with the increase in lead content.
12. The size of lead particles was higher at the centre as compared to that of periphery of the deposit.
13. The size of the aluminum grains was almost same at the bottom and top regions whereas it was lower at the peripheral region of the preform. In middle region the grain size was a little bit coarser than that of the top or bottom region.
14. In SEM the grain boundaries were not very clear with the increase in lead content and the maximum amount of lead was distributed along the grain boundaries.
15. Some silicon particles were observed to be surrounded by lead at the grain boundary of aluminum phase.
16. Hardness of the deposit decreases with the increase in lead content and its effect increases with the increase in lead content. Hardness value is high for high silicon content
17. Hardness of the preform increases from centre to periphery of the deposit whereas it remains constant with the increase in distance from bottom to top of the deposit.
18. Hardness is not affected by the grain size although it decreases with the increase in porosity of the deposit.
19. Ultimate tensile strength, proof stress and elongation to fracture decreases linearly with the increase in lead content of the deposit. Both the strengths and elongation increase linearly with the increase in distance from centre to periphery of the deposit. Both the strengths are also higher for higher silicon content.
20. Ultimate tensile strength, proof stress and elongation to fracture decreases exponentially with the increase in porosity of the deposit.
21. Both, Ultimate tensile strength and proof stress have a linear relationship with the hardness of the deposit.



22. Increase in wear rate with the increase in applied load has three stages, in the second stage rate of increase in wear rate is the lowest and in the third stage it is the highest.
23. Wear rate decreases linearly with the increase in lead content and it is lower for 12 % Si as compared to that of 6 % Si in Ai-Si-Pb alloy.
24. The wear rate decreases with the increase in distance from centre to periphery of the deposit.
25. Coefficient of friction decreases rapidly up to the load of 40 N and beyond this load the friction coefficient is almost constant. The coefficient of friction is lower for higher lead content.



**CHAPTER-8**  
**SCOPE FOR FUTURE WORK**

*CHAPTER-8***SCOPE FOR FUTURE WORK**

1. Atomizer or nozzle design should be such that it could produce preform of uniform thickness.
2. Lead can be replaced by the graphite.
3. Cooling rate of droplet or solidification rate of the preform can be increased to get more fine grains.
4. Porosity formation should be decreased.
5. Mechanical processing of the preform and its characterization can be carried out.



# REFERENCES

## REFERENCES

1. Abramov V.O., Abramov O.V., Sommer F. and Orlov D., "Influence of Si addition on the microstructure and the properties of Al-Pb base alloys prepared under quasi-weightlessness condition", *Mater Lett.*, 29, 67-71 (1996).
2. An J., Dong C. and Zhang Q.Y., "Improvement of the wear behavior of stircast Al-Si-Pb alloys by hot extrusion", *Tribol. Int.*, 36, 25-34 (2003).
3. An J., Liu Y.B. and Lu Y., "The influence of Pb on the friction and wear behavior of Al-Si-Pb alloys", *Mater. Sci. Eng. A* 373, 294-302 (2004).
4. An J., Liu Y.B., Lu Y., Zhang Q.Y. and Dong C., "Dry sliding wear behavior of hot extruded Al-Si-Pb alloys in the temperature range 25-200 °C", *Wear*, 256, 374-385 (2004).
5. Ogita Y., Ido Y. and Sakamoto M., "Improvement of aluminum-lead bearings", *MPR*, 37-44 (1991).
6. Pathak J. P., Tiwari S. N. and Malhotra S. L., "On the wear characteristics of leaded aluminium bearing alloys", *Wear*, 112, 341-353 (1986).
7. Pathak J.P., Torabian H. and Tiwari S.N., "Antiseizure and antifriction characteristics of Al-Si-Pb alloys", *Wear*, 202, 134-141 (1997).
8. Sharma A. and Rajan T.V., "Bearing characteristics of cast leaded aluminum-silicon alloys", *Wear*, 197, 105-114 (1996).
9. Sharma A. and Rajan T.V., "Scanning electron microscopic studies of worn-out leaded aluminum-silicon alloy surfaces", *Wear*, 174, 217-228 (1994).
10. Zhu M., Gao Y., Chung C.Y., Che Z.X., Luo K.C. and Li B.L., "Improvement of wear behavior of Al-Pb alloys by mechanical alloying", *Wear*, 242, 47-53 (2000).
11. Fang X., Fan Z., "Rheo-die casting of Al-Si-Pb immiscible alloys", *Scripta Mater.*, 54, 789-793 (2006).
12. Mohan S., Agarwala V. and Ray S., "Friction characteristics of stir-cast Al-Pb alloys", *Wear*, 157, 9-17 (1992).
13. Rudrakshi G.B., Srivastava V.C., Pathak J.P. and Ojha S.N., "Spray forming of Al-Si-Pb alloys and their wear characteristics", *Mater. Sci. Eng. A* 383, 30-38 (2004).

14. Zhao J.Z., Drees S. and Ratke L., "Strip casting of Al-Pb alloys – a numerical analysis", *Mater. Sci. Eng.*, A282, 262-269 (2000).
15. Mohan S., Pathak J. P., Sarkar S., and Chander Nitin , "Surface Studies of Centrifugally Cast Aluminium based Lead Bearing Alloys", *J. Reinf Plast Comp*, 2007.
16. Mohan S., Agarwala V. and Ray S., "The effect of lead content on the wear characteristics of a stir-cast Al-Pb alloy", *Wear*, 140, 83-92 (1990).
17. Mohan S., Agarwala V. and Ray S., "Liquid-liquid dispersion for fabrication of Al-Pb metal-metal composites", *Mater. Sci. Eng. A*, 144, 215-219 (1991).
18. Guang R., Jing-En Z., Shengqi Xi and Pengliang Li, "Microstructure and morphology of Al-Pb bearing alloy synthesized by mechanical alloying and hot extrusion", *J. Alloy Compd.*, 419, 66-70 (2006).
19. An J., Liu Y.B., Zhang M.Z. and Yang B., "Effect of Si on the interfacial bonding strength of Al-Pb alloy strips and hot-dip aluminized steel sheet by hot rolling", *J. Mater. Process. Technol.*, 120, 30-36 (2002).
20. An J., Liu Y.B., Lu Y. and Zhang Q.Y., "The formation of reacted film and its influence on tribological properties of extruded Al-Si-Cu-20-25Pb alloy under dry sliding", *J. Mater. Sci.*, 38, 1975-1982 (2003).
21. Yu F., Dwarakadasa D.S. and Ranganathan S., "Microstructure and mechanical properties of spray-formed Al-Si-Pb alloys", *J. Mater. Process. Technol.*, 137, 164-167 (2003).
22. Padhi P., Anand Santosh K., Kar Debashis, Ghosh S. and Panigrahi S. C., "Modeling structure of Al-Sn alloys", *Mater. Sci. Forum*, 519-521, 1519-1524 (2006).
23. Torabian H., Pathak J.P. and Tiwari S.N., "On wear characteristics of leaded aluminium-silicon alloys", *Wear*, 177, 47-54 (1994).
24. Suh Y. C. and Lee Z. H., "Nucleation of liquid Pb-phase in hypermonotectic Al-Pb melt and the segregation of Pb-droplets in melt-spun ribbon", *Scripta Metall. Mater.*, 33, 1231-1237 (1995).
25. Cui C., Fritsching U., Schulz A. and Li Q., "Mathematical modeling of spray forming process of tubular performs Part 1. Shape evolution", *Acta Mater.*, 53, 2765-2774 (2005).

26. Cui C., Fritsching U. and Schulz A., "Three-Dimensional Mathematical Modeling and Numerical Simulation of Billet Shape in Spray Forming Using a Scanning Gas Atomizer", *Metall. Mater. Trans. B*, 38, 333-346 (2007).
27. Ojha K. V., Tomar A., Singh D. and Kaushal G. C., "Shape, microstructure and wear of hypoeutectic Al-Si alloys" *Mat. Sci. Engg. A*, 487, 591- 596 (2008).
28. Ward R.M., Barratt M.D., Jacobs M.H., Zhang Z., Dowson A.L., "A simple transient numerical model for heat transfer and shape evolution during the production of rings by centrifugal spray deposition" , *J. Mater. Sci.*, 39, 7259-7267 (2004).
29. Mi J. and Grant P.S., "Modelling the shape and thermal dynamics of Ni superalloy rings during spray forming Part 1: Shape modeling–droplet deposition, splashing and redeposition", *Acta Mater.*, 56, 1588-1596 (2008).
30. Liu D., Zhaao J. and Ye H., "Modelling of the solidification of gas – atomized alloy droplets during spray forming", *Mater. Sci. Eng. A*, 372, 229-234 (2004).
31. Liu D.M., Zhao J.Z. and Li M.S., "Modelling and experimental verification of tubular product formation during spray forming", *Trans. Nonferrous Met. Soc. China*, 19, 661-667 (2009).
32. Cui C., Fritsching U., Schulz A., Tinscher R., Bauckhage K. and Mayr P., "Spray forming of homogeneous 100Cr6 bearing steel billets", *J. Mater. Process. Tech.*, 168, 496-504 (2005).
33. Rudrakshi G.B., Srivastava V.C. and Ojha S.N., "Microstructural development in spray formed Al-3.5Cu-10Si-20Pb alloy and its comparative wear behaviour in different environmental conditions", *Mater. Sci. Eng. A*, 457, 100-108 (2007).
34. Liang X. and Lavernia E.J., "Solidification and microstructure evolution during spray atomization and deposition of Ni<sub>3</sub>Al", *Mater. Sci. Eng. A*, 161, 221-235 (1993).
35. Gupta M., Mohamed F.A. and Lavernia E.J., "Heat transfer mechanism and their effects on microstructure during spray atomization and codeposition of metal matrix composites", *Mater. Sci. Eng. A*, 144, 99-110 (1991).
36. Anand S., Srivatsan S., Wu Yue and Lavernia E.J., "Processing, microstructure and fracture behavior of a spray atomized and deposited aluminum-silicon alloy", *J. Mater. Sci.*, 32, 2835-2848 (1997).

37. Gibbons G.J. and Hansell R.G. "Down-Selection and Optimisation of Thermal-Sprayed Coatings for Aluminium Protection and Upgrade", *J. Therm. Spray Tech.*, 15, 340, 1059-9630 (2006).
38. Gibbons G.J. and Hansell R.G. "Thermal-Sprayed Coating on Aluminium for Mould Tool Protection and Upgrade" *J. Mater. Process. Tech.*, 924, 136 (2005).
39. Shukla P., Mishra N.S. and Ojha S.N., "Modelling of Heat Flow & Solidification during Atomization & Spray Deposition Processing", *ASM J Therm. Spray Tech.*, 12(1), 95-100 (2003).
40. Liang X., Earthman J.C. and Lavernia E.J., "On the mechanism of grain formation during spray atomization and deposition", *Acta metall. mater.*, 40, 3003-3016 (1992).
41. Srivastava A.K., Anandani R.C., Dhar A. and Gupta A.K., "Effect of thermal conditions on microstructural features during spray forming", *Mater. Sci. Eng. A*, 304-306, 587-591 (2001).
42. Pedersen T.B., Hattel J.H. and Pryds N.H, in: Proceedings of the 22nd RISØ International Symposium on Materials Science "A Geometrical model for the prediction of the billet shape in spray forming", 353-358 (2001).
43. Markus S., Cui C. and Fritsching U., "Analysis of deposit growth in spray forming with multiple atomizers", *Mater. Sci. Eng. A*, 383, 166-174 (2004).
44. Hattel J.H. and Pryds N.H, "A unified spray forming model for the prediction of billet shape geometry", *Acta mater*, 52, 5275-5288 (2004).
45. Pryds N.H and Hattel J.H., "Spray forming: A numerical investigation of the influence of the gas to melt ratio on the billet surface temperature", *Int. J. Therm. Sci.*, 44, 587-597 (2005).
46. Cai W. and Lavernia E.J., "Modeling of porosity during spray forming", *Mater. Sci. Eng. A*, 226-228, 8-12 (1997).
47. Cai W. and Lavernia E.J., "Modeling of porosity during spray forming: part II. Effects of atomization gas chemistry and alloy compositions", *Metall. Mater. Trans. B*, 29, 1097 (1998).
48. Sahu K.K., Dube R.K. and Koria S.C., "Aspects of porosity formation in spray deposited thin aluminium strip", *Powder Metall.*, 52, 135 (2009).
49. Schneider A., Uhlenwinkel V., Harig H. and Bauckhage K., "Overspray injection in spray forming of CuSn13.5 billets", *Mater. Sci. Eng. A*, 383, 114-121 (2004).



50. Bewlay B. P. and Cantor B., "Gas velocity measurement from a close-coupled spray deposition atomizer", *Mater. Sci. Eng. A*, 118, 207-222 (1989).
51. Cui C., Cao F. and Li Q., "Formation mechanism of the pressure zone at the tip of the melt delivery tube during the spray forming process", *J. Mater. Process. Tech.*, 137, 5-9 (2003).
52. Singh D., Koria S. C. and Dubey R. K., "Velocities of gas from free fall type atomizers" *Powder Metall.*, 42-1, 79-85 (1999).
53. Singh D., Koria S. C. and Dubey R. K., "Study of free fall gas atomization of liquid metals to produce powder", *Powder Metall.*, 44-2, 177-184 (2001),
54. Singh D., Koria S. C. and Dubey R. K., "Development of operating pressure diagram for free fall gas atomization of liquid metals" , *ISIJ International*, 43(12), 2067 (2003).
55. Singh D. and Dangwal S., "Effects of process parameters on surface morphology of metal powders produced by free fall gas atomization", *J. Mater. Sci.*, 41, 3853 (2006).
56. Anderson I.E., Figliola R.S. and Morton H., "Flow mechanism in high pressure gas atomization", *Mater. Sci. Eng.A*, 148, 101-114 (1991).
57. Biancaniello F.S., Espina P.I., Mattingly G.E. and Ridder S.D., "A flow visualization study of supersonic inert gas-metal atomization", *Mater. Sci. Eng. A*, 119, 161-168 (1989).
58. Fukuda T., "Gas velocity distribution for a confined type gas atomization nozzle", *Tetsu-to-hagane*, 82-8, 635-640 (1996).
59. Fukuda T., Nakanishi M., Kubo T., "Pressure distribution around the melt delivery tube for a confined type gas atomization nozzle", *Tetsu-to-hagane*, 82-8, 665-670 (1996).
60. Mates S.P. and Settles G.S., "A study of liquid metal atomization using close-coupled nozzles, part 1: gas dynamic behavior", *Atomization Spray*, 15, 1-22, (2005).
61. Tsao C.Y.A. and Su Y.H., "Modelling of solidification of molten metal droplets during atomization", *Metall. Mater. Trans. B*, 28, 1249-1256 (1997).
62. Grant P.S., Cantor B. and Katgerman L., "Modelling of droplet dynamic and thermal histories during spray forming-II. Effect of process parameters", *Acta metall. mater.*, 41, 3109-3115 (1993).

63. See B., Runkle J.C. and King T.B., "The disintegration of liquid lead streams by nitrogen jets", *Metall. Trans.*, 4, 2669-2672 (1973).
64. Grant P.S. and Cantor B., "Modelling of droplet dynamic and thermal histories during spray forming-III. Analysis of spray solid fraction", *Acta metall. mater.*, 43, 913-921 (1995).
65. Nichiporenko O.S. and Naida Yu.I., "Heat exchange between metal particles and gas in the atomization process", *Sov. Powder Metall. Met. Cream.*, 7 (67), 509-512 (1968).
66. Lubanska H., "Correlation of spray ring data for gas atomization of liquid metals", *J. Metals*, 2, 45-49 (1970).
67. Dube R.K., Koria S.C. and Subramanian, "Atomization of aluminum by multiple discrete nitrogen jets", *Powder Met. Int.*, 20(6), 14-17 (1988).
68. Li S., Wu P., Zhou W. and Ando T., "Kinetics of heterogeneous nucleation of gas-atomized Sn-5 mass %Pb droplets", *Mater. Sci. and Eng. A*, 473, 206-212 (2008).
69. Pillai S.K. and Ando T., "Modeling of the In-flight Solidification of Droplets Produced by the Uniform-Droplet Spray Process," *J. Therm. Sci.*, 48, 1495-1500 (2009).
70. Tinoco Jose, Widell Bjorn, Fredriksson Hasse, Fuchs Laszlo, "Modeling the in-flight events during metal spray forming", *Mater. Sci. Eng. A*, 365, 302-310 (2004).
71. Liu D., Zhao J. and Ye H., "Modeling of the solidification of gas-atomized alloy droplets during spray forming", *Mater. Sci. Eng. A*, 372, 229-234 (2000).
72. Xu Q., Gupta V.V. and Lavernia E.J., "Thermal behavior during droplet - based deposition", *Acta mater.* 48, 835-849 (2000).
73. Hogg, Lambourne A., Ogilvy A. and Grant P.S. "Microstructural characterisation of spray formed Si-30Al for thermal management applications", *Scripta Mater.*, 55, 111-114 (2006).
74. Sharma M.M., "Microstructure and mechanical characterization of various modified 7XXX series spray formed alloys", *Mater. Charact.*, 59, 91-99 (2008).
75. Ferrarini C.F., Bolfarini C., Kiminami C.S., Botta F W.J., "Microstructure and Mechanical properties of spray deposited hypoeutectic Al-Si alloy", *Mater. Sci. Eng. A*, 375-377, 577-580 (2004).

76. Gouthama, Rudrakshi G.B. and Ojha S.N., "Spray forming and wear characteristics of liquid immiscible alloys", *J. Mater. Process. Tech.*, 189, 224-230 (2007).
77. Srivastava V.C., Mandal R.K. and Ojha S.N., "Microstructure and mechanical properties of Al-Si alloys produced by spray forming process", *Mater. Sci. Eng. A*, 304-306, 555-558 (2001).
78. Srivastava V.C., Mandal R.K., Ojha S.N. and Venkateswarlu K., "Microstructural modifications induced during spray deposition of Al-Si-Fe alloys and their mechanical properties", *Mater. Sci. Eng. A*, 471, 38-49 (2007).
79. Tjong S.C. and Tam K.F., "Mechanical and thermal expansion behavior of hiped aluminum-TiB<sub>2</sub> composites", *Mater. Chem. Phys.*, 97, 91-97 (2006).
80. Askel M.H. and Eralp O.C., "Gas dynamics", Prentice Hall., London, 79-124, 197-198 (1994).
81. Beveridge G.S.G. and Schechter R.S., "Optimization: Theory and Practice", McGraw Hill, NY, 67-86 (1970).
82. Moir S.A., Jones H. and Beck S.B.M., "Gas velocities from free fall gas atomizers", *Powder Metall.*, 39, 271-276 (1996).
83. Lavernia E.J. and Wu Y., "Spray atomization and deposition", John Wiley and Sons, Chichester, 57 (1996).
84. Kumar A., Ghosh S. and Dhindaw B. K., "Simulation of Cooling Rate of Alloy Drops during Spray Casting", *Trans. Indian Institute of Metals*, 60, 2-3 (2007).
85. Singh D., Tomar A. and Ojha K. V., "Momentum and heat transfer in gas atomization of melts", *Steel Res. Int.* 78-3, 241-247 (2007).
86. Li S., Wu P., Fukuda H. and Ando T., "Simulation of the solidification of gas-atomized Sn-5 mass %Pb droplets", *Mater. Sci. and Eng. A*, 499, 396-403 (2009).
87. Chu M.G., Shiohara Y. and Flemings M.C., "Solidification of highly undercooled Sn-Pb alloy droplets", *Metall. Trans. A*, 15, 1303 (1984).
88. Jones H., "Ultra Rapid Quenching of Liquid Alloys", H. Herman (Ed.), Academic Press, NY, 19 (1981).
89. See Bruce and Johnston G.H., "Interaction between nitrogen jets and liquid lead and tin streams", *Powder Tech.*, 21, 119-133 (1978).
90. Osorio W.R., Garcia L.R., Goulart P.R. and Garcia, "Effect of eutectic modification and T4 heat treatment on mechanical properties and corrosion

- resistance of an Al-9 Wt% Si casting alloy”, *Mater. Chem. Phys.*, 106, 343-349 (2007).
91. Heiberg G. and Armberg L., “Investigation of the microstructure of the Al-Si eutectic in binary aluminum-7 wt% silicon alloys by electron backscatter diffraction”, *J. Light Metals*, 1, 43-49 (2001).
  92. Muller H.R., Ohla k., Zauter R. and Ebner M., “Effect of reactive elements on porosity in spray formed copper alloy billets”, *Mater. Sci. Eng. A*, 383, 78-86, (2004).
  93. Candan E., “Effect of alloying addition on the porosity of SiC<sub>p</sub> Preforms infiltrated by aluminium”, *Mater. Lett.*, 60, 1204-1208 (2006).
  94. Evans M., “Optimization of manufacturing processes”, Maney Publishing, London, 29 (2003).
  95. Hagege S., “Lead inclusion in silicon: Structure, morphology and thermal behavior”, *Interface Sci.*, 7, 85-101 (1999).
  96. Rao A.K.P., Das K., Murty B.S. and Chakraborty M., “Effect of grain refinement on wear properties of Al and Al-7Si alloy”, *Wear*, 257, 148-153 (2004).
  97. Bocchini G.F., “The influence of porosity on the characteristics of sintered material”, *Int. J. Powder Metall.*, 22, 185-202 (1986).
  98. Payne R.D., Moran A.L. and Cammarata R. C., “Relating porosity and mechanical properties in spray formed tubulars”, *Scripta metal.et. Mater.*, 29, 907-912 (1993).
  99. Gui M., Kang S.B. and Lee J.M., “Influence of porosity on dry sliding wear behavior in spray deposited Al-6Cu-Mn/ SiC<sub>p</sub> composite”, *Mater. Sci. Eng. A*, 293, 146-156 (2000).
  100. Lin Z., Hui Q.X., Hua D.B., Bo H.X. and Li Q.M., “Effect of porosity on wear resistance of SiC<sub>p</sub> /Cu composites prepared by pressureless infiltration”, *Tran. Nonferrous Met. Soc. China*, 18, 1076-1082 (2008).
  101. Hamid A.A., Ghosh P.K., Jain S.C. and Ray S., “The influence of porosity and particles content on dry sliding wear of cast in situ Al(Ti)-Al<sub>2</sub>O<sub>3</sub>(TiO<sub>2</sub>) composite”, *Wear*, 265, 14-26 (2008).



**APPENDIX**



## Appendix-A

### Derivation for $r_1$ and $r_2$ of figure 6.4

In  $\Delta$  edg

$$\frac{h_1}{r - gc} = \tan \theta$$

or

$$\frac{h_1}{r - h_1 \tan \alpha / 2} = \tan \theta$$

or

$$\begin{aligned} h_1 &= \frac{r \tan \theta}{1 + \tan \theta \tan \alpha / 2} \\ &= \frac{r \sin \theta}{\cos \theta + \sin \theta \tan \alpha / 2} \end{aligned}$$

or

$$r_1 = \frac{r}{\cos \theta + \sin \theta \tan \alpha / 2}$$

Now,

$$\tan \alpha / 2 = \frac{f K}{h_2} = \frac{M K}{\tan \theta \cdot h_2}$$

$$= \frac{h_2 - BM}{h_2 \cdot \tan \theta} = \frac{h_2 - r \tan \theta}{h_2 \tan \theta}$$

$$h_2 - h_2 \tan \theta \cdot \tan \alpha / 2 = r \tan \theta$$

$$h_2 = \frac{r \tan \theta}{1 - \tan \theta \cdot \tan \alpha / 2}$$

$$h_2 = \frac{r \sin \theta}{\cos \theta - \sin \theta \cdot \tan \alpha / 2}$$

$$r_2 = \frac{r}{\cos \theta - \sin \theta \cdot \tan \alpha / 2}$$

## Appendix-B

### Some publications from this work

1. Momentum and Heat Transfer during gas atomization of melts.  
D. Singh, Aruna Tomar, K.V. Ojha  
**Steel Research Int.**, 78(3), 241-247 (2007).
2. Shape, microstructure & wear of spray formed hypoeutectic Al-Si alloys.  
K.V. Ojha, A. Tomar, D. Singh  
**Materials Science and Engineering A** 487, 591 – 596 (2008).
3. Shape, Wear & Mechanical properties of spray formed hypoeutectic Al-Si alloys.  
K.V. Ojha, A. Tomar, D. Singh  
**Trans. IIM**, 61(2), 1-5 (2008).
4. Mathematical model for the solidification of gas atomized droplets.  
D. Singh, Aruna Tomar, K.V. Ojha  
**Trans. PMAI**, 33(12), 1-8 (2007).
5. Porosity and microstructure of spray formed Al-Si-Pb alloys.  
Aruna Tomar and Devendra Singh  
**Material science and engineering**, communicated.
6. Mathematical models to describe the thickness uniformity of disc shape preform produced by spray forming.  
A. Tomar and D. Singh  
**Scripta Matrilia**, communicated.
7. D. Singh, Aruna Tomar, K.V. Ojha, “Mathematical model for the solidification of gas atomized droplets”, International conference on emerging



solutions through powder metallurgy for automotive and engineering industry & 33rd ATM, 2007, PMAI, New Delhi, India, February 9-11, 2007.

8. K.V. Ojha, A. Tomar, D. Singh, "Shape, Wear & Mechanical properties of spray formed hypoeutectic Al-Si alloys", International conference on Metals and alloys: Past, Present and Future held at Kanpur, December 7-9, 2007.